Nano-size Effect on Phase Transition of Atmospheric Aerosol Particles

Dissertation zur Erlangung des Ges
‘Doktor rerum naturalium (Dr. rer.nat.)’
im Promotionsfach Chemie
am Fachbereich Chemie, Pharmazie, Geographie und Geowissenschaften
der Johannes Gutenberg-Universität in Mainz
Paul Crutzen Graduate School
Max Planck Graduate Center

Chuchu Chen
geb. in Zhoushan, China

Mainz, 2022

1. Berichterstatter:

2. Berichterstatter:

Tag der mündlichen Prüfung:

Declaration

I hereby declare that I wrote the dissertation submitted without any unauthorized external assistance and used only sources acknowledged in the work. All textual passages which are appropriated verbatim or paraphrased from published and unpublished texts as well as all information obtained from oral sources are duly indicated and listed in accordance with bibliographical rules. In carrying out this research, I complied with the rules of standard scientific practice as formulated in the statutes of Johannes Gutenberg University Mainz to insure standard scientific practice.

Chuchu Chen
Mainz, 2022

Abstract

Phase transition is a physical phenomenon prevalent in nature, accompanied by the transfer of mass and heat, and changes the physicochemical properties of substances. Particle size is considered as another vital dimension in regulating the phase transition of nanoparticles except for chemical composition, temperature, relative humidity, and pressure. Atmospheric new particle formation (NPF) as a large contribution of cloud condensation nuclei (CCN) shows a strong size dependence on the initial cluster growth. However, there are several major issues in the current study of size-dependent phase transitions in the NPF process. For instance, it is difficult to quantitatively observe and analyze the size effect on the phase transition of particles below 6 nm. Few models consider the significant size effect of surface tension for nanoparticles below 6 nm. The structure of the corresponding nanoparticle at the critical phase transition point is still under debate. The underlying mechanism at the molecular level to explain the size dependence of phase transition of inorganic and organic nanoparticles remains inconsistent.

The thesis aims to quantitatively explore the size-dependent phase transition of organic and inorganic aerosol nanoparticles below 6 nm as well as the nanoparticle structure corresponding to the critical point and its underlying mechanism, based on the molecular dynamics simulations and thermodynamic data analyses.

In the first part of this thesis, the size-dependent solubility of NaCl nanoparticles (volume equivalent diameter ranges from 0.507 to 1.745 nm) in water droplets is investigated by using molecular dynamics simulations with improved q_8 evaluation criteria, and analyzing the structure of the corresponding saturated aqueous nanodroplet. A significant size-dependent solubility of NaCl nanoparticles is observed in the simulations, which can be well predicted by combining the Ostwald-Freundlich equation and the Gibbs-Duhem equation with consideration of size-dependent solid-liquid surface tension. Further structure analysis of the corresponding saturated aqueous nanodroplet shows that the distribution of ions and water in saturated nanodroplet is inhomogeneous. The concentration of NaCl in the inner part is larger than the one near the surface. Moreover, the spatial structure of dissolved ions in the aqueous nanodroplet resembles the structure of molten NaCl nanoparticle at the melting point, and the similarity grows when the size decreases. The melting point temperature of NaCl nanoparticles is size-dependent, as is the solubility of NaCl nanoparticles. The

nanoparticle contains 7 pairs of NaCl ions at 300 K is proved to be molten. Smaller molten particles at 300 K (≤7 pairs of NaCl ions) are thought to be the dissolved NaCl with infinite solubility.

In the second part of this thesis, the size dependence of succinic acid solvation is investigated by performing molecular dynamics simulations on the scale of ~1 to 4 nm with the potential of the mean forces method. The analyses reveal that the surface preference of succinic acid is stronger for a droplet than the slab of the same size, and the surface propensity is enhanced due to the curvature effect as the droplet becomes smaller. Energetic analyses show that such surface preference is primarily an enthalpic effect in both systems, while the entropic effect further enhances the surface propensity in droplets. On the other hand, with decreasing droplet size, the solubility of succinic acid in the internal bulk volume may decrease, imposing an opposite effect on the size dependence of solubility as compared with the enhanced surface propensity. Meanwhile, structural analyses, however, show that the surface to internal bulk volume ratio increases drastically, especially when considering the surface in respect to succinic acid, e.g., for droplet with radius of 1 nm, the internal bulk volume would be already close to zero for the succinic acid molecule.

In the third part of this thesis, the surface tension of aqueous NaCl is investigated by molecular dynamics simulations and pressure tensor method from dilute to highly supersaturated solutions. The results show that the linear approximation of concentration dependence of $\sigma_{NaCl,sol}$ at molality scale can be extended to the supersaturated NaCl solution until a molality of ~10.7 mol kg^{-1} (i.e., solute mass fraction (x_{NaCl}) of ~0.39). Energetic analyses reveal different regimes of concentration dependence of the surface tension of aqueous NaCl at 298.15 K: a water-dominated regime (x_{NaCl} from 0 to ~0.39), a transition regime (x_{NaCl} from ~0.39 to ~0.47) and a molten NaCl-dominated regime (x_{NaCl} from ~0.47 to 1). This study provides thermodynamic data for supersaturated bulk NaCl solutions, which can be compared with those for supersaturated NaCl nanoparticles from the first part of the thesis, thus reflecting the size effect on the solubility of NaCl nanoparticles except for the concentration effect.

In conclusion, based on the molecular dynamics simulations and thermodynamic analyses, this thesis provides a perspective for quantitative analysis of size effect on phase transition of organic and inorganic aerosol nanoparticles and its

underlying mechanisms from molecular level. The results of this thesis may be useful for studies about nanoparticles in various fields, such as atmospheric science, material science and chemical engineering.

Zusammenfassung

Der Phasenübergang ist ein in der Natur weit verbreitetes physikalisches Phänomen, das mit dem Transfer von Masse und Wärme einhergeht und die physikalisch-chemischen Eigenschaften von Substanzen verändert. Neben der chemischen Zusammensetzung, der Temperatur, der relativen Luftfeuchtigkeit und dem Druck gilt die Partikelgröße als eine weitere wichtige Dimension zur Regulierung des Phasenübergangs von Nanopartikeln. Die Bildung neuer Partikel in der Atmosphäre (NPF) als ein großer Beitrag von Wolkenkondensationskernen (CCN) zeigt eine starke Größenabhängigkeit vom anfänglichen Clusterwachstum. Bei der derzeitigen Untersuchung der größenabhängigen Phasenübergänge im NPF-Prozess gibt es jedoch mehrere wichtige Probleme. So ist es zum Beispiel schwierig, den Größeneffekt auf den Phasenübergang von Partikeln unter 6 nm quantitativ zu beobachten und zu analysieren. Nur wenige Modelle berücksichtigen den signifikanten Größeneffekt der Oberflächenspannung bei Nanopartikeln unter 6 nm. Die Struktur des entsprechenden Nanopartikels am kritischen Phasenübergangspunkt wird immer noch diskutiert. Der zugrunde liegende Mechanismus auf molekularer Ebene zur Erklärung der Größenabhängigkeit des Phasenübergangs von anorganischen und organischen Nanopartikeln bleibt uneinheitlich.

Ziel dieser Arbeit ist es, den größenabhängigen Phasenübergang von organischen und anorganischen Aerosol-Nanopartikeln unter 6 nm sowie die dem kritischen Punkt entsprechende Nanopartikelstruktur und den zugrundeliegenden Mechanismus auf der Grundlage von Molekulardynamiksimulationen und thermodynamischen Datenanalysen quantitativ zu untersuchen.

Im ersten Teil dieser Arbeit wird die größenabhängige Löslichkeit von NaCl-Nanopartikeln (Volumenäquivalentdurchmesser von 0,507 bis 1,745 nm) in Wassertröpfchen untersucht, indem Molekulardynamiksimulationen mit verbesserten q8-Auswertungskriterien verwendet werden und die Struktur des entsprechenden gesättigten wässrigen Nanotropfens analysiert wird. In den Simulationen wird eine signifikante größenabhängige Löslichkeit von NaCl-Nanopartikeln beobachtet, die durch Kombination der Ostwald-Freundlich-Gleichung und der Gibbs-Duhem-Gleichung unter Berücksichtigung der größenabhängigen Fest-Flüssig-Oberflächenspannung gut vorhergesagt werden kann. Eine weitere Strukturanalyse des entsprechenden gesättigten wässrigen Nanotropfens zeigt, dass die Verteilung von

Ionen und Wasser im gesättigten Nanotropfen inhomogen ist. Die NaCl-Konzentration im inneren Teil ist größer als die in der Nähe der Oberfläche. Darüber hinaus ähnelt die räumliche Struktur der gelösten Ionen im wässrigen Nanotropfen der Struktur der geschmolzenen NaCl-Nanopartikel am Schmelzpunkt, und die Ähnlichkeit nimmt mit abnehmender Größe zu. Die Schmelzpunkttemperatur von NaCl-Nanopartikeln ist größenabhängig, ebenso wie die Löslichkeit von NaCl-Nanopartikeln. Ein Nanopartikel mit 7 Paaren von NaCl-Ionen bei 300 K ist nachweislich geschmolzen. Kleinere geschmolzene Teilchen bei 300 K ($\leqslant$7 Paare von NaCl-Ionen) werden als gelöstes NaCl mit unendlicher Löslichkeit angesehen.

Im zweiten Teil dieser Arbeit wird die Größenabhängigkeit der Solvatisierung von Bernsteinsäure untersucht, indem Molekulardynamiksimulationen auf der Skala von ~1 bis 4 nm mit dem Potenzial der Methode der mittleren Kräfte durchgeführt werden. Die Analysen zeigen, dass die Oberflächenpräferenz von Bernsteinsäure für ein Tröpfchen stärker ist als für eine Platte gleicher Größe, und die Oberflächenneigung wird durch den Krümmungseffekt verstärkt, wenn das Tröpfchen kleiner wird. Energetische Analysen zeigen, dass diese Oberflächenpräferenz in beiden Systemen in erster Linie ein enthalpischer Effekt ist, während der entropische Effekt die Oberflächenneigung in Tröpfchen weiter verstärkt. Andererseits kann mit abnehmender Tröpfchengröße die Löslichkeit der Bernsteinsäure im inneren Volumen abnehmen, was einen entgegengesetzten Effekt auf die Größenabhängigkeit der Löslichkeit im Vergleich zur verstärkten Oberflächenneigung hat. Strukturanalysen zeigen jedoch, dass das Verhältnis von Oberfläche zu internem Volumen drastisch ansteigt, insbesondere wenn die Oberfläche in Bezug auf die Bernsteinsäure betrachtet wird, z. B. für ein Tröpfchen mit einem Radius von 1 nm, wäre das interne Volumen für das Bernsteinsäuremolekül bereits nahe Null.

Im dritten Teil dieser Arbeit wird die Oberflächenspannung von wässrigem NaCl mit Hilfe von Molekulardynamiksimulationen und der Drucktensormethode von verdünnten bis zu stark übersättigten Lösungen untersucht. Die Ergebnisse zeigen, dass die lineare Approximation der Konzentrationsabhängigkeit von $\sigma_{NaCl,sol}$ auf der Molalitätsskala auf die übersättigte NaCl-Lösung bis zu einer Molalität von ~10.7 mol kg^{-1} (d.h. gelöster Massenanteil (x_{NaCl}) von ~0.39) ausgedehnt werden kann. Energetische Analysen zeigen verschiedene Regime der Konzentrationsabhängigkeit der Oberflächenspannung von wässrigem NaCl bei 298.15 K: ein von Wasser

dominiertes Regime (x_{NaCl} von 0 bis ~0.39), ein Übergangsregime (x_{NaCl} von ~0.39 bis ~0.47) und ein von geschmolzenem NaCl dominiertes Regime (x_{NaCl} von ~0.47 bis 1). Diese Studie liefert thermodynamische Daten für übersättigte NaCl-Lösungen, die mit denen für übersättigte NaCl-Nanopartikel aus dem ersten Teil der Arbeit verglichen werden können und somit den Größeneffekt auf die Löslichkeit von NaCl-Nanopartikeln mit Ausnahme des Konzentrationseffekts widerspiegeln.

Auf der Grundlage der Molekulardynamiksimulationen und thermodynamischen Analysen bietet diese Arbeit eine Perspektive für die quantitative Analyse des Größeneffekts auf den Phasenübergang von organischen und anorganischen Aerosol-Nanopartikeln und der zugrunde liegenden Mechanismen auf molekularer Ebene. Die Ergebnisse dieser Arbeit können für Studien über Nanopartikel in verschiedenen Bereichen, wie z. B. Atmosphärenwissenschaften, Materialwissenschaften und Chemieingenieurwesen, nützlich sein.

Contents

1. Introduction

1.1 Size effect on phase transitions

In a thermodynamic system, a phase is used to describe a spatial region where all the physical properties of a substance are basically uniform (Beegle et al., 1974; Atkins et al., 2014). The phase transition is the spontaneous transforming process from one phase into another phase at the transition temperature under a given pressure (Atkins et al., 2014). It is a physical phenomenon prevalent in nature, accompanied by the transfer of mass and heat, and changes the physicochemical properties of substances. For instance, aerosol particles undergo ubiquitous phase transitions, ranging from liquid, solid and semi-solid, and interact with gases under atmospheric conditions (Seinfeld et al., 1998; Hinds, 1999; Pöschl, 2005; Pöschl and Shiraiwa, 2015; Seinfeld and Pandis, 2016; Mikhailov et al., 2009). New particle formation (NPF) is the creation and growth of molecular embryos or clusters during the phase transformation from vapor to liquid or solid. Deliquescence of solid salts including sodium chloride (NaCl) arising from ocean spray over breaking waves at high relative humidity (RH) is the phase transition from solid to liquid. The formation of ice nuclei (IN) or cloud condensation nuclei (CCN) is the phase transition from liquid to solid at a certain relative humidity and temperature. A substantial amount of theoretical understanding on phase transitions aids in the development of novel materials and technologies for the benefit of human life and environmental protection. For example, some phase-change materials, which can absorb or release heat via reversible phase change, show great promise in the domains of heat storage and thermal management, resulting in energy savings and environmental protection. However, current theoretical knowledge of phase transitions is still incomplete, e.g., the mechanisms behind the size dependence of several phase transition events in aerosol nanoparticles remain unknown..

A caveat mentioned here, is referring to the standard treatments of phase transitions in textbooks on statistical thermodynamics: there the size of the system is normally not considered as a parameter, and the so-called "thermodynamic limit" is implied. For the simplest case of a single-component system, this means the particle number N is taken to infinity, and in a pure phase in thermal equilibrium the two so-called "intensive" variables temperature T and pressure p characterize all properties, only one (so-called) extensive variable (i.e., proportional to N), e.g., the volume, enters. The potential energy μ per particle, or the volume per particle (V/N = inverse of the particle density), are functions of T and p only, there is no extra dependence on N, since

in the considered limit both surface effects and statistical fluctuations can be ignored. A phase transition, e.g., vapor to liquid or liquid to solid, then occurs at a well-defined transition temperature $T_{trans}(p)$. At this temperature, both the potential energy per particle and the volume per particle exhibit a "jump singularity", i.e., are discontinuous functions of T when $T_{trans}(p)$ is crossed.

However, when considering finite systems, two effects come into play: (i) surface effects, which for more or less compact liquid droplets or crystalline clusters are of relative order $(\frac{1}{\sqrt[3]{N}})$ for the potential energy per particle, density, etc., causing a shift of the transition temperature $T_{trans}(p,N)$ relative to $T_{trans}(p)$, also of this order. (ii) Effects due to statistical fluctuations, which are of relative order $(\frac{1}{\sqrt[2]{N}})$. This effect causes a "rounding" of the transition, because there is also no longer an infinitely high free energy barrier between the two phases that can coexist right at the transition. So there is a temperature region around $T_{trans}(p,N)$ where the system by such fluctuations spontaneously "jumps back and forth" between both phases during macroscopic observations times (for which hysteresis can be ignored, and such large observation times are tacitly assumed when one speaks about thermal equilibrium).

When N is large (N of the order 10^3 typically is already large enough), $(\frac{1}{\sqrt[3]{N}})$ is much larger than $(\frac{1}{\sqrt[2]{N}})$, so the shift may be clearly larger than the rounding, and it makes sense to ignore the rounding in practice, although in principle it is present for all finite values of N, and discuss only the shift of the transition as a function of the size of the system, as will typically be done later in this work. But when N gets smaller and smaller, the notion of well-defined phases and transitions between them gets gradually lost. From these considerations, it is obvious that there cannot be a valid answer to the question in general, how large N has to be, to allow to distinguish different phases, and locate for small N still transition temperatures $T_{trans}(p,N)$. The quantities that have discontinuities at $T_{trans}(p)$ for infinite N are continuous at $T_{trans}(p,N)$, the transition for large but finite N still shows up as an inflection point, but the slope at this point decreases with decreasing N. In addition, the positions of the inflection points for different quantities like potential energy per particle, volume per particle, for small N will no longer coincide precisely.

In the rest of the thesis, the rounding of transitions in small particles will be mostly disregarded, but one should keep this caveat in mind.

1.2 Size effect on atmospheric new particle formation

Atmospheric aerosols are defined as fine solid or liquid particles or as a mixture of both suspended in the air, with particle diameters in the range of 10^{-9} to 10^{-4} m (Seinfeld et al., 1998; Hinds, 1999; Pöschl, 2005; Pöschl and Shiraiwa, 2015; Seinfeld and Pandis, 2016). They play an important role in atmospheric chemistry and physics, climate, biosphere, and human health (Ammann et al., 1998; Pöschl, 2005; Ervens, 2015). In recent years, due to the improvement in the technology of observation and simulation, new particle formation (NPF) events have been observed directly and proved to be a significant contribution to atmospheric aerosol population (Fig. 1-1) (Kulmala et al., 2004; Yu and Turco, 2008; Merikanto et al., 2009). New particle formation (NPF) is a crucial secondary phase transformation process, by which supersaturated gaseous precursors (e.g., sulfuric acid and low volatile organic compounds) produced by the oxidation of gaseous pollutants condense into clusters, which subsequently collapse through condensation to form particles (Zhang et al., 2012). NPF occurs in two distinct stages: (1) nucleation to form critical molecular embryos or clusters from gaseous vapors to liquid or solid, and (2) subsequent growth of these clusters to detectable sizes or even larger sizes (>2 to 3 nm) that competes with removal by preexisting aerosols (Zhang, 2010; Zhang et al., 2012; Kulmala et al., 2013). NPF is a worldwide phenomenon and occurrences vary with season and location including urban, forested, marine, and free troposphere (Kulmala et al., 2004; Wang et al., 2017; Kerminen et al., 2018; Zheng et al., 2021). Both observations and global simulations suggest that NPF is the dominant source of atmospheric aerosol particle number concentration in the troposphere and the continental boundary layer (Dunne et al., 2016; de España et al., 2017; Fountoukis et al., 2012; Gordon et al., 2017; Kuang et al., 2009; Laakso et al., 2013; Lihavainen et al., 2003; Merikanto et al., 2009; Pierce and Adams, 2009; Reddington et al., 2011; Rose et al., 2017; Yu and Luo, 2009; Yue et al., 2011). The newly formed particles can further contribute to the cloud condensation nuclei (CCN) budget, thereby altering cloud albedo, structure, and lifetimes, and insolation reaching the Earth's surface (Barahona et al., 2010; Boucher and Lohmann, 1995; Fan et al., 2016; Gordon et al., 2016; Li et al., 2017; Mauritsen et al., 2011; Rosenfeld et al., 2014; Seinfeld et al., 2016; Zhang et al., 2010).

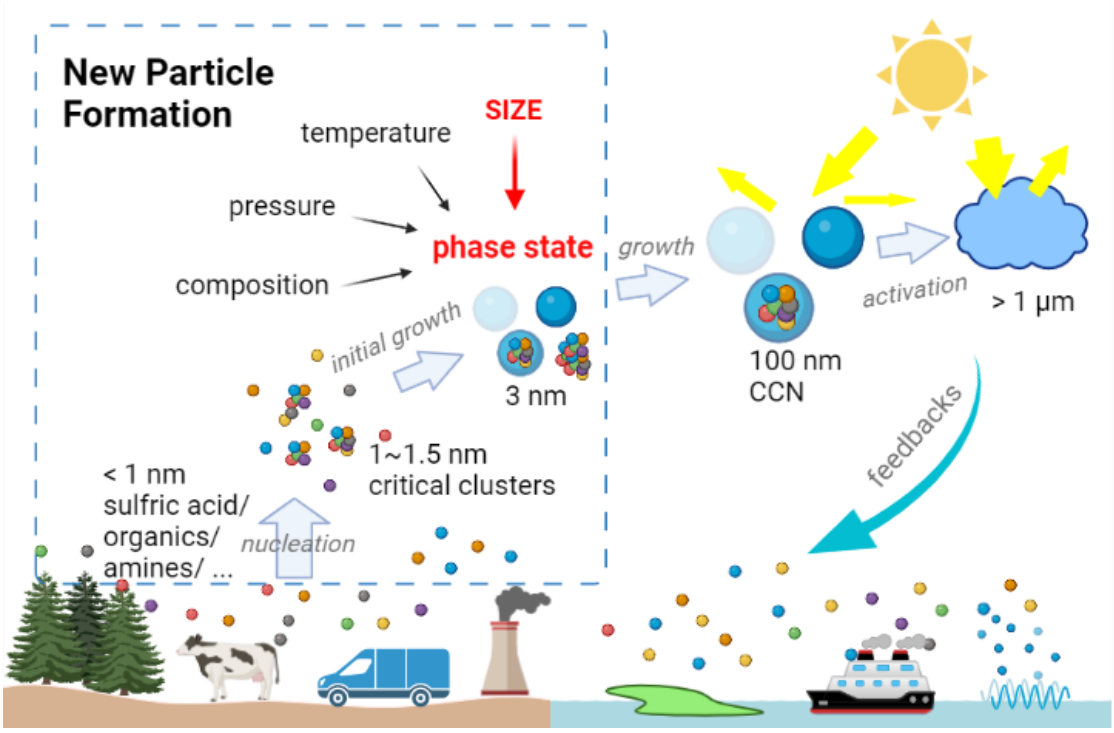

Figure 1-1: **Dynamics of new particle formation (NPF) from vapor to cloud droplet.** Particle size along with chemical composition, temperature, and pressure is the vital dimension in regulating the phase transition of nanoparticles including NPF. NPF is a large source for cloud condensation nuclei (CCN), which affect the cloud formation and atmospheric radiation and thereby affect climate and Earth environment.

Particle size along with chemical composition, temperature, and pressure is considered as another vital dimension in regulating the phase transition of nanoparticles (Cheng et al., 2015; Guo et al., 2015; Jeevanandam et al., 2018; Tolbert and Alivisatos, 1994). At the nanoscale, physicochemical properties of substances obviously change compared to their bulk condition due to the confinement and finite size effects.

NPF including multiphase transitions significantly depend on particle sizes (Fletcher, 1958; Lü et al., 2013; Zhang et al., 2012). Particle size has been proved to be quite related to the details of the nucleus surface and the changes of surface tension (Prestipino et al., 2014). It can influence the molecule concentrations and interactions at the surface of nanoparticles compared to the bulk, and hence influence the nucleation. For liquid-vapor equilibrium and phase partitioning, the increasing curvature of smaller nanoparticles can lead to a higher vapor pressure in a certain RH and hence to a higher solute concentration, which is termed the Kelvin effect (Eq. 1-1) (von Helmholtz, 1886;

Zhang et al., 2004; Shchekin and Rusanov, 2008; Donahue et al., 2013). This imposes a restriction in the growth of freshly nucleated nanoparticles.

$$P = P_0 \cdot \exp\left(\frac{4\sigma_{\mathrm{lv}} v_{\mathrm{l}}}{RTD}\right) \quad (1-1)$$

Where P is the saturated vapor pressure of the particle with a diameter of D; P_0 is the vapor pressure of a planar surface; σ_{lv} is the liquid-vapor surface tension; v_l is the molar volume of liquid; R is the gas constant and T the temperature in Kelvin.

For liquid-solid equilibrium, the increasing curvature of smaller nanoparticles can induce higher solubility of nanocrystals, which is termed the Ostwald–Freundlich effect (Eq. 1-2) (Freundlich, 1909; Kaptay, 2012; McCoy, 2001; Letellier et al., 2007; Shchekin and Rusanov, 2008).

$$a_{\mathrm{s}}^{*} = a_{\mathrm{s,bulk}}^{*} \cdot \exp\left(\frac{4\sigma_{\mathrm{sl}} v_{\mathrm{s}}}{RTD}\right) \quad (1-2)$$

Where a_{s}^{*} is the saturated solute activity of the particle with a diameter of D; $a_{\mathrm{s,bulk}}^{*}$ is the saturated solute activity in the bulk solution; σ_{sl} is the liquid-vapor surface tension; v_s is the molar volume of solid; R is the gas constant and T the temperature in Kelvin.

For vapor-solid equilibrium, the increasing curvature of smaller nanoparticles can lead to a lower freezing point depression, which is termed the Gibbs–Thomson effect (Eq. 1-3) (Johnson, 1965; Perez, 2005).

$$\Delta T = T_{\mathrm{bulk}} \frac{4\sigma_{\mathrm{sl}} v_{\mathrm{s}}}{\Delta H D} \quad (1-3)$$

Where ΔT is the depression of phase transition (melting) temperature of the particle with a diameter of D; T_{bulk} is the bulk melting temperature; v_s is the molar volume of solid; σ_{sl} is the liquid-vapor surface tension; v_s is the molar volume of solid; ΔH is the bulk enthalpy of phase transition.

In addition, surface tension is also size-dependent inferred by Tolman length based on Gibbs' theory of surface tension (Eq. 1-4) (Tolman, 1948, 1949b, a).

$$\sigma = \frac{\sigma_{\mathrm{bulk}}}{1 + (\frac{4\delta}{D})} \quad (1-4)$$

Where σ is the interfacial energy of the droplet with a diameter of D; σ_{bulk} is the bulk interfacial energy; δ is the Tolman length. For water and organic liquids, some studies have confirmed that surface tension decreases with the decrease in droplet size; the decrease becomes significant for smaller particles (Tolman, 1949a; Fisher and

Israelachvili, 1981; Factorovich et al., 2014; Menzl et al., 2016). The size dependence of surface tension hence contributes to the size effect on the nucleation.

Size effect on phase transitions of nanoparticles is important not only in the field of atmospheric NPF but also in other fields. For instance, in material science, the melting point temperature of some metal nanoparticles shows a significant size dependence, i.e., the temperature decreases with the decrease in size compared to the bulk. This infers that some metal nano materials could exist in liquid-like states at room temperature (Sun et al., 2014; Cao et al., 2019). A full understanding of this size effect on the phase transition process is essential for the development of next generation semiconductor nano materials. Meanwhile, in the pharmacology field, size can influence the properties of nanodrug, thereby controlling release rates and positions in the human body, and further improving efficiency of drugs and decreasing side effects (Qiu et al., 2015; Ji et al., 2018; Qin et al., 2018).

Therefore, it is essential to deeply investigate the size effect on the phase transition of nanoparticles, not only for various compounds but also for distinct phase transition processes with the same material. Such research would provide a new dimension to the various existing theories for the underlying mechanisms of phase transition in numerous areas, including the NPF process in the atmosphere which gives a sound scientific foundation for CCN formation.

1.3 Approaches to size effect on phase transitions of NPF and limitations

Several efforts have been undertaken to elucidate the size effect on the atmospheric NPF based on a variety of experimental measurements and theoretical calculations.

It is challenging to directly observe the size effect on particle phase states in the NPF processes. In recent years, instrumentation has been improved in order to more accurately observe the phase transitions of smaller nanoparticles. Table 1-1 shows specific techniques commonly used in laboratory over the past years for observing the phase transition of nanoparticles in different sizes. For example, a variety of techniques including XRD, TEM, optical microscopy, Raman spectroscopy and small angle x-ray scattering were used to probe size dependence in temperature-induced or pressure-induced solid-solid and solid-liquid phase transition (Goldstein et al., 1992; Tolbert and Alivisatos, 1994; Gribb and Banfield, 1997; McHale et al., 1997; Zhang et al., 2006;

Rivest et al., 2011). Cryogenic-Transmission Electron Microscopy (cryo-TEM) was used to characterize the morphology of nanoparticles that were generated and dried in the gas phase under ambient conditions. A size dependence of the morphology was observed, where small particles of succinic and pimelic acids mixed with ammonium sulphate (<40 nm) were homogeneous, and large particles (>40 nm) were phase separated (Veghte et al., 2014; Altaf and Freedman, 2017). In addition, a partially engulfed morphology was found in generated nanoparticles using SAXS and FTIR techniques (Pathak et al., 2014). In recent years, AOT was developed to improve the precision in size measurements (Rickards et al., 2013), and AFM was used to directly measure the three-dimension morphology and phase transition of nanoparticles with diameter down to 10 nm (Estillore et al., 2017). XPS was used to probe surface activity of succinic acid in sodium chloride and ammonium sulphate solutions, and a higher solubility of succinic acid was found at the interface compared to bulk solutions (Werner et al., 2014; Werner et al., 2016). HTDMA and nano-HTDMA were frequently used to measure the hygroscopicity growth factor of different sizes of particles at a given RH, and further observing the deliquescence and efflorescence processes of particles (Biskos et al., 2006a; Biskos et al., 2006b; Biskos et al., 2006c; Lei et al., 2020). Despite the significant improvements in instrument performance, the detected nanoparticles are mostly on scales greater than 6 nm, which is more than the particle size (≤3 nm) during nucleation and initial growth processes, thus the experimental results of size effect on the physicochemical properties of NPF particles are lacking.

Table 1-1: Techniques for investigating the phase transition of nanoparticles.

Techniques	Size range	Information provided
X-Ray Diffraction (XRD)	≥2 nm	Crystalline phases, grain size, film thickness, and crystallite orientations
Small Angle X-ray Scattering (SAXS)	≥10 nm	Topography, morphology, imaging
Scanning Electron Microscopy (SEM)	≥10 nm	Topography, morphology, imaging, crystallographic structure, and Elemental composition
Transmission Electron Microscopy (TEM)	≥10 nm	Topography, morphology, imaging, crystallographic structure, and Elemental composition
Optical microscopy	≥10 μm	Topography, morphology, imaging
Fourier Transform Infrared Spectroscopy (FTIR)	≥1 μm	Chemical functional groups, imaging, and mapping
Raman Spectroscopy	≥10 μm	Structural and chemical information, bonding state, and structural order
Optical Tweezing (AOT)	≥400 nm	Trapping of supermicron particles by gradient forces: phase, thermodynamics, water uptake, heterogeneous reactions
X-ray Photoelectron Spectroscopy (XPS)	≥10 nm	Surface properties
Atomic Force Microscopy (AFM)	≥10 nm	Surface properties
Hygroscopicity tandem differential mobility analyzer (HTDMA)	20 nm to 1 μm	Hygroscopicity/volatility
Nano-Hygroscopicity Tandem Differential Mobility Analyzer (nano-HTDMA)	6 nm to 20 nm	Hygroscopicity/volatility

Since the instrumentation is still unstable to directly observe size effects on nanoparticles below 6 nm diameter, theoretical calculations become an effective tool to help understand the size effects on the NPF process.

For thermodynamics and kinetics models, although the Kelvin effect has been commonly considered for liquid-vapor equilibrium and phase partitioning, size effects on the liquid-solid equilibrium upon phase transitions are rarely considered for nanoparticles in the new particle formation process. Kulmala et al (2004) extended the Köhler theory to describe the activation of nanometer-sized clusters to growth by condensation of vapor gases, which consider the Kelvin effect for liquid-vapor equilibrium and phase partitioning during the initial growth. The theory has been further applied in aerosol dynamics models to explain the observed behavior of sub 5 nm particle in field and laboratory measurements (Anttila et al., 2010; Korhonen et al., 2004; Kuang et al., 2012; Kulmala et al., 2013; Trostl et al., 2016). However, the Köhler theory requires to predict the accurate liquid-vapor surface tension and activity coefficients of the extremely small and highly concentrated clusters, which are significantly different from those of the bulk particles. Cheng et al. (2015) conducted the Differential Köhler Analysis (DKA) method to provide concentration-dependent water activity and liquid-vapor surface tension data for ammonium sulfate (AS) and sodium chloride (NaCl). Moreover, Cheng et al. (2015) included the size effects on the liquid-solid equilibrium phase diagrams of aerosol particles above 6 nm diameter. With DKA derived water activity and liquid-vapor surface tension, the interfacial energy at the solid-liquid interface for particles can be determined by combining the Gibbs-Duhem equation and Ostwald-Freundlich equation for the size-dependent solubility of nanoparticles above 6 nm diameter. Yet, the size-dependent solubility of nanoparticles with diameters smaller than 6 nm is unclear due to data constraints.

The solid-liquid interface energy of nanoparticles as a key factor affecting the size effect of nanoparticle solubility also has a significant size effect, especially for nanoparticles in the NPF process, however, this has not been fully considered in the present models. There is still a discussion regarding whether the solid-liquid interfacial energy of nanoparticles and that of solute embryos should be expected to close (Cohen et al., 1987; Gao et al., 2006; Gao et al., 2007). Cheng et al. (2015) reported that the solid-liquid interface energy of salt nanoparticles shows no significant difference larger than 6 nm, but decreases for embryos, which seems to be in line with the size

dependence of interfacial energy. Nevertheless, the magnitude and the underlying mechanisms of the size effect on the interfacial energy for particles below 6 nm remain inapplicable in the current thermodynamic models.

Size dependence has been observed in multiple phase transition processes for the same compound, indicating a similarity in the phase transition temperature and the size between the processes, although few investigations have provided the corresponding data. Phase transition processes such as dissolution, melting process, glass transition, nucleation and spinodal decomposition show the similar size dependence (Zhang et al., 2011; Kuhn et al., 2011; Burch and Bazant, 2009; Mudunkotuwa et al., 2012; Couchman and Jesser, 1977). For example, the freezing temperature and melting temperature of water is proved to be very similar size dependence (Pan et al., 2011; Manka et al., 2012; Li et al., 2013). The reason for this similarity is still unknown, however, despite the different hypotheses involved, the temperatures for distinct phase transition processes typically exhibit simple relations (Turnbull, 1950; Koop et al., 2011). The present theories for distinct phase transition processes should be validated and reconciled with a better understanding of size dependence of different phase transition processes for the same compound.

The size dependence of phase transitions is comparable in inorganic and organic particles but with distinct characteristics such as molecular density distributions, which has not been adequately explained. Thermodynamically, the Gibbs-Thomson equation derivation implies a close relationship between the solid-liquid interfacial energy and phase transition enthalpy, which may be applied to the size dependence of phase transition of a few substances (Johnson, 1965; Perez, 2005; Cheng et al., 2015). While the Turnbull equation exhibits a similar relationship, it differs from the derived equation by a cube root of the molar volume of solid (Turnbull, 1950). Thus, the thermodynamic models should be further validated.

Furthermore, the underlying driving mechanisms of size-dependent phase transitions of nanoparticles at molecular level are still not uniform. Several studies based on molecular level approaches, such as molecular dynamics (MD) simulations, have been done to explain the mechanisms by calculating the structures and free energy changes of nanoparticles. For example, the liquid-vapor surface tension of NaCl droplets derived from DKA exists a large deviation from the near-linear increase at a molality of 10 mol kg^{-1}, but the extent for the linear dependence of surface tension on

molality and the underlying reason for such a deviation remain unclear. Wang et al. (Wang et al., 2018) validated the linear approximation of concentration dependence of the liquid-vapor surface tension of NaCl planar from dilute to a molality of ~10.7 mol kg^{-1} (water-dominated regime) based on MD simulations, and further energetic analysis reveals that this monotonic increase in surface tension is driven by the increase in excess surface enthalpy as the solution becomes concentrated. Besides, several studies qualitatively explain the increased solubility of organics in nanoparticles at the molecular level as being due to the enrichment of solute molecules at the surface of the nanoparticles by MD simulations (Hub et al., 2012; Sayou et al., 2017). This appears to be in line with the Werner et al. (2016) report, where the size-dependent solubility of surface-active organic molecules in nanodroplets results from the enhanced surface concentration estimated from XPS experiments and the bulk-like particle concentration. However, inorganic compounds show a different molecular distribution in the nanodroplet compared to organic compounds that accumulate in the center of the nanodroplet, but still have the same size-dependent solubility. A unified interpretation of the size-dependent phase transition of inorganic and organic nanoparticles at the molecular level is still expected.

1.4 Research objectives and methods

As discussed above, particle size is proved to be another important dimension to describe the phase transition and equilibrium phase diagram of atmospheric new particle formation. However, it is still challenging to obtain the size effect on the nanoparticles below 6 nm especially for the NPF process either by experiments or by simulations. A reliable approach that can accurately quantify the size-dependent phase transition of particles below 6 nm is still lacking (Fig. 1-2 I). One of the major reasons for the lack approach is that the size effect of surface tension is not clear in the supersaturated nanoparticles (Fig. 1-2 II). Also, a uniform theory to explain the relationship between different size-dependent phase transitions for the same substance as well as the relationship between different compounds in the size-dependent phase transition is still in progress (Fig. 1-2 III, IV). Additionally, the molecular-level interpretation of the contribution of inorganic and organic compounds to the phase transition and the corresponding underlying mechanism remains a challenge (Fig. 1-2 V).

Therefore, the aim of this thesis is to investigate size dependence of phase transition of inorganic and organic nanoparticles and its underlying mechanism from molecular level by using molecular dynamics simulations. The trajectories of all molecules undergoing a phase transition for different sizes of nanoparticles are simulated. Based on these molecular dynamic data, the nano-size effect on phase transitions from the aspects of free energy change and structural changes of inorganic and organic nanoparticles is further analyzed. Specifically, in this thesis I addresses three key topics with the following objectives:

A. Investigate the size-dependent solubility of NaCl nanoparticles in water droplets based on the MD simulations and the corresponding thermodynamic analyses. The following questions are mainly addressed:

(1) What is the size-dependent solubility of NaCl nanocrystal below 2 nm?

(2) What is the corresponding size-dependent solid-liquid surface tension?

(3) What is the distribution of ions and water molecules in super saturated nanoparticles?

(4) What is the size dependence of different phase transition processes (i.e., dissolution and melting processes) for the same NaCl nanocrystal?

To answer these questions, firstly, an improved q_8 detection approach is developed to directly quantify the solubility of NaCl aqueous nanodroplets with different sizes in the MD simulations. Thus, the size-dependent solubility of NaCl nanoparticles by considering the size-dependent solid-liquid surface tension with the Gibbs-Duhem and Ostwald-Freundlich equations can be predicted. Next, the density profiles and distributions of ions and water molecules in the corresponding saturated NaCl nanodroplets are calculated to observe the structural features from molecular level. Furthermore, the chemical potentials of dissolved and melt NaCl nanoparticles are compared to quantitatively understand the similarity of the relationship between particle size and phase transition temperatures and the connection of dissolution and melting processes.

B. Investigate the size dependence of organic composition solvation in the nanoparticles based on the MD simulations and energetic analyses. The following questions are mainly addressed:

(1) What are the potential driving forces for the size dependence of succinic acid solvation in the nanoparticles?

(2) What is the size dependence of succinic acid solubility?

(3) What is the distribution of succinic acid molecule in the different sizes of water nanodroplets?

To answer these questions, firstly, the simulations for one single succinic acid molecule in different sizes of water nanodroplets and different thickness of water planar slabs are performed. The single succinic acid molecule is pulled from the center of mass of water nanodroplets to the interface to obtain the potential of mean forces (PMFs) profiles based on the Umbrella Sampling method. With the information of free energy change of succinic acid in the different sizes of water nanodroplets, the potential enthalpic and entropic driving force contribution can be identified to the size dependence of succinic acid solvation as well as the molecule distributions in water nanodroplets and planar slabs.

C. Explore the concentration-dependent thermodynamic properties (e.g., interfacial energy) of supersaturated bulk NaCl solution based on the MD simulations and energetic analyses. This study can be further used to compare with the thermodynamic properties of supersaturated NaCl nanoparticles from the first part of the thesis, thus reflecting the size effect on the solubility of NaCl nanoparticles in addition to concentration effects. The following questions are mainly addressed:

(1) What is the concentration-dependent interfacial energy of supersaturated aqueous NaCl solution?

(2) What are the potential driving forces for the concentration-dependent interfacial energy of supersaturated aqueous NaCl solution?

To answer these questions, firstly, molecular dynamics simulations and pressure tensor method are applied to calculate the concentration dependence of interfacial energy of NaCl from infinitely dilute to highly supersaturated solution to molten salt. Then, the surface enthalpy and entropy profiles and the density profiles distribution of ions are investigated to explore the underlying mechanisms behind the concentration dependence.

1.5 Overview

The key results of this PhD thesis are summarized in two first-author manuscripts for publication in peer-reviewed scientific journals and one co-author publication in the peer-reviewed scientific journal.

The Chapter 2 of this thesis is based on the manuscript "Size-dependent solubility of NaCl nanocrystal in aqueous droplet", which will soon be submitted. I performed the study under the guidance with my supervisors. I worked out the technical details including preparing sodium chloride and water force field and structure files, setting up and running molecular dynamics simulations under different scenarios, post-processing and analyzing the thermodynamic data such as ion and molecular structure information, energy profiles, density distributions, etc. I discussed the results, interpretation and implications and commented on the manuscript with the coauthors. I made the figures and tables, and wrote the manuscript.

The Chapter 3 of this thesis is based on the manuscript "Energetic analysis of succinic acid in water droplets: insight into the size-dependent solubility of atmospheric nanoparticles", which is available as preprint undergoing public peer review in an internationally leading journal of atmospheric science. I performed the study under the guidance with my supervisors. I worked out the technical details including choosing the reasonable succinic acid and water force field, preparing the molecule structure files, setting up and running molecular dynamics simulations, post-processing and analyzing the thermodynamic data such as the succinic acid molecule free energy profiles in different sizes of water nanodroplets, enthalpy and entropy decomposition profiles of the succinic acid molecule in different sizes of water nanodroplets, molecule density distributions, surface thicknesses of different sizes of nanodroplets, etc. I discussed the results, interpretation and implications and commented on the manuscript with the coauthors. I made the figures and tables, wrote and submitted the manuscript.

The Chapter 4 of this thesis is based on the publication "Molecular dynamics simulation of the surface tension of aqueous sodium chloride: from dilute to highly supersaturated solutions and molten salt", which is available in an internationally leading journal of atmospheric science. I gave technical support in numerical modelling and calculation. I was involved in the discussions of the results, interpretation and implications and gave comments on the manuscript.

Besides these three main studies, this PhD project intersects one publication and one manuscript which either explore the underlying mechanisms of temperature-dependent surface tension in the gas-liquid interface or the size-dependent vapor pressure and surface tension of water nanodroplets. In the two co-author studies, I was involved in numerical modelling and calculation as well as result discussion,

manuscript revisions and publications. An overview of the key topics of this PhD project and the concepts that connect them is shown (Fig. 1-2).

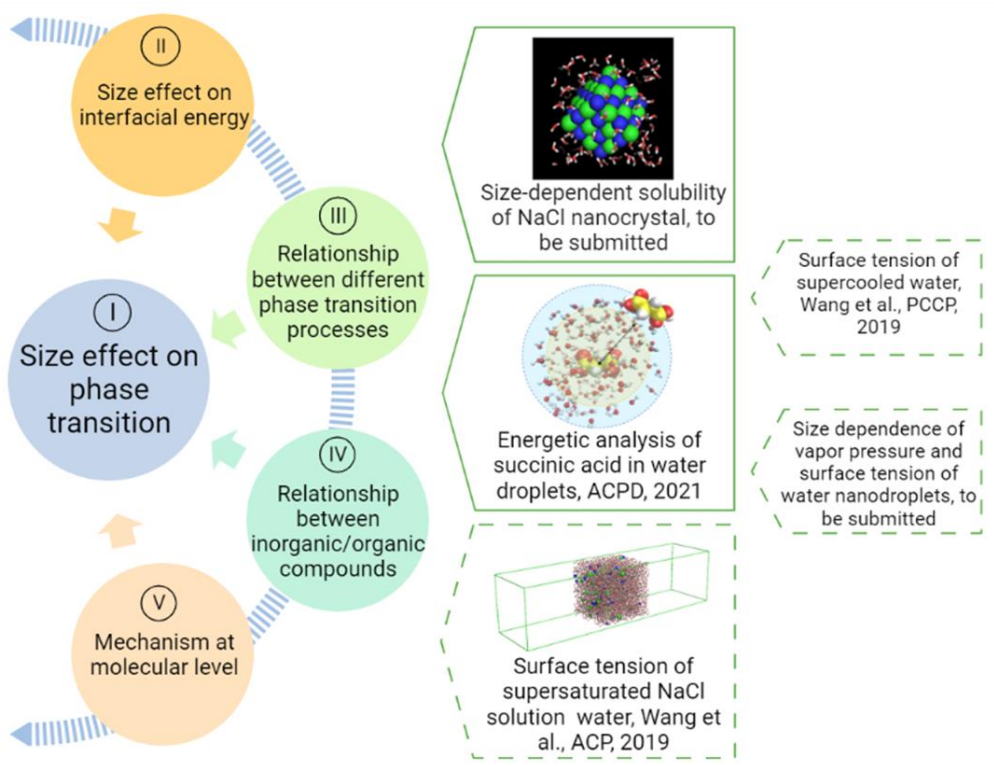

Figure 1-2: **Structure of this thesis.** The left part presents the object of the project schematically. The middle and right parts summarize the individual studies under the main topic of nano-size effect on phase transition of aerosol particles based on the molecular dynamics simulations. Here, solid line boxes indicate first-author papers and dashed boxes indicate co-authored papers.

2. Size-dependent solubility of NaCl nanocrystal in aqueous droplet

This work is to be submitted as Chen et al. (2021):

Chen, C., Wang, X., Binder, K., Pöschl, U., Su, H., and Cheng, Y.: Size-dependent solubility of NaCl nanocrystal in aqueous droplet, to be submitted

I am the first-author of this work and my contribution to this work includes performing the study, working out all of the technical details such as preparing sodium chloride and water force field files, running molecular dynamics simulations, analyzing the data, making the figures and tables, discussing the results, interpretation and implications and writing the manuscript.

The following text, figures, and tables quoted (within "") from page 18 to page 60 are exactly the same as the manuscript which is cited on page 17.

"**Abstract**

The solubility of nanoparticles is of fundamental importance in pharmaceutical industry, materials sciences, and atmospheric sciences, but the current understanding remains elusive to theory and experiment especially at the nano-scale. In particular, the size contribution of nanoparticles to the solubility and the structure of the corresponding nanodroplet of saturated solution have not been revealed. Here, the solubility of sodium chloride (NaCl) nanocrystals with volume equivalent diameters ranging from 0.51 to 1.75 nm is investigated by using molecular dynamics simulations with improved evaluation criteria, and the structure of the corresponding saturated aqueous nanodroplet is further analyzed. A significant size-dependent solubility of NaCl nanoparticles is observed in the simulations, which can be well predicted by combining the Ostwald-Freundlich equation and Gibbs-Duhem equation with consideration of size-dependent solid-liquid surface tension. Further structure analysis of the corresponding saturated aqueous nanodroplet shows that the concentration distribution of ions and water in saturated nanodroplet is inhomogeneous. The concentration of NaCl in the inner part of the nanodroplet is larger than the one near the surface. Moreover, the spatial structure of dissolved ions in the aqueous nanodroplet resembles the structure of molten NaCl nanoparticle at melting point, and the similarity grows when the size decreases. The melting point temperature of NaCl nanoparticles is size-dependent, as is the solubility of NaCl nanoparticles. The nanoparticle containing 7 pairs of NaCl ions is proved to be molten at 300 K. This indicates that when the particles are small enough, they can be considered as dissolved particles with infinite solubility at the room temperature. Overall, based on the size-dependent solubility of NaCl nanoparticles, the research provides a perspective to the inhomogeneous structure in corresponding saturated nanodroplets and the connection between dissolution and melting processes of solids, which may be useful for studies about nanoparticles in various fields, such as atmospheric science, material science and chemical engineering.

Significance

Particle size is an important parameter in the equilibrium phase diagram of aerosol nanoparticles. An improved evaluation criteria to distinguish between solid and liquid NaCl nanoparticles is introduced to help quantitatively predict size-dependent solubility of NaCl nanocrystal in aqueous nanodroplets. The corresponding saturated nanodroplet shows an inhomogeneous distribution of ions and water molecules. As the NaCl nanoparticles become smaller, the dissolved NaCl in the saturated aqueous nanodroplet begins to show some structural similarity to the molten NaCl at the melting point. When the nanoparticles are small enough, they can be considered as dissolved particles with infinite solubility at the room temperature. These findings will help to improve aerosol parameterization in aerosol and climate predictions as well as the understanding of nanomaterials in material science and chemical engineering.

Introduction

The solubility of solids in water is one of the most fundamental physicochemical properties for many physical processes, such as the absorption of drugs, nucleation in the solution and hygroscopic growth of atmospheric nanoparticles (Müller et al., 2001; Thanh et al., 2014; Cheng et al., 2015). In addition to chemical composition, temperature and relative humidity, particle size has been recognized as one of the main factors in regulating the solubility of nanoparticles (Harbury, 1946; Müller and Peters, 1998; Ostwald, 1900; Freundlich, 1922). For example, size-dependent solubilities of sodium chloride (NaCl) and ammonium sulfate (AS) nanoparticles with diameter ranges from ~6 to ~60 nm in the aqueous nanodroplet are observed respectively based on experiments (Biskos et al., 2006a; Biskos et al., 2006b), and these dependences are explained by the Ostwald-Freundlich effect (Cheng et al., 2015). Besides, molecular dynamics (MD) simulations predict that the solubility of ~6 nm NaCl nanoparticles is about 1.5 higher than the macroscopic NaCl in bulk water solution (Espinosa et al., 2016). An increasing dissolution rate of NaCl residual crystal (≤200 ions, diameter ≤~2 nm) is also found by MD simulations, indicating a higher solubility of smaller NaCl nanodroplets (Lanaro and Patey, 2015). However, very few quantitative studies on size-dependent solubility of nanoparticles with a diameter of less than 2 nm in the aqueous droplet currently exist, even for the well-studied salt substances.

The reason for the few quantitative studies is mainly due to a lack of reliable thermodynamic parameters, such as surface tension. It is difficult to directly measure surface tension in the highly supersaturated critical nanodroplets. For probe experiments, heterogeneous nucleation on the contact surface leads to uncertainty of measurement results (Gast and Adamson, 1997). For substrate-free experiments, a nanosized range is still unreachable due to the limitation of techniques (Tang et al., 1986; Chan et al., 1997; Vicente et al., 2002). In addition, there is still discussion regarding whether the solid-liquid interfacial energy of nanoparticles and that of solute embryos should be expected to close to each other (Cohen et al., 1987; Gao et al., 2006; Gao et al., 2007). Solid-liquid surface tension of salts is derived from the Differential Köhler Analysis (DKA)-based thermodynamic data with the Gibbs-Duhem equation and the Ostwald-Freundlich equation, and it is then used to determine the size-dependent solubility of the solute (Cheng et al., 2015). They report that the solid-liquid interface energy of salt nanoparticles shows no significant difference for particles larger than 6 nm, but decreases for embryos, which seems to be in line with the size dependence of interfacial energy. Nevertheless, the magnitude and the underlying mechanisms of the size effect on the interfacial energy for particles below 6 nm remain inaccessible in the current thermodynamic models. Bahadur et al. (2008a; 2008b) conduct two MD simulation approaches, the energy difference method and the test area method, to determine the surface tensions (NaCl-air, NaCl-solution and solution-air) of particles ranging in size from 2 to 10 nm. With the Tolman equation fitting, the surface tension is proved to remain close to the planar surface tension except for particles smaller than 2 nm. However, the two methods of Bahadur et al. (2008a; 2008b) do not yield identical surface tension values.

Except for the issue of size-dependent surface tension of critical nanodroplets, the distribution of ions and molecules in highly concentrated nanodroplet in the critical state is still ambiguous. An increased solubility of smaller nanoparticles indicates the liquid and well mixed state compared to bulk materials, which has a similar linear inverse dependence on the bulk phase transition temperature for salt solutions (Virtanen et al., 2010; Koop et al., 2011; Cheng et al., 2015). Possible morphologies of aerosol particles in the accumulation mode size regime including homogeneous, partially engulfed, and core-shell structures are observed by current technologies (Krieger et al.,

2012). However, studies of the size-dependent structure of critical highly concentrated nanodroplets in the nucleation mode size regime are still scarce.

Here, the size-dependent solubility of NaCl nanoparticles (diameter ranges from 0.507 to 1.745 nm) in water droplets is investigated, as well as size-dependent solid-liquid surface tension and structures under the corresponding critical conditions by classic MD simulations. Firstly, an improved detection approach is developed to directly distinguish solid-like and liquid-like structures of NaCl nanoparticles in water droplets in the MD simulations. With this approach, the solubility range of a certain size of NaCl nanoparticles is determined. Then, size-dependent solid-liquid surface tension and solubility of critical NaCl nanoparticles are predicted based on the discrete solubility range data with the Gibbs-Duhem equation, the Ostwald-Freundlich equation and the Tolman equation. Furthermore, the structure of the corresponding saturated aqueous nanodroplet is analyzed to compare the distribution of ions and water in highly saturated nanodroplets of different sizes. Eventually, the connection of dissolution and melting processes is discussed to give a new perspective for phase transition of solids.

Results

Size-dependent solubility of NaCl nanoparticles

A strong size dependence is shown for NaCl particles with diameters larger than 0.665 nm (13 pairs of NaCl ions) (red and orange bars in Fig. 1) according to the improved q_8 detection approach. At particle diameter equal to 0.665 nm with 13 pairs of NaCl ions, the saturation mass fraction is ~3.2 times higher than the simulated saturation mass fraction of bulk NaCl particle (gray circle in Fig. 1) (Berendsen et al., 1987; Joung and Cheatham III, 2008; Aragones et al., 2012; Moucka et al., 2013; Espinosa et al., 2016). The trend is qualitatively consistent with the experimental results (green triangles in Fig. 1) (Cheng et al., 2015). The simulated solubility data are a bit lower compared to the experiment data, where the experimental saturation mass fraction of bulk NaCl (brown triangle in Fig. 1) is ~1.5 times higher than the simulated saturation mass fraction of bulk NaCl.

Size-dependent solubility based on the simulations cannot be explained by the combination of the Ostwald-Freundlich and Gibbs-Duhem equation with a single bulk solid-liquid surface tension ($\sigma_{\mathrm{sl,bulk}}$) (Eq. 3). The prediction curve obtained based on the single $\sigma_{\mathrm{sl,bulk}} = 102$ mN m^{-1} and the bulk saturation mass fraction ($\chi^*_{\mathrm{s,bulk}}$)

calculated by MD simulations (Bahadur and Russell, 2008a) (pink line in Fig. 1) does not fit the data well. This indicates that the simulated solubility data become sensitive to σ_{sl} as the crystal gets small. Therefore, the size-dependent solid-liquid surface tension of NaCl nanoparticles should be under consideration for the size-dependent solubility of NaCl nanoparticles.

The saturation mass fraction (χ_s^*) of NaCl particles with diameters less than 0.665 nm does not vary monotonically. The saturation ratio ($\chi_s^*/\chi_{s,bulk}^*$) remains similar when the diameter of the crystal decreases from 0.665 to 0.530 nm, with 13 to 8 pairs of NaCl ions. Subsequently, the ratio suddenly jumps to ~5.61 when the diameter of the crystal drops to 0.507 nm (7 pairs of NaCl ions), where the particle is thought as the dissolved NaCl with infinite solubility. This result is consistent with that in the melting process simulations, where the NaCl particle with 7 pairs of NaCl ions is supposed to be molten at 300 K.

By considering the size-dependent solid-liquid surface tension (σ_{sl}) based on the second-order Tolman equation (Supplementary Note 3), size-dependent solubility based on the simulations is well explained by the combination of the Ostwald-Freundlich and Gibbs-Duhem equations (blue shaded curves in Fig. 1). Compared to the fitting curves from the first-order Tolman equation (light pink shaded curves in Fig. 1), the blue fitting curves well capture the solubility pattern. In addition, the size-dependent surface tension competes with the effect of crystal size on the solubility of nanoparticles. The reduction in particle size contributes to an increase in solubility, but this gain is inhibited by the presence of the size effect on the surface tension, particularly when the particles are smaller than 0.665 nm with 13 pairs of NaCl ions.

Structures of NaCl nanoparticles at different dissolution states

By examining the structures of NaCl nanoparticles at three states of dissolution: the incomplete, critical, and complete dissolutions are examined, it is discovered that the distribution of ions and water molecules is inhomogeneous in the incomplete and critical dissolution state, but close to homogeneous in the complete dissolution state. The droplet composed by 32 pairs of NaCl ions (corresponding to 1 nm diameter) with 100 to 160 water molecules is taken as an example, where the particle containing 110-130 water molecules is in the critical dissolution state. As shown by the light red lines in Fig. 2, in the incomplete dissolution state, both Na^+ and Cl^- ions are primarily

distributed within ~1 nm distance from the center of mass (COM) of the particle, and more concentrated within distances ~0.4 nm. Na^+ ions have the highest density distribution at ~0.3 nm distance from the COM, while Cl^- ions are concentrated at the COM and ~0.4 nm distance from the COM. Meanwhile, water molecules are distributed at distances >0.4 nm and mostly concentrated at distances ~1 nm distance from the COM. As shown by the red and blue lines in Fig. 2, in the critical dissolution state, the concentration distribution of Na^+ and Cl^- ions becomes similar but not homogeneous, and the concentration of ions decrease gradually from the COM to the particle surface. Water molecules are concentrated at the position closer to the COM compared to that in the incomplete dissolution state, and individual water molecules enter the interior of the particle (<0.4 nm distance from the COM). This shows that only a few water molecules are required to destroy the crystal structure inside the NaCl nanoparticle, where saturation can be much higher than that on the surface of the particle. As shown by the light blue lines in Fig. 2, in the complete dissolution state, the distribution of Na^+ and Cl^- ions is even more similar. This indicates that the distribution of ions and water molecules would be homogeneous when the mass saturation of NaCl particle is close to the bulk mass saturation. Note that, the fixed COM position of the total system in the MD algorithm might cause small fluctuations of the nanocrystal position relative to the total COM, which may give rise to some smearing of the profiles of the ions and water molecule densities near the COM of the total system.

The structure of different-size droplets in the critical dissolution state is further analyzed to quantify the characteristics of the inhomogeneity distribution of ions and water. The saturated droplet composed of 32 pairs of NaCl ions (corresponding to 1 nm diameter) with 130 water molecules is taken as an example. As shown in Fig. 3a, the profile of number density of ions and water molecules at different distances from the center of mass (COM) indicates ions are highly concentrated in the area around the COM of droplet and are more diluted in the area near the surface. For example, the profile of the number of ions and water molecules at different distances from the COM in this droplet suggests only ~4 water molecules exist in the area around the COM of droplet with radius of 0.5 nm, while there are 16 ions in the same area (Fig. 3b). The two-dimensional density map of the relative fraction of ions shows more visually the gradient distribution of the ions (Fig. 3c). Except for a thin interface where no ion exists, the bulk solution with concentration of 14.4 mol kg^{-1} is homogeneous. This is similar

to the result from the previous simulation, where the smooth density profile of ions in the bulk solution with concentration of 11.48 mol kg^{-1} indicates the homogeneous structure of the system (Wang et al., 2018). By contrast, the droplet composed of 32 NaCl and 130 water molecules shows inhomogeneity of the ion/water distribution with a gradient. The concentration becomes larger when the position is closer to the center. Furthermore, the distribution of Na^+ and Cl^- ions is rather stratified. The bidimensional density map of the difference of the relative fraction of Na^+ and Cl^- ions (Fig. 3d) shows that Na^+ ions are more concentrated in the center of the droplet while Cl^- ions are more concentrated at the surface of the droplet.

Discussion

Dissolution and melting processes of NaCl nanoparticles

By following the approach of Qi et al. (2001), the melting temperature for the nanocrystals above the size of 15 pairs is determined and the melting point of NaCl nanocrystal shows a significant size dependence (Supplementary Note 1). As shown in Fig. S8, the heat capacity (blue circles) is obtained from the derivative of the average potential energy (red circles) with respect to the temperature based on Eq. S1, and the melting temperature of each crystal is at the temperature with the maximum apparent heat capacity. Above the size of 15 pairs of NaCl nanocrystals, the depression of melting point of nanocrystals in comparison to the bulk is quite proportional to $N^{(-1/3)}$, showing a significant size dependence (red dashed line in Fig. S9). This phenomenon also occurs in other substances, i.e., pure metal and alloy nanoparticles (Couchman and Jesser, 1977; Qi et al., 2001; Chen et al., 2011). The dependence can be derived from the decrease of phase stability of nanoparticles due to surface effects (Jiang and Yang, 2008). By using the q_8 calculation, the melting point of NaCl nanocrystals is also determined (blue diamonds in Fig. S9). The results shows that above the size of 8 pairs of NaCl nanocrystals, the melting point depression of nanocrystals is proportional to $N^{(-1/3)}$ (blue dashed line in Fig. S9). The approach of Qi et al. (2001) cannot lead to the melting point for the NaCl nanocrystals below the size of 15 pairs. Note that the melting point for the NaCl nanocrystals below the size of 15 pairs is already less than the Debye temperature, and the heat capacity no longer follows the Dulong-Petit law. The vibrations of the atoms must be under consideration for the accurate heat capacity data.

By comparing the average potential energy of dissolved and molten NaCl nanoparticles with diameter below 6 nm, it shows that the structure of dissolved NaCl in saturated solution becomes similar to the structure of molten NaCl when the NaCl particle size decreases. The average potential energy of NaCl (μ_{NaCl}) only depends on the relative position of the ions (Joung and Cheatham III, 2008), so that it can reflect the spatial distribution of ions. The average potential energies in different simulated systems are compared to analyze the similarity of NaCl in the dissolved state and molten state quantitatively (Fig. 4). Dark circles represent μ_{NaCl} in the molten NaCl particles at respective melting points, and the values are all close to -700 kJ mol^{-1} (grey line). This means the spatial distribution of ions in the molten NaCl particle at the respective melting point is almost the same and independent of size. This phenomenon also works for other substances, such as copper (Delogu, 2005). However, μ_{NaCl} in the dissolved droplets at the critical dissolution state (blue circles) decreases with the decrease of diameter. The blue circles approach to -700 kJ mol^{-1} and deviate from the blue dashed line (≈ -358.35±20.95 kJ mol^{-1}), which represents μ_{NaCl} in bulk saturated solution. It suggests the structure similarity of dissolved NaCl in saturated nanodroplets to molten NaCl at melting point increases when the size of NaCl particle decreases. The red circles represent μ_{NaCl} of NaCl nanoparticles at 300 K, which deviate from the red line that represents μ_{NaCl} of bulk NaCl crystal (≈ -780 kJ mol^{-1}). The increase of μ_{NaCl} with the decrease of particle size means the bigger particle is more stable and thus has a higher melting point temperature. The trends of red circles and blue circles almost meet at near -700 kJ mol^{-1} which represents μ_{NaCl} of 7 pairs of NaCl ions at melting point as other molten nanoparticles. This means that 7 pairs of NaCl ions at 300 K in the molten state can be considered as the dissolved NaCl nanoparticle with infinite solubility. Due to the size-dependent solubility, smaller molten NaCl particles at 300 K (≤7 pairs of NaCl ions) are also considered as dissolved NaCl with the same size and infinite solubility.

The radius of gyration of particles and the radial distribution function of ions to ions ($RDF_{ion\text{-}ion}$) also supports the analysis of μ_{NaCl}. The similarity of the radius of gyration of NaCl particles in the dissolution and melting processes becomes more pronounced when the particle size decreases (Fig. 5). The similarity of relative positions of ions in the dissolution and melting processes increases when the particle size decreases (Fig. S10). Harbury (1946) gave a similar assumption that there is a

significant comparability between supersaturated solution and undercooled melts. In total, the dissolution of bulk NaCl solids is a traditional dissolution while the dissolution of NaCl particles at nanoscale is analogous to the melting process of NaCl particles at the nanoscale. And these two different types of phase transition, dissolving and melting, "meet" at ≤7 pairs of NaCl ions at 300 K.

The radial distribution functions of Na^+ to Na^+ ($RDF_{Na\text{-}Na}$), Cl^- to Cl^- ($RDF_{Cl\text{-}Cl}$), $Na^+$to Cl^- ($RDF_{Na\text{-}Cl}$), and Cl^- to Na^+ ($RDF_{Cl\text{-}Na}$) give valuable additional information that the q_8-determined solubility and melting point of NaCl nanocrystals are on firm ground. The $RDF_{Na\text{-}Na}$ and $RDF_{Cl\text{-}Cl}$ of the q_8-determined unmelted NaCl nanocrystals and undissolved NaCl in saturated nanodroplets show rather sharp peaks at the first to fourth nearest neighbor distances of ~0.40 nm, ~0.56nm, ~0.69 nm, and ~0.79 nm (Fig. S12 and S14). The $RDF_{Na\text{-}Cl}$ and $RDF_{Cl\text{-}Na}$ of the q_8-determined unmelted NaCl nanocrystals and undissolved NaCl in saturated nanodroplets show the same sharp peaks at the first to fourth nearest neighbor distances of ~0.28 nm, ~0.49 nm, ~0.63 nm, and ~0.84 nm (Fig. S16 and S18). This is well compatible with the simple predictions from the snapshot of 9 pairs of NaCl crystal shown in the Fig. S19, indicating that the nanocrystals are still crystalline despite their smallness, and the crystal structure is not disturbed by the condensation of a few water molecules. Meanwhile, The $RDF_{Na\text{-}Na}$ and $RDF_{Cl\text{-}Cl}$ as well as the $RDF_{Na\text{-}Cl}$ and $RDF_{Cl\text{-}Na}$ of the q_8-determined molten NaCl nanocrystals at the melting points and dissolved NaCl in saturated nanodroplets show flatter peaks compared to the ones of the ummelted and undissolved NaCl nanoparticles (Fig. S11, S13, S15, S17). This captures well the different structural features between the solid and liquid state of NaCl, in agreement with the previous studies (Li et al., 2021; Lide, 2004; Fuentes-Azcatl and Barbosa, 2016), thus supporting the results of the solubility and melting point of NaCl nanoparticles determined by the q_8 method. Snapshots of NaCl nanoparticles during the melting and dissolution processes in Fig. S20 support the solubility and melting point of NaCl nanoparticles determined by the q_8 method as well. The snapshots of NaCl nanoparticles at the temperature lower than the q_8-determined melting points show that the typical shape of nano-sized NaCl nanocrystals is not spherical. Both in the case of melting and dissolution process, spherical shape occurs only when the transition to the fluid phase takes place.

Implications

The simulations demonstrate that the solubility of NaCl at nanoscale is size-dependent and can be much higher than the one of a bulk solution. The melting point of NaCl is also found to be size-dependent in the study. To transform a NaCl particle with a temperature of 300 K into liquid state, the temperature of the environment should be increased or water should be added to the NaCl. In these processes, heat from a higher-temperature environment or the interaction with water molecules changes the NaCl crystal to the liquid state. In other words, the heat, and the interaction with water for NaCl nanocrystals are equivalent. As the size decreases, a lower temperature or less surrounding water molecules are needed to change the phase of NaCl. The nanoparticle with only 7 pairs of NaCl ions cannot exist in the solid state at 300 K, thus no heat or interaction with a few water molecules is needed to transform it into liquid. Overall, this study can provide a new perspective to connect the dissolution and melting processes of NaCl nanoparticles, and this connection may also be suitable for other solids. For a substance whose melting point is higher than 300 K at macroscopic level, there exists a critical diameter (D_c) at which the melting point is 300 K. Naturally, when the diameter of the nanoparticle composed by this substance is below D_c, the particle is expected to be liquid at room temperature. The nanoparticle whose diameter is larger than D_c is solid at room temperature, while a small amount of adsorbed water molecules can turn it into a molten-like liquid with a thin solution coating. These general principles may be useful for studies about nanoparticles in various fields, including the environmental, pharmaceutical and materials sciences (Rabinow, 2004; Koop et al., 2011; Suo et al., 2013).

Especially for the atmospheric environment, the structure of highly concentrated solution droplet as shown in this study (Fig. 3c) might exist and could lead to an uncertainty to evaluate the effect of aerosols on climate. In the traditional opinions, atmospheric aerosols can grow up by absorbing water molecules from the air when the relative humidity (RH) is higher than a threshold value (Biskos et al., 2006a; Biskos et al., 2006b). After that, the aerosol with homogeneous solution exists. When the RH is lower than the threshold value, the aerosol would keep dry or adsorb few water molecules on the surface. According to this study, an aerosol can absorb a few water molecules and change to become a highly condensed core with a diluted solution coating. Thus, more studies should be performed to examine if the aerosol composed

by a highly condensed salt or organic core and a coating (diluted solution or even pure water) really exists stably in the atmosphere. And topics involving the effect on climate should also be investigated in the future, i.e., the albedo of aerosol with different coating structures.

Methods

MD simulation details

The JC force field for NaCl with SPC/E water model has been proved to nicely predict the experimental value of solubility (~6.15 mol kg^{-1}) (Berendsen et al., 1987; Joung and Cheatham III, 2008; Aragones et al., 2012; Moucka et al., 2013; Espinosa et al., 2016). Therefore, this force field combination is applied in the study to simulate the NaCl-water mixture. The MD simulations are carried out with the GROMACS 2016.6 package (Van Der Spoel et al., 2005; Abraham et al., 2015). NaCl nanocrystals with different diameters are surrounded by certain water molecules initially. The systems are then energetically minimized by the steepest-descent method and equilibrated for 100 ps at 300 K. The MD simulations are further performed in the *NVT* ensemble with periodic boundary conditions and velocity-rescaling thermostat. Electrostatic interactions are calculated using the particle mesh Ewald (PME) algorithm, and van der Waals interactions are accounted for up to a cutoff distance of 10 Å. All simulations are carried out for at least 600 ns using a 1 fs time step, and conformations for analysis are saved every 2 ps. More detailed information about the initial structure setup and simulation times are shown in Table S1.

In this study, the melting processes of NaCl nanocrystals is also simulated. The JC force field is adopted to keep synchronous with the simulations of NaCl dissolution process. The particles with different diameters are simulated at different temperatures to determine the melting point. More details about the setup are shown in Supplementary Note 1.

NaCl solid to liquid judging criteria

The NaCl nanocrystal is considered as dissolved or molten when the time average of the q_8 value of each ion in the crystal is less than 0.35. q_8 is the local bond-orientational order parameter to provide the best separation between solid-like (>0.35) and liquid-like (≤0.35) state of each NaCl ion in the nanoparticles (Fig. S5).

Since at 300 K the crystal structure of NaCl is already close to perfectly rigid, also a simple study of the radial pair distribution functions between the different pairs of ions gives a clear identification which NaCl clusters are still in a nanocrystal state and which are already in a liquid state (Fig. S6).

q_8 calculation for ions

In order to detect the dissolution and melting progress of NaCl nanocrystal, it is necessary to distinguish ions that are in the solid-like and liquid-like structures. To do this, the local order parameter approach of Steinhardt et al. (1983) is followed. For each ion (i), the local bond-orientational order parameter $q_l(i)$ is calculated as

$$q_l(i) = \left[\frac{4\pi}{2l+1}\sum_{m=-l}^{l}|q_{lm}(i)|^2\right]^{\frac{1}{2}} \quad (1)$$

and

$$q_{lm}(i) = \frac{1}{N}\sum_{j=0}^{N} Y_l^m\left(\theta(r_{ij}), \emptyset(r_{ij})\right) \quad (2)$$

where l is a free integer parameter and m is an integer that runs from m = -l to l. Y_l^m is the spherical harmonic, r_{ij} is the position vector of the neighbor ion (j) with respect to the central ion (i), $\theta(r_{ij})$ and $\emptyset(r_{ij})$ are the polar and azimuthal angles with respect to the reference coordinate of r_{ij}. N is the number of neighbors of ion. Note that in the perfect bulk NaCl crystal structure, each ion has 6 nearest neighbors of different species (e.g., Na^+ has 6 neighboring Cl^- and vice versa) and 12 next-nearest neighbors of the same kind (e.g., Na^+ has 12 neighboring Na^+). However, the NaCl nanoparticle structures during melting and dissolution processes in the simulations are mostly not perfect crystal structures. Therefore, here the ions are considered to be identical and the number of neighbors of ion is equal to 12. Lanaro and Patey (2016) utilized a similar method to track the production of NaCl nuclei in aqueous solutions. Jiang et al. (2019) also used this approach to investigate the mechanism of NaCl crystal nucleation from solutions with high supersaturations. The parameter $q_l(i)$ is sensitive to different crystal symmetries depending on the choice of l. $q_l(i)$ distributions for $l = 4$, 6, and 8 were examined, using the cubic nanocrystal with 108 pairs of NaCl in the solid phase and the dissolved state as representative of the liquid phase at 300 K. As shown in Fig

S1, the local bond-orientational order parameter $q_8(i)$ provides the best separation between solid and liquid phase distribution for NaCl nanoparticles.

Size-dependent solubility estimation

Size-dependent solubility is discussed based on the combination of the Ostwald-Freundlich (Ostwald, 1900; Freundlich, 1922) and Gibbs-Duhem equations (Cohen et al., 1987; Richardson and Snyder, 1994; Seinfeld et al., 1998) as

$$D = -\frac{4\nu\sigma_{\mathrm{sl}}}{RT\int_{x_{\mathrm{s,bulk}}^{*}}^{x_{\mathrm{s}}^{*}} M\frac{1-x_{\mathrm{s}}}{x_{\mathrm{s}}}dlna_{\mathrm{w}}} \tag{3}$$

where R is the universal gas constant, T is the temperature, ν is the molar volume of NaCl solid phase (atomic volume) given as 2.7×10^{-5} m^3 mol^{-1}, and M is the molar weight of solute. $x_{\mathrm{s,bulk}}^{*}$ is the mass fraction of solute in a saturated bulk solution, and $a_{\mathrm{s,bulk}}^{*}$ is the solute activity at $x_{\mathrm{s,bulk}}^{*}$. x_{s}^{*} is the mass fraction of solute in a saturated droplet. a_{w} is the water activity retrieved from modified TM model (Supplementary Note 2). σ_{sl} is the size-dependent solid-liquid surface tension estimated by Tolman equation (Supplementary Note 3). In this study, D is the volume equivalent diameter of NaCl crystal at the saturation dissolution point, which equals to the diameter of the NaCl droplet of equivalent volume,

$$D = \sqrt[3]{\frac{6V}{\pi}} \tag{4}$$

and the volume of NaCl crystal (V) is measured based on the initial structure in the MD simulations (Fig. S19), where the distance between Na^+ and Cl^- is 0.28 nm.

Structure analysis

The profiles of number density and number of ions and water molecules at different distances from the center of mass (COM) are used to analyze the structure of saturated droplets. The relative fraction of ions is calculated by the following equation:

$$RFI = \frac{\rho_{\mathrm{ion.area}}/\rho_{\mathrm{water.area}}}{\rho_{\mathrm{ion.total}}/\rho_{\mathrm{water.total}}} \tag{5}$$

where $\rho_{\mathrm{ion.area}}$ represents the number density of NaCl in a spherical shell area, $\rho_{\mathrm{water.area}}$ represents the number density of water in a spherical shell area, the thickness of the spherical shell is 0.02 nm. $\rho_{\mathrm{ion.total}}$ represents the number density of NaCl in the entire droplet, $\rho_{\mathrm{water.total}}$ represents the number density of water in the entire droplet.

The radial distribution functions (RDFs) of ions with respect to other ions can reflect the spatial distribution of ions (Van Der Spoel et al., 2005; Hess et al., 2010). They are calculated as:

$$G_{\mathrm{ion-ion}}(r, t_o) = \frac{1}{500} \cdot \sum_{t=0.002}^{1} g_{\mathrm{ion-ion}}(r, t_{\mathrm{o}} + t) \tag{6}$$

Here, $g_{\mathrm{ion-ion}}(r)$ represents the RDF for one conformation:

$$g_{\mathrm{ion-ion}}(r) = \frac{1}{N_{\mathrm{ion}}} \cdot \sum_{i \in N_{\mathrm{ion}}}^{N_{\mathrm{ion}}} \sum_{j \in N_{\mathrm{ion}}}^{N_{\mathrm{ion}}} n(r_{\mathrm{ij}}) \tag{7}$$

r represents a given distance and the interval value is the thickness of a spherical shell equal to 0.02 nm, N_{ion} represents the number of ions for the given conformation, i and j represent the ions and $i \neq j$, r_{ij} represents the distance from ions i and ions j, $n(r_{\mathrm{ij}})$ represents the number of ions j locates in the distance of $r - 0.02\ nm$ to r from the given reference ion i. $G_{\mathrm{ion-ion}}(r, t_{\mathrm{o}})$ represents the average value of RDF from t_{o} to $t_{\mathrm{o}} + 1$ ns. As the simulation time step is 0.002 ns, $G_{\mathrm{ion-ion}}(r, t_{\mathrm{o}})$ can be considered as the average value of 500 conformations, $g_{\mathrm{ion-ion}}(r, t_{\mathrm{o}} + t)$ is the RDF at the time $t_{\mathrm{o}} + t$. In this study, $\mathrm{RDF_{ion\text{-}ion}}$ represents $G_{\mathrm{ion-ion}}(r, t_{\mathrm{o}})$. The profile of $\mathrm{RDF_{ion\text{-}ion}}$ over time can reflect the change of relative positions of ions during the process of dissolving.

Radius of gyration

Radius of gyration is defined as

$$R_{\mathrm{g}}^2 = \frac{1}{N} \sum_{\mathrm{i}} (R_{\mathrm{i}} - R_{\mathrm{COM}})^2 \tag{8}$$

where N is the number of ions in the cluster, R_{i} is the position of ion (i) and R_{COM} is the position of the center of mass of the cluster.

Average potential energy calculation

To calculate the average potential energy of dissolved or molten NaCl, the trajectories only containing the Na^+ and Cl^- ions after the MD simulations of a given NaCl-water system are extracted and then rerun for the new trajectories. In the rerun simulation, energy is calculated every 2 ps, and the average value over the time after the equilibrium of a system is taken to describe the system.

Figures

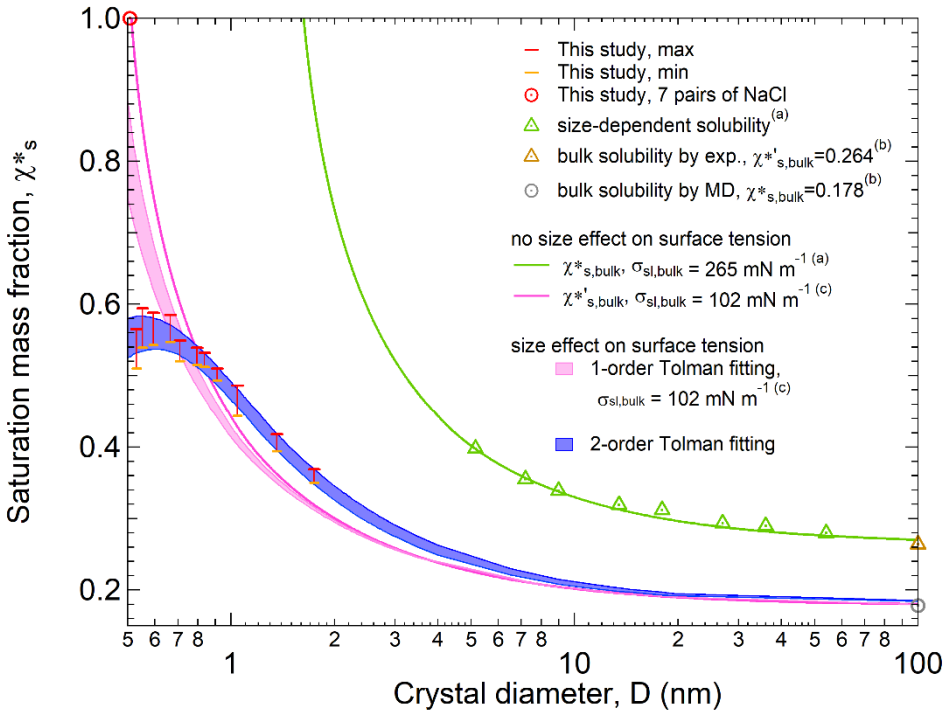

Figure 1. Size-dependent saturation mass fraction of NaCl nanoparticles at 300 K. The solubility range of NaCl nanoparticles is obtained from the MD simulations for particles with 8 to 108 pairs of NaCl ions (red and orange bars) and 7 pairs of NaCl ions (red circle). [(a)]The size-dependent solubility of NaCl nanoparticles is taken from experiments for particles with dry diameters of 5.18 to 54.2 nm (green triangles). [(b)]The NaCl bulk solubility from MD (grey circle) and from experiment (brown triangle) is taken from Espinosa et al. (2016). The size-dependent solubility curves are obtained based on the combination of the Ostwald-Freundlich and the Gibbs-Duhem equation with and without considering size effect on surface tension. The size effect on solid-liquid surface tension is considered based on the 2nd order Tolman equations for the light blue shaded curves. The size effect on solid-liquid surface tension is considered based on the 1st order Tolman equation with the bulk solid-liquid surface tension from Bahadur and Russell (2008a) for the light pink shaded curves. [(a)]The green curve without considering the size effect of surface tension is based on the NaCl bulk solubility by experiment and the bulk solid-liquid surface tension from Cheng et al. (2015). [(c)]The pink curve without considering the size effect of surface tension is based on the NaCl bulk solubility from MD and the bulk solid-liquid surface tension from Bahadur and Russell (2008a).

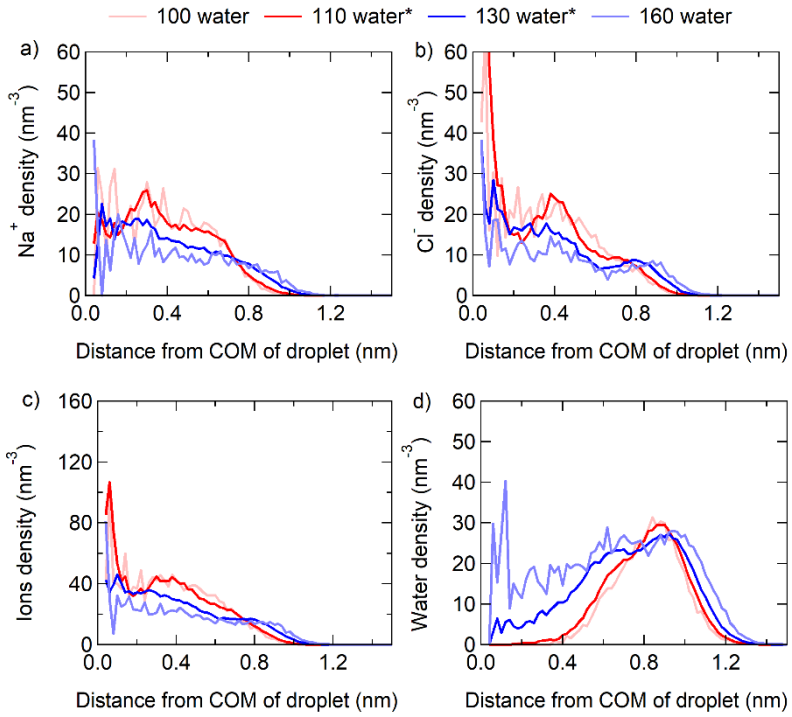

Figure 2. The number density profiles of ions and water molecules in the particles composed by 1 nm NaCl (32 pairs) and different numbers of water molecules. (a) for Na^+ ions, (b) for Cl^- ions, (c) for ions, and (d) for water molecules. Particles with less than 110 water molecules are in the incompletely dissolved state (light red lines). Particles with 110-130 water molecules are in the critically dissolved state (red and blue lines). And particles with more than 130 water molecules are saturated NaCl aqueous nanodroplets (light blue lines).

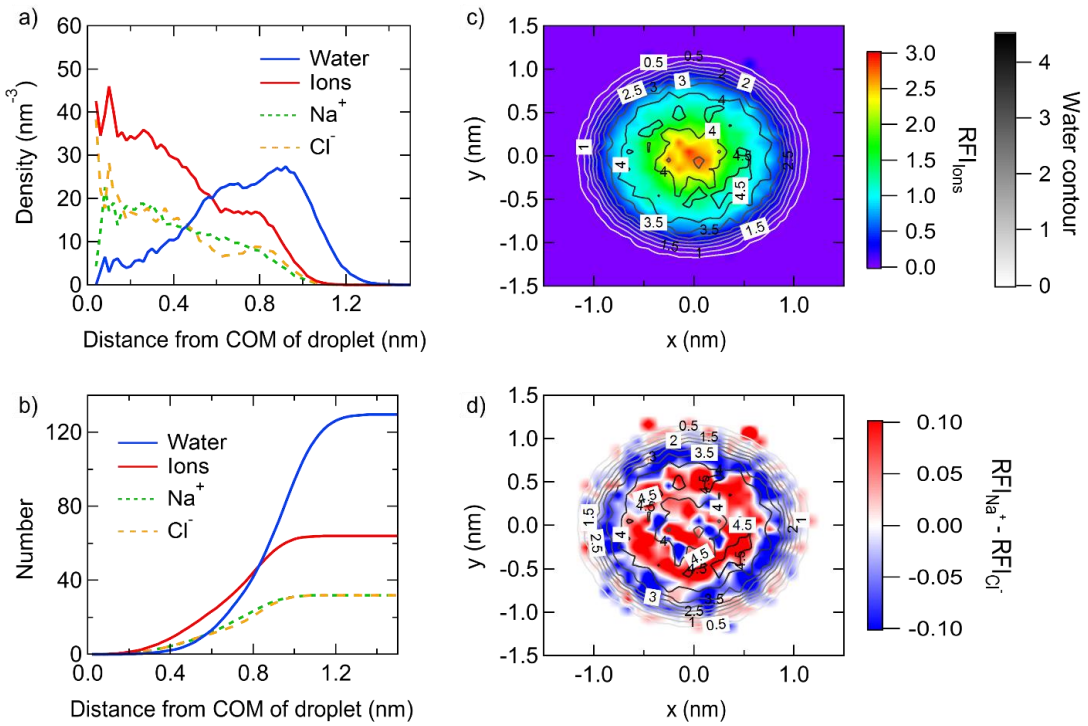

Figure 3. The distribution of ions and water molecules in the droplet composed by 1 nm NaCl and 130 water molecules. (a) The number density of ions and water molecules at different distance from COM in the droplet. (b) The cumulative number of ions and water molecules at different distances from COM in the droplet. (c) Two-dimensional density map of the relative fraction of ions. The contour lines represent the relative fraction of water molecules. (d) Two-dimensional density map of the difference of the relative fraction of Na^+ and Cl^- ions. The contour lines represent the relative fraction of water molecules.

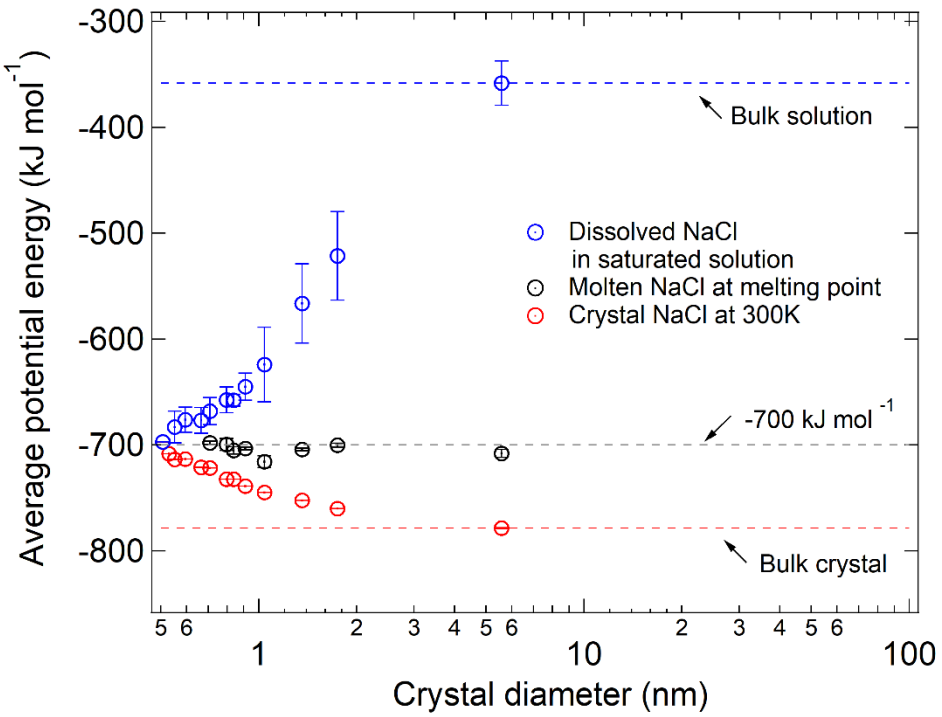

Figure 4. The average potential energy of NaCl (μ_{NaCl}) in solution, molten NaCl and crystal. Blue circles represent μ_{NaCl} in the saturated droplets at the critical dissolution state. The blue dashed line represents μ_{NaCl} in bulk saturated solution (≈ -358.35±20.95 kJ mol^{-1}). Black circles represent μ_{NaCl} in the molten NaCl at respective melting point, and the values are all near -700 kJ mol^{-1} (gray dashed line). Red circles represent μ_{NaCl} in crystal NaCl at 300 K, and the dashed red line is μ_{NaCl} in bulk NaCl crystal (≈ -780 kJ mol^{-1}).

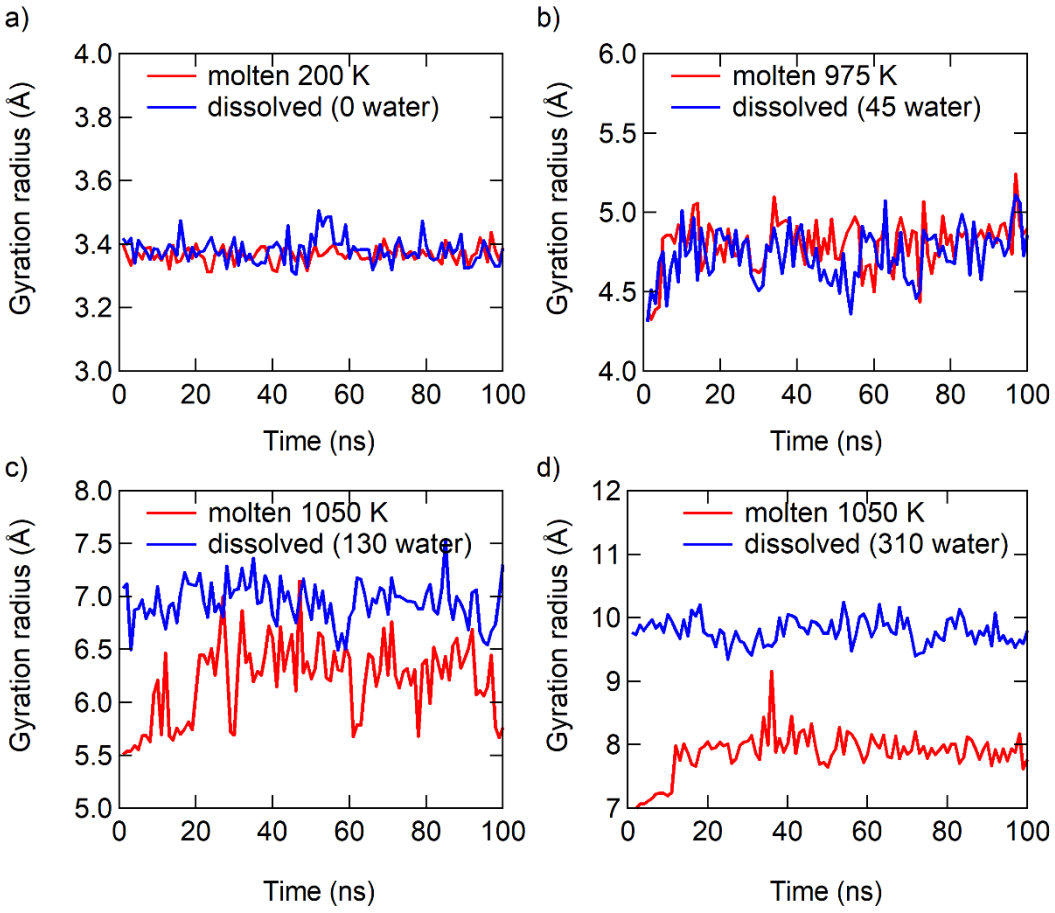

Figure 5. The radius of gyration of the molten NaCl and dissolved NaCl in saturated solution nanodroplets. (a) For 7 pairs of NaCl ions particles (diameter = 0.507 nm). (b) For 15 pairs of NaCl ions particles (diameter = 0.709 nm). (c) For 32 pairs of NaCl ions particles (diameter = 1.042 nm). (d) For 62 pairs of NaCl ions particles (diameter = 1.358 nm).

Supplementary Information

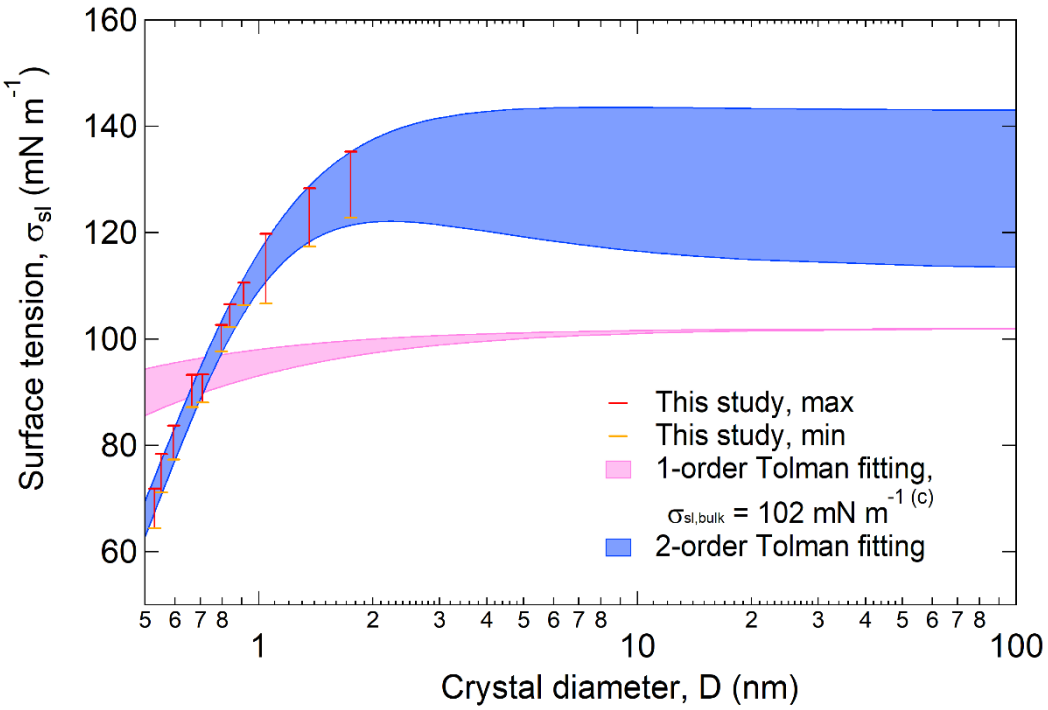

Figure S1. Size-dependent solid-liquid surface tension of NaCl nanoparticles at 300 K. The solid-liquid surface tension of NaCl nanoparticles is obtained from the MD simulated solubility data sets by the combination of the Ostwald-Freundlich equation with the Gibbs-Duhem equation (red and orange bars). The blue shaded curves are derived from the 2nd Tolman equation. (c)The light pink shaded curves are derived from the 1st order Tolman equation with the bulk solid-liquid surface tension from Bahadur and Russell (2008a).

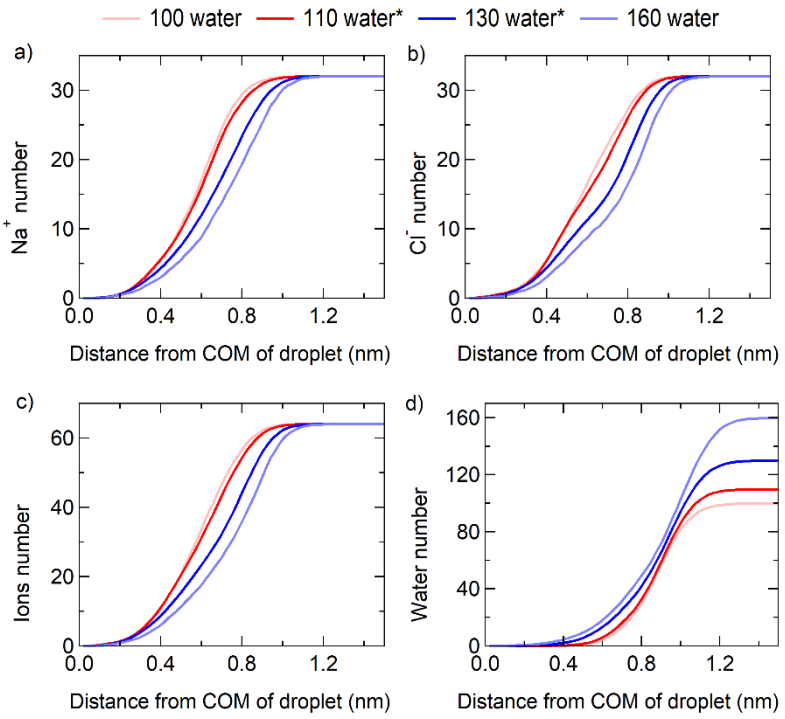

Figure S2. The cumulative number profiles of ions and water molecules in the particles composed by 1 nm NaCl (32 pairs) and different numbers of water molecules. (a) for Na^+ ions, (b) for Cl^- ions, (c) for ions, and (d) for water molecules. Particles with less than 110 water molecules are in the incompletely dissolved state (light red lines). Particles with 110-130 water molecules are in the critically dissolved state (red and blue lines). And particles with more than 130 water molecules are saturated NaCl aqueous nanodroplets (light blue lines).

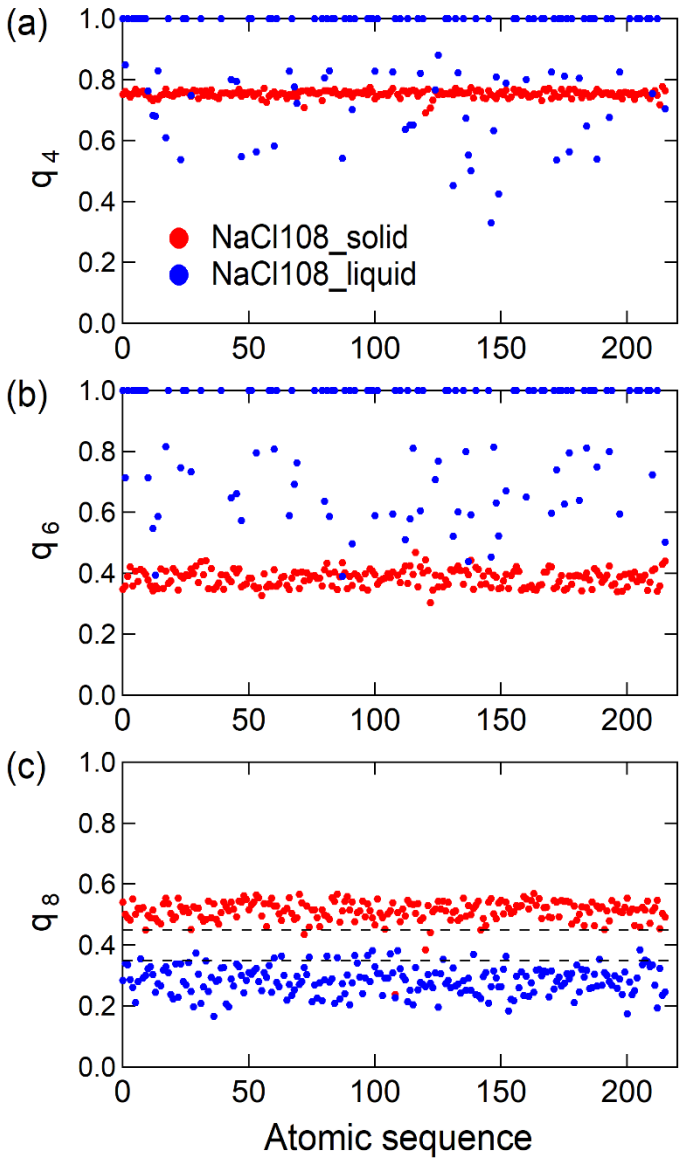

Figure S3. q_4, q_6, q_8 atomic distributions for the cubic nanocrystal with 108 pairs of NaCl in the solid phase and a dissolved state as representative of the liquid phase at 300 K. This figure indicates that q_8 provides the best separation between liquid and solid phase distributions compared to q_4 and q_6. The vertical dash line in (c) indicates the selected threshold ($q_8 = 0.35$).

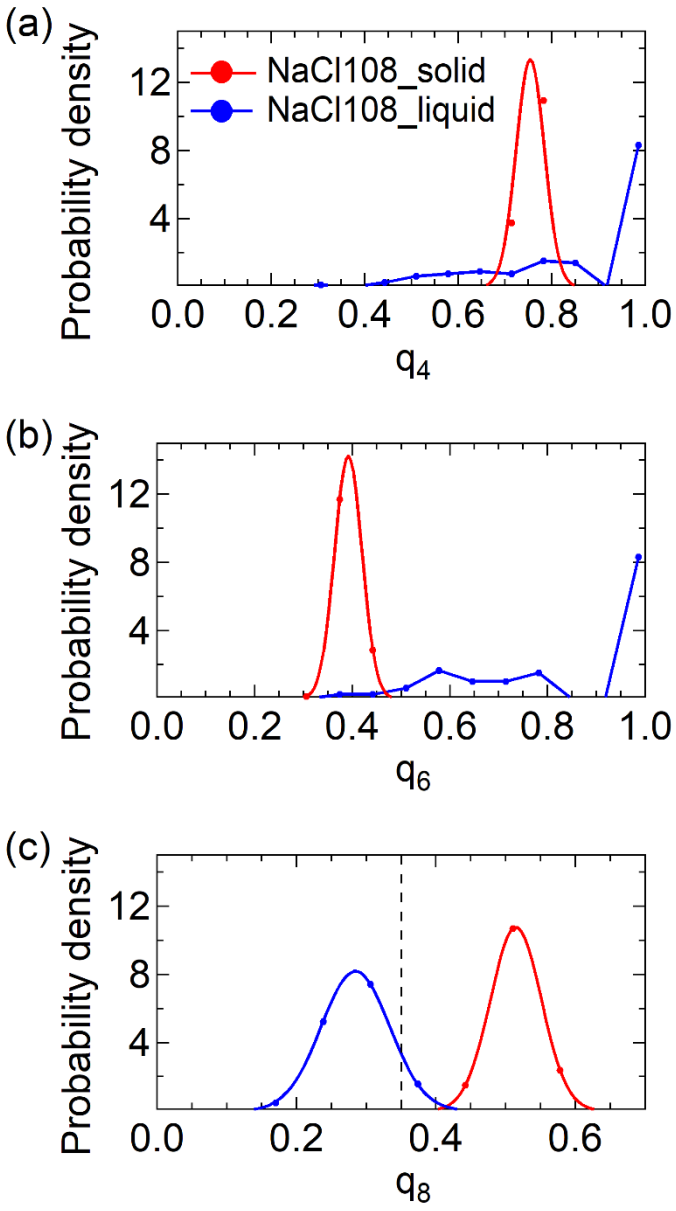

Figure S4. **q_4, q_6, q_8 probability density distributions for the cubic nanocrystal with 108 pairs of NaCl in the solid phase and a dissolved state as representative of the liquid phase at 300 K.** This figure indicates that q_8 provides the best separation between liquid and solid phase distributions compared to q_4 and q_6. The vertical dash line in (c) indicates the selected threshold (q_8 = 0.35).

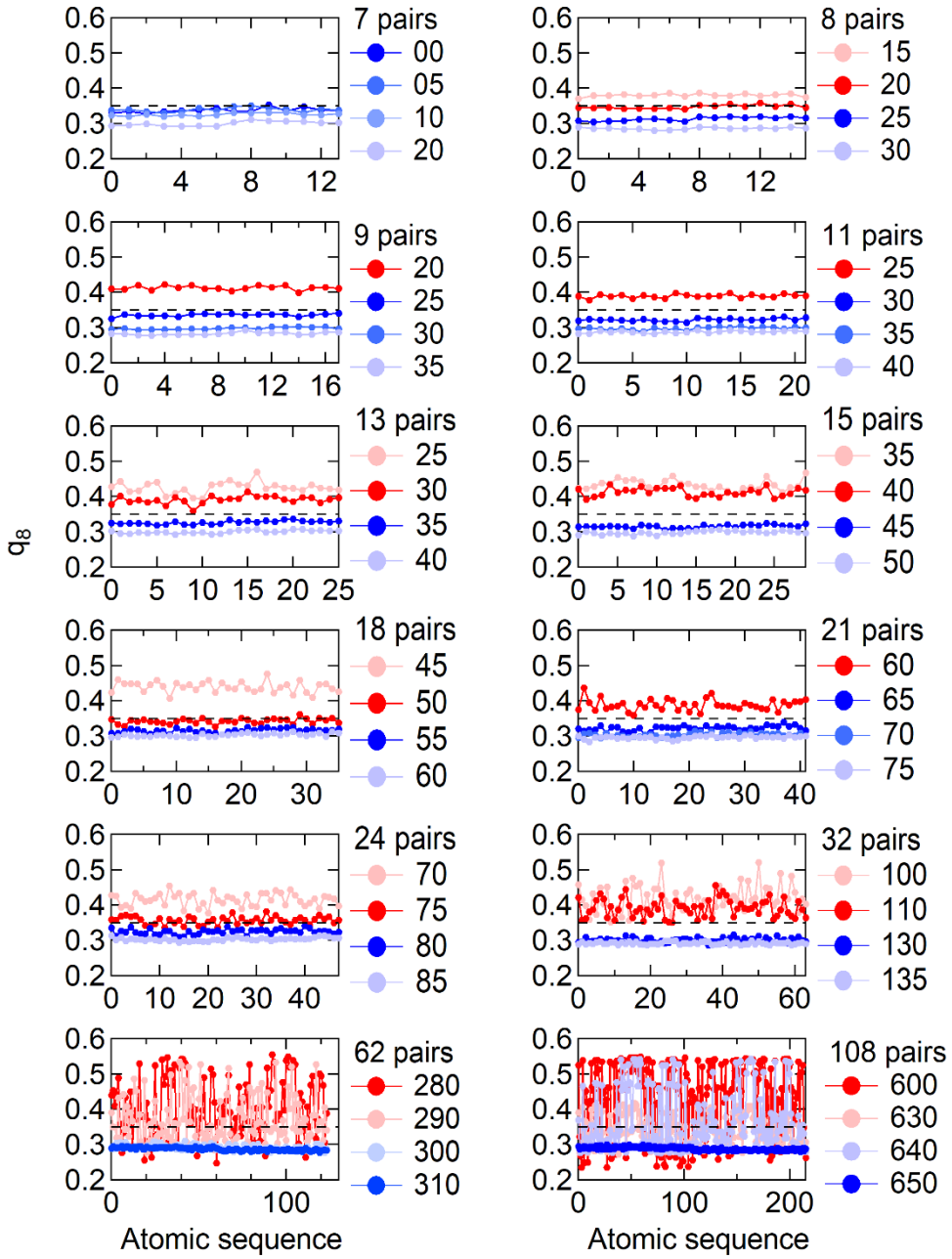

Figure S5. q_8 atomic distributions for ions in NaCl aqueous nanoparticles with different sizes in solid and liquid phase. This figure indicates that q_8 = 0.35 (dash lines) is a good choice for the threshold to distinguish solid-like and liquid-like structures of NaCl nanoparticles.

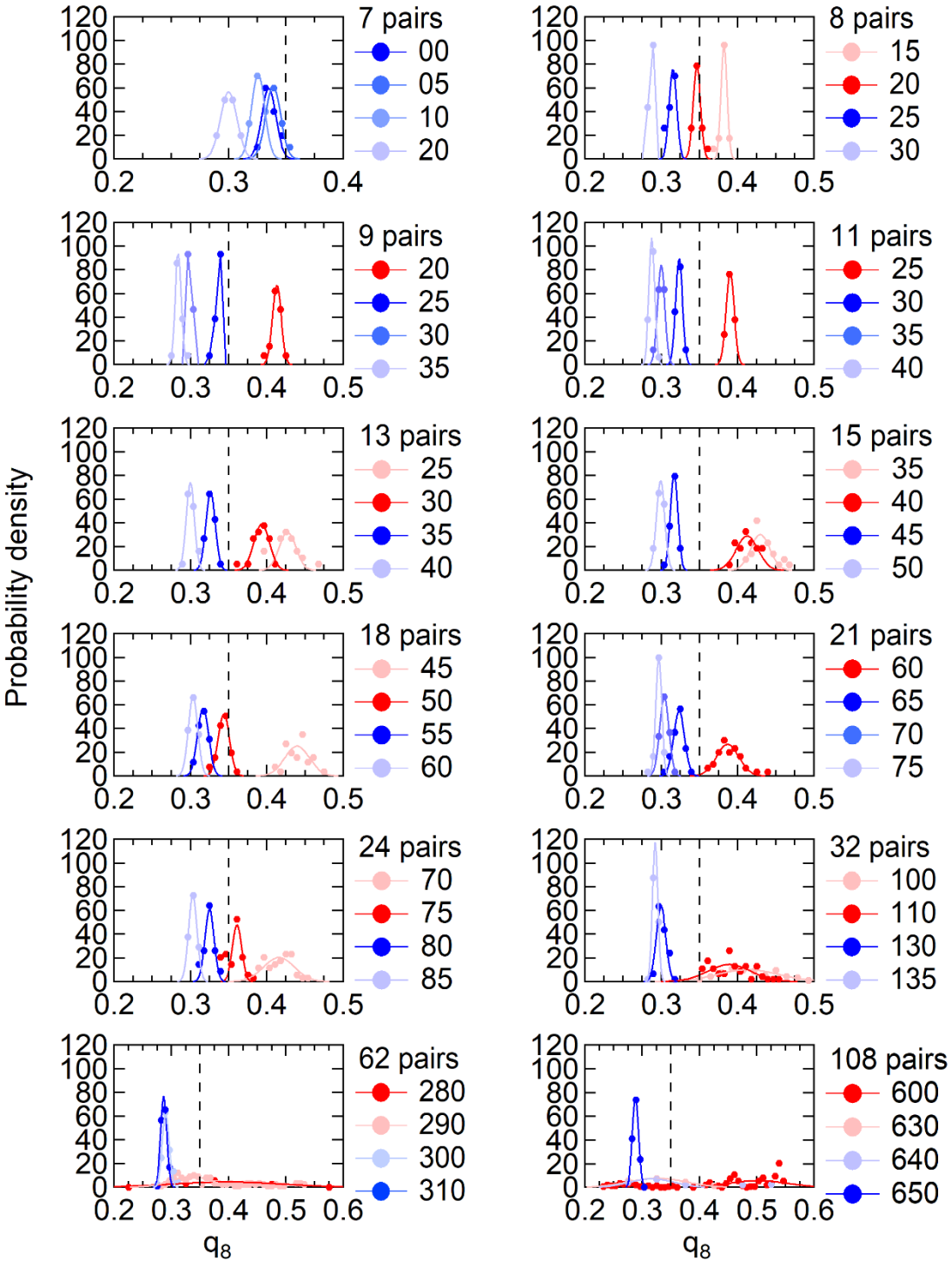

Figure S6. q_8 probability density distributions for ions in NaCl aqueous nanoparticles with different sizes in solid and liquid phase. This figure indicates that q_8 = 0.35 (dash lines) is a good choice for the threshold to distinguish solid-like and liquid-like structures of NaCl nanoparticles.

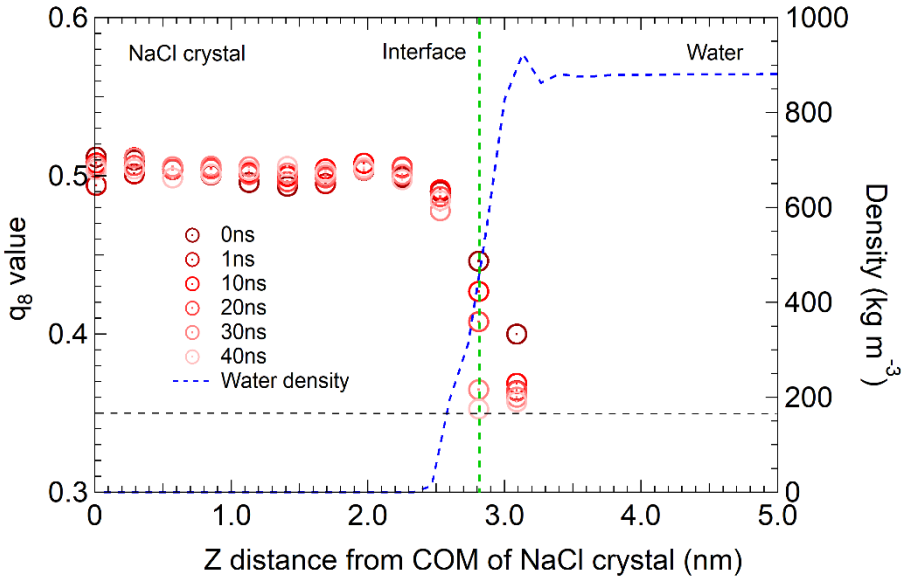

Figure S7. Variation of q_8 distributions with simulation time for different layers of NaCl planar slab interface with water. This figure indicates that q_8 = 0.35 (grey horizontal dash line) is a good choice for the threshold to distinguish solid-like and liquid-like structures in different layers of NaCl planar slab. The dissolution starts from the interface with water where q_8 is decreasing to be less than 0.35 (around 3 nm in Z distance from COM of NaCl crystal). q_8 is larger than 0.35 within the undissolved layers of the NaCl planar slab. The interface (green dash line) is determined based on half of the water density profile.

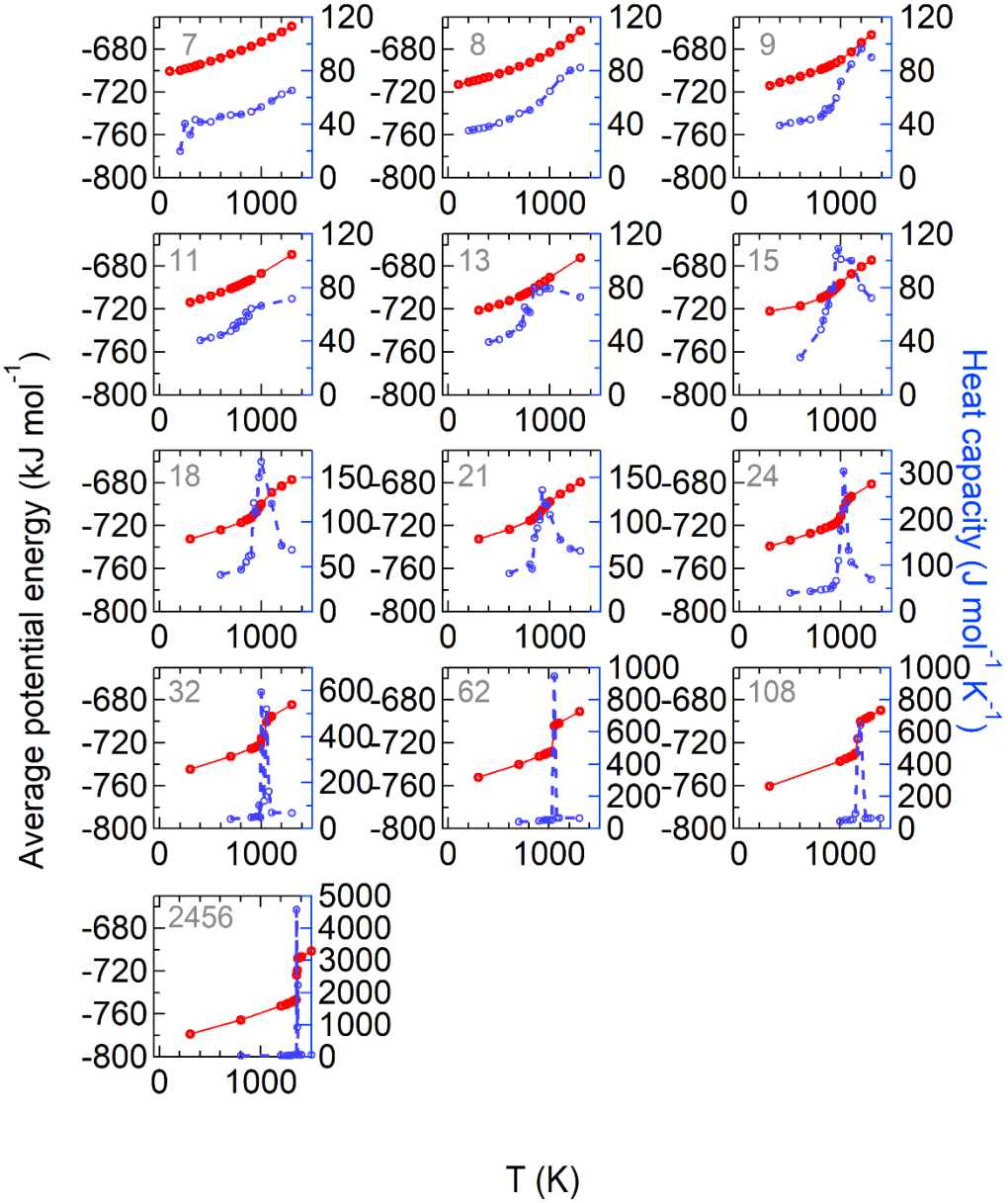

Figure S8. The average potential energy (left axis) and heat capacity (right axis) as a function of temperature T for NaCl crystals with different sizes. The heat capacity (blue circles and dash lines) is evaluated according to Eq. S1 with the average potential energy data (red circles). The melting point is the temperature with the maximum apparent heat capacity. No clear maximum heat capacity is found for 7, 8, 9, 11, 13 pairs of NaCl nanoparticles.

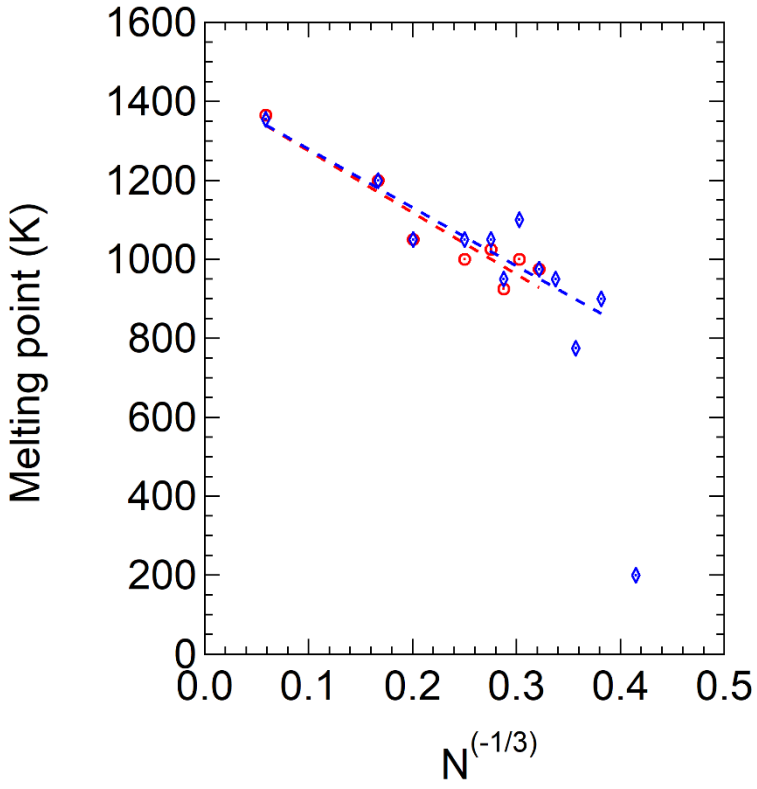

Figure S9. Melting points for NaCl crystals as a function of $N^{(-1/3)}$. The labels above the data are the numbers of the pairs of NaCl ions. N is the number of ions. The red circles are the melting points of NaCl nanocrystals at the maximum heat capacity derived from Eq. S1. The blue diamonds are the melting points of NaCl nanocrystals when q_8 of NaCl nanocrystals is less than 0.35. The red dashed line shows the linear fitting of the melting point respect to $N^{(-1/3)}$ based on the red circles. The blue dashed line shows the linear fitting of the melting point respect to $N^{(-1/3)}$ based on the blue diamonds except for the diamond at 7 pairs of NaCl.

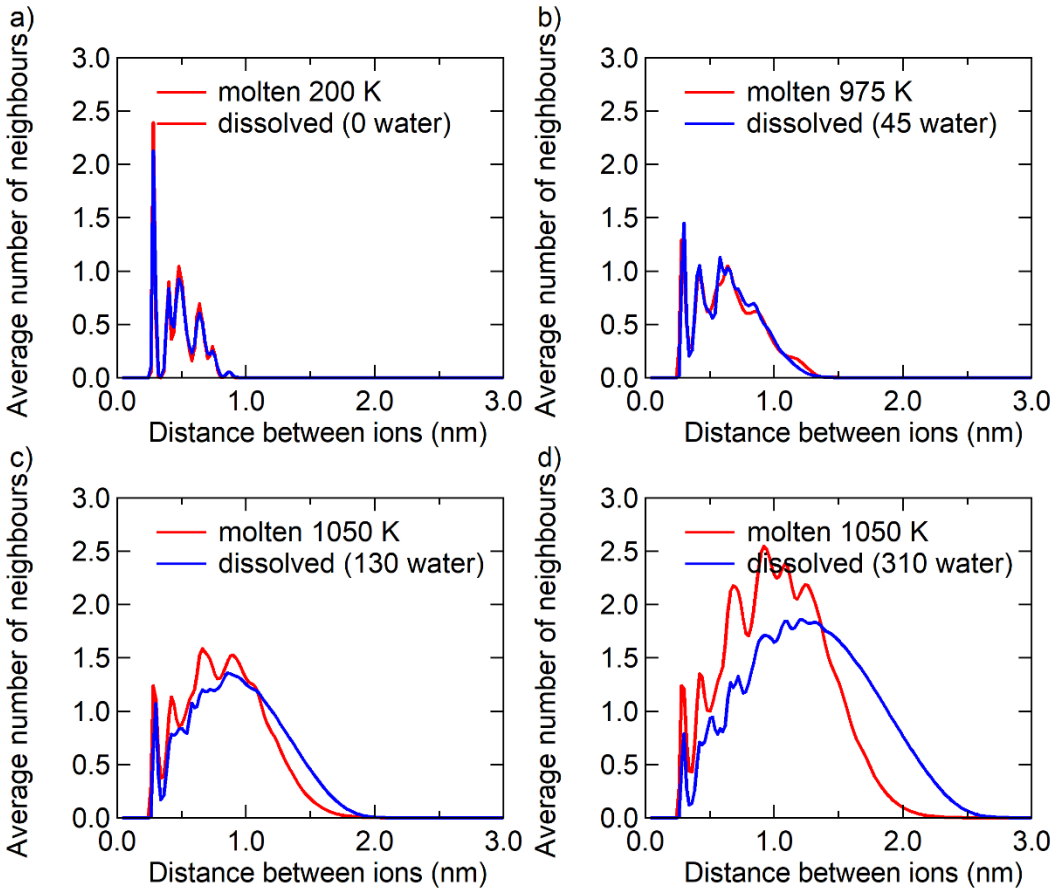

Figure S10. $RDF_{ions\text{-}ions}$ of the molten NaCl and dissolved NaCl in saturated solution nanodroplets. (a) For 7 pairs of NaCl ions particles (diameter = 0.507 nm). (b) For 15 pairs of NaCl ions particles (diameter = 0.709 nm). (c) For 32 pairs of NaCl ions particles (diameter = 1.042 nm). (d) For 62 pairs of NaCl ions particles (diameter = 1.358 nm).

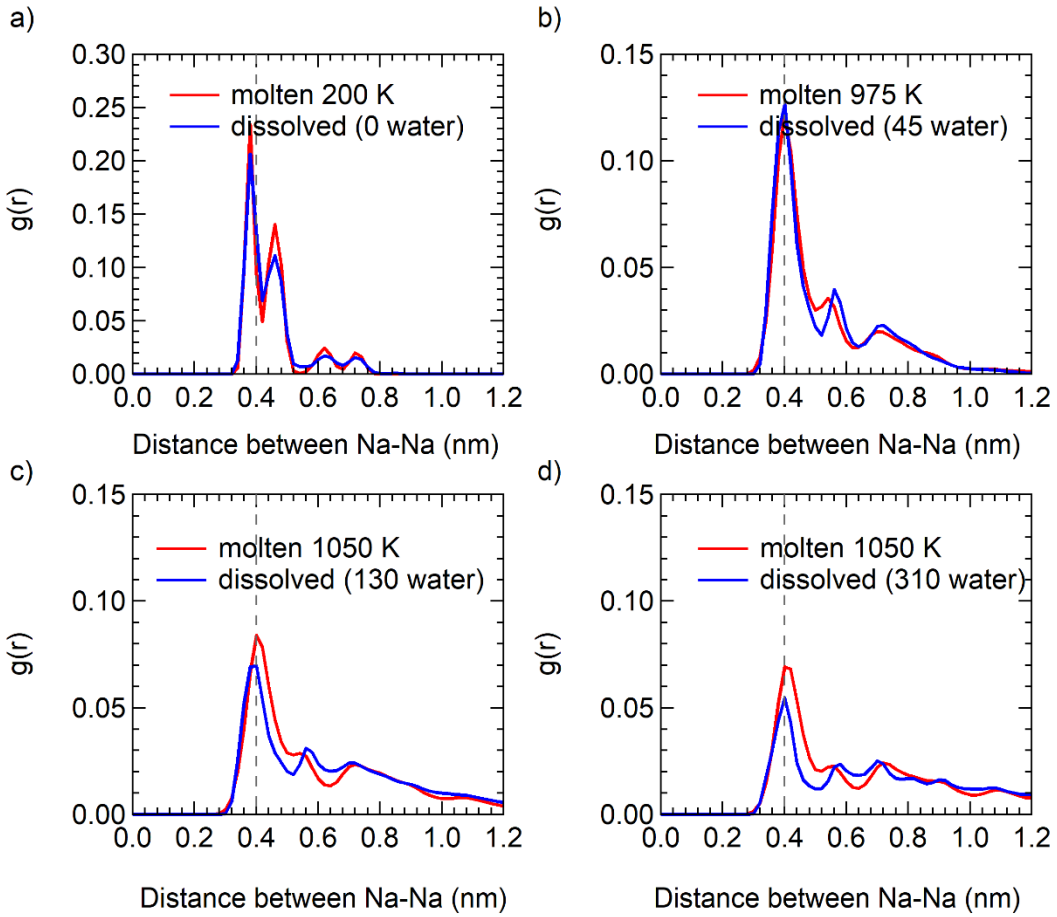

Figure S11. $RDF_{Na\text{-}Na}$ of the molten NaCl and dissolved NaCl in saturated solution nanodroplets. (a) For 7 pairs of NaCl ions particles (diameter = 0.507 nm). (b) For 15 pairs of NaCl ions particles (diameter = 0.709 nm). (c) For 32 pairs of NaCl ions particles (diameter = 1.042 nm). (d) For 62 pairs of NaCl ions particles (diameter = 1.358 nm). The dash line indicates the theoretical position where peak should occur according to the ideal NaCl crystal structure with the distance of ~0.4 nm between Na^+ and Na^+ ions nearest neighbors.

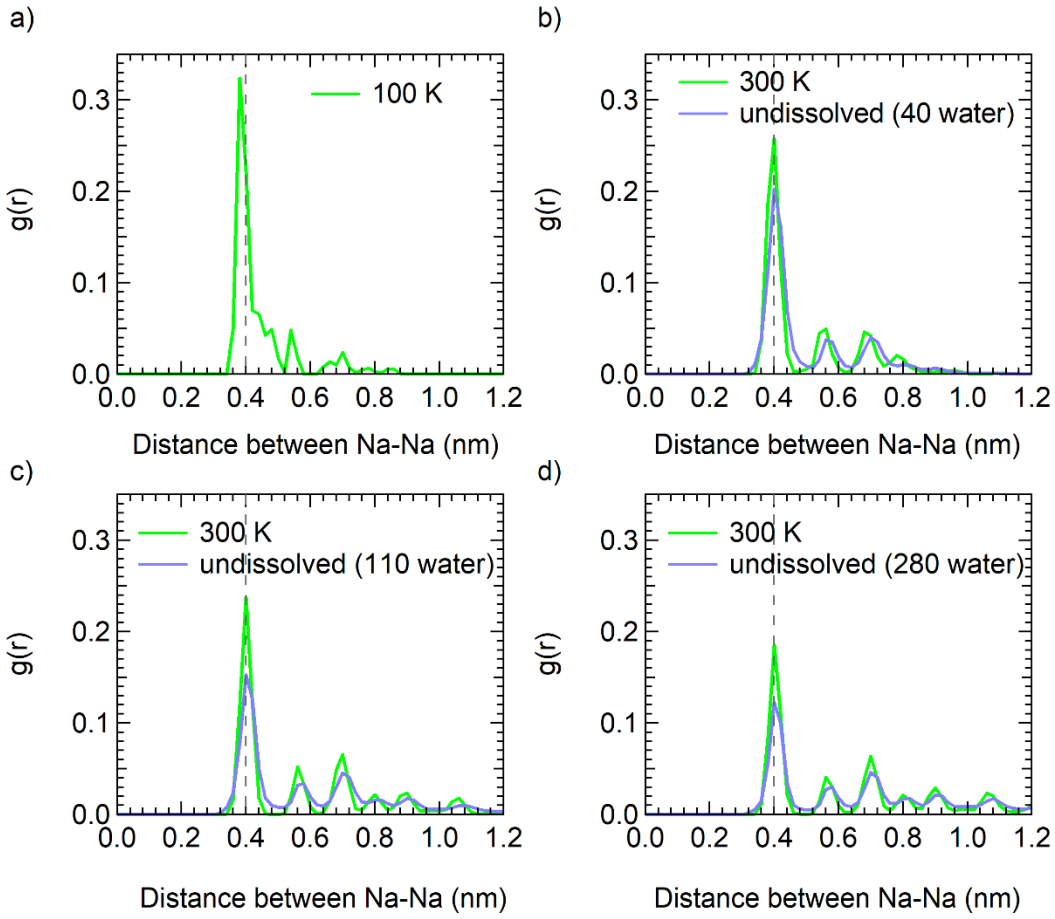

Figure S12. $RDF_{Na\text{-}Na}$ of the unmelted NaCl nanocrystal and undissolved NaCl in nanodroplets. (a) For 7 pairs of NaCl ions particles (diameter = 0.507 nm). (b) For 15 pairs of NaCl ions particles (diameter = 0.709 nm). (c) For 32 pairs of NaCl ions particles (diameter = 1.042 nm). (d) For 62 pairs of NaCl ions particles (diameter = 1.358 nm). The dash line indicates the theoretical position where peak should occur according to the ideal NaCl crystal structure with the distance of ~0.4 nm between Na^+ and Na^+ ions nearest neighbors.

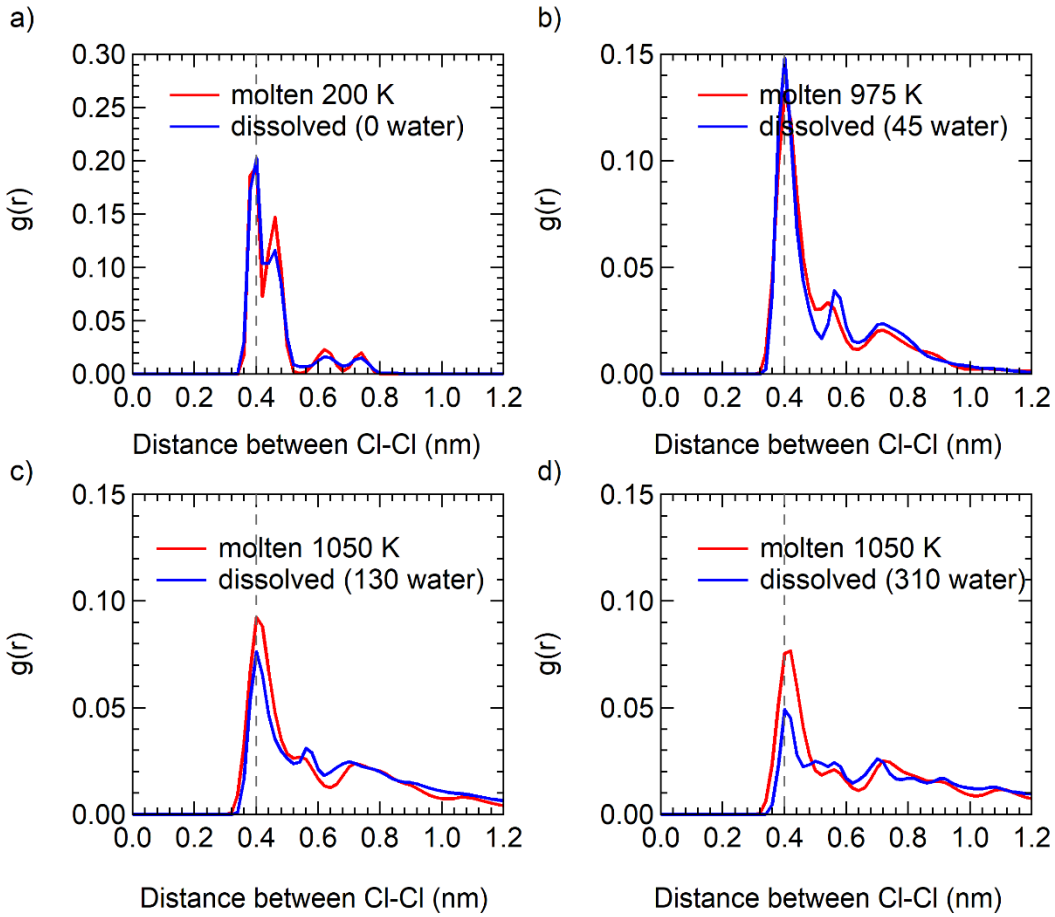

Figure S13. $RDF_{Cl\text{-}Cl}$ of the molten NaCl and dissolved NaCl in saturated solution nanodroplets. (a) For 7 pairs of NaCl ions particles (diameter = 0.507 nm). (b) For 15 pairs of NaCl ions particles (diameter = 0.709 nm). (c) For 32 pairs of NaCl ions particles (diameter = 1.042 nm). (d) For 62 pairs of NaCl ions particles (diameter = 1.358 nm). The dash line indicates the theoretical position where peak should occur according to the ideal NaCl crystal structure with the distance of ~0.4 nm between Cl^- and Cl^- ions nearest neighbors.

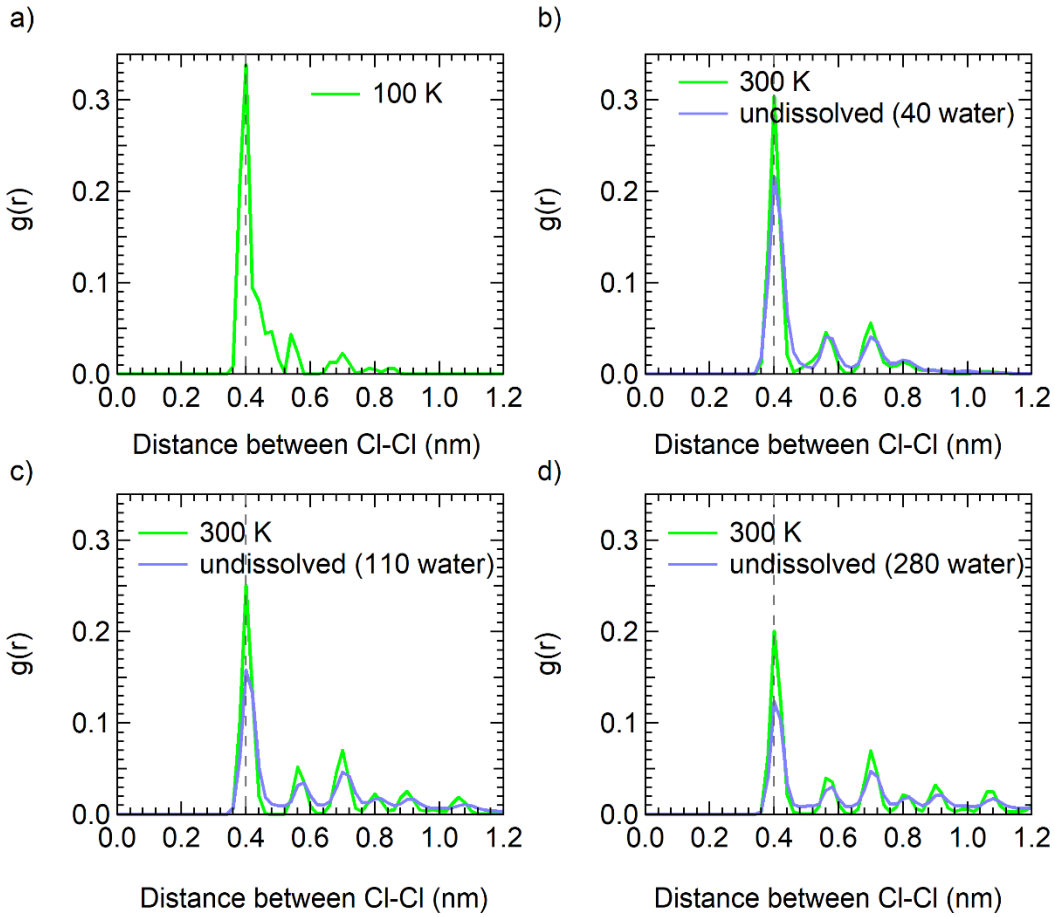

Figure S14. $RDF_{Cl\text{-}Cl}$ of the unmelted NaCl nanocrystal and undissolved NaCl in nanodroplets. (a) For 7 pairs of NaCl ions particles (diameter = 0.507 nm). (b) For 15 pairs of NaCl ions particles (diameter = 0.709 nm). (c) For 32 pairs of NaCl ions particles (diameter = 1.042 nm). (d) For 62 pairs of NaCl ions particles (diameter = 1.358 nm). The dash line indicates the theoretical position where peak should occur according to the ideal NaCl crystal structure with the distance of ~0.4 nm between Cl^- and Cl^- ions nearest neighbors.

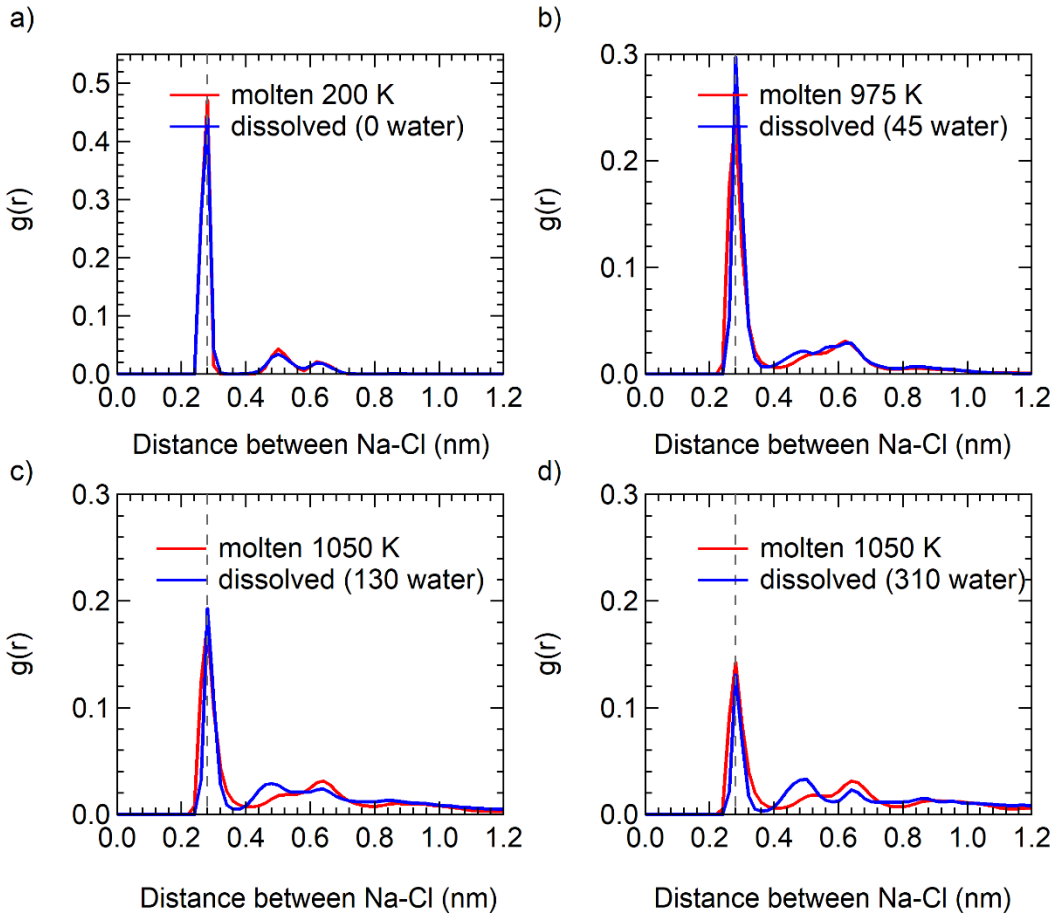

Figure S15. $RDF_{Na\text{-}Cl}$ of the molten NaCl and dissolved NaCl in saturated solution nanodroplets. (a) For 7 pairs of NaCl ions particles (diameter = 0.507 nm). (b) For 15 pairs of NaCl ions particles (diameter = 0.709 nm). (c) For 32 pairs of NaCl ions particles (diameter = 1.042 nm). (d) For 62 pairs of NaCl ions particles (diameter = 1.358 nm). The dash line indicates the theoretical position where peak should occur according to the ideal NaCl crystal structure with the distance of ~0.28 nm between Na^+ and Cl^- ions nearest neighbors.

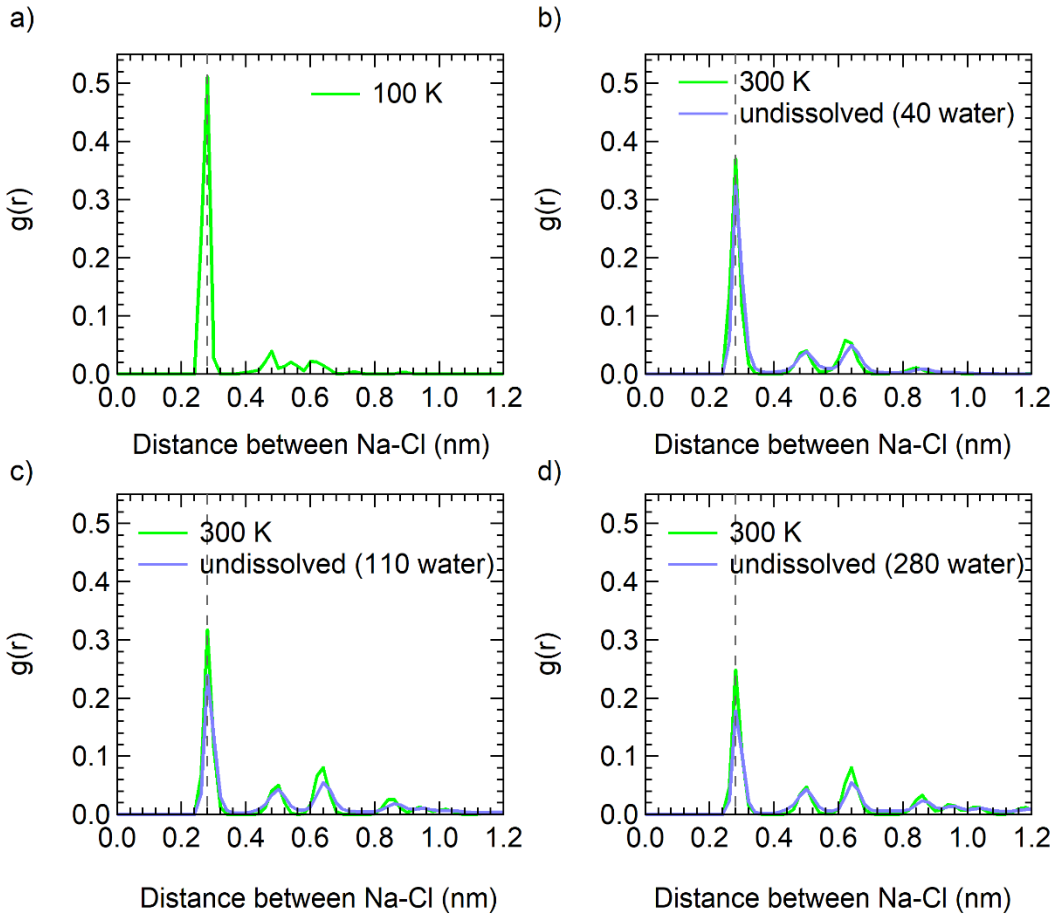

Figure S16. $RDF_{Na\text{-}Cl}$ of the unmelted NaCl nanocrystal and undissolved NaCl in nanodroplets. (a) For 7 pairs of NaCl ions particles (diameter = 0.507 nm). (b) For 15 pairs of NaCl ions particles (diameter = 0.709 nm). (c) For 32 pairs of NaCl ions particles (diameter = 1.042 nm). (d) For 62 pairs of NaCl ions particles (diameter = 1.358 nm). The dash line indicates the theoretical position where peak should occur according to the ideal NaCl crystal structure with the distance of ~0.28 nm between Na^+ and Cl^- ions nearest neighbors.

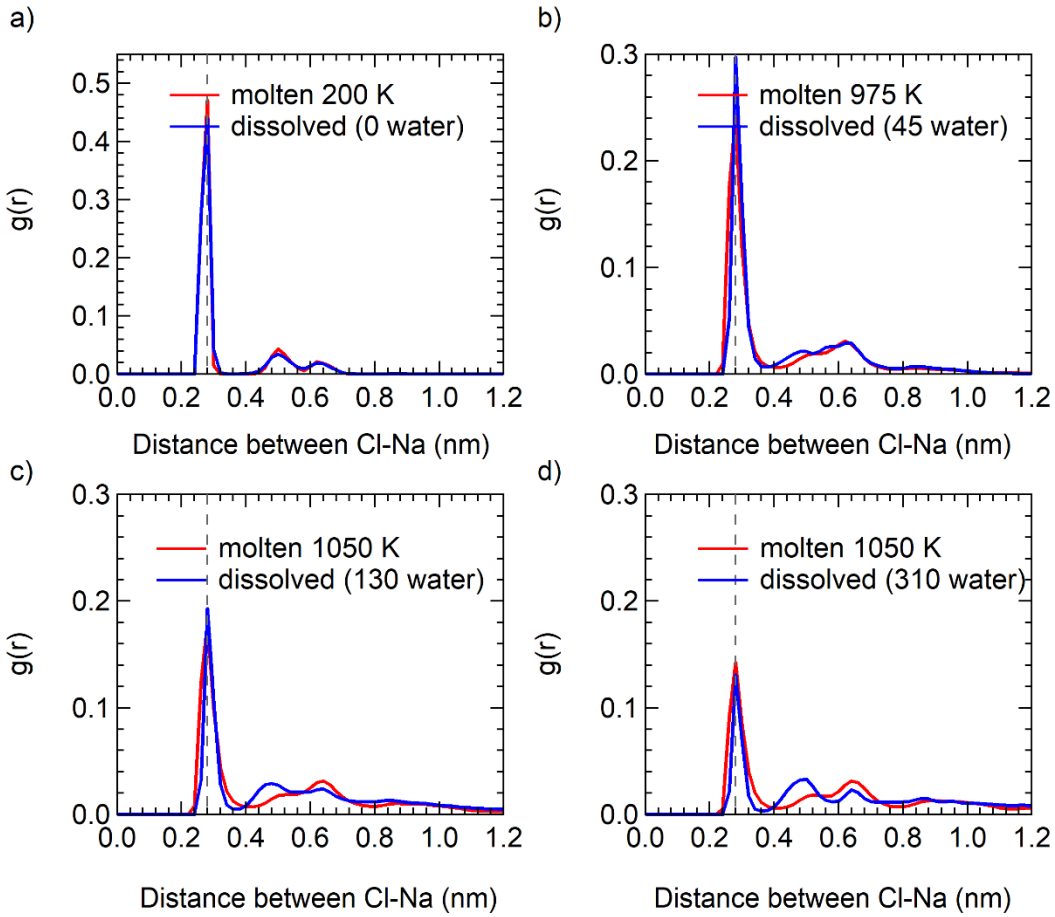

Figure S17. $RDF_{Cl\text{-}Na}$ of the molten NaCl and dissolved NaCl in saturated solution nanodroplets. (a) For 7 pairs of NaCl ions particles (diameter = 0.507 nm). (b) For 15 pairs of NaCl ions particles (diameter = 0.709 nm). (c) For 32 pairs of NaCl ions particles (diameter = 1.042 nm). (d) For 62 pairs of NaCl ions particles (diameter = 1.358 nm). The dash line indicates the theoretical position where peak should occur according to the ideal NaCl crystal structure with the distance of ~0.28 nm between Cl^- and Na^+ ions nearest neighbors.

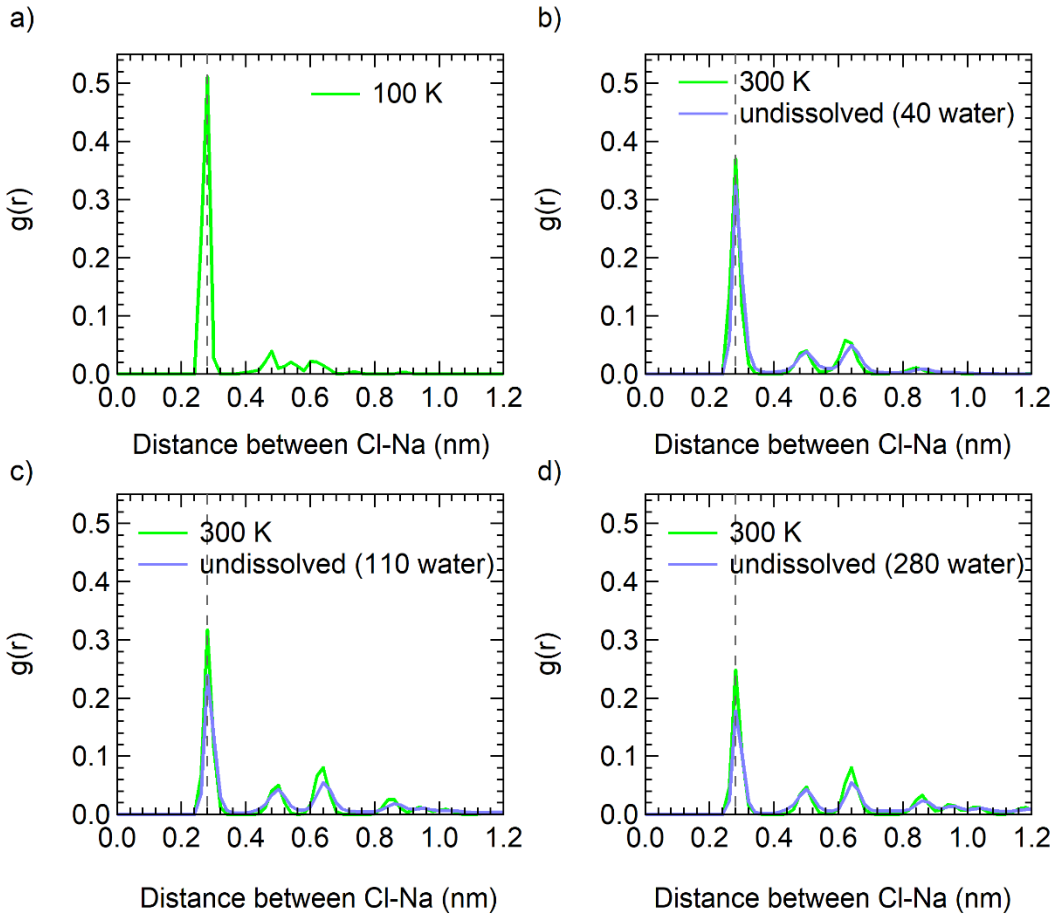

Figure S18. $RDF_{Cl\text{-}Na}$ of the unmelted NaCl nanocrystal and undissolved NaCl in nanodroplets. (a) For 7 pairs of NaCl ions particles (diameter = 0.507 nm). (b) For 15 pairs of NaCl ions particles (diameter = 0.709 nm). (c) For 32 pairs of NaCl ions particles (diameter = 1.042 nm). (d) For 62 pairs of NaCl ions particles (diameter = 1.358 nm). The dash line indicates the theoretical position where peak should occur according to the ideal NaCl crystal structure with the distance of ~0.28 nm between Cl^- and Na^+ ions nearest neighbors.

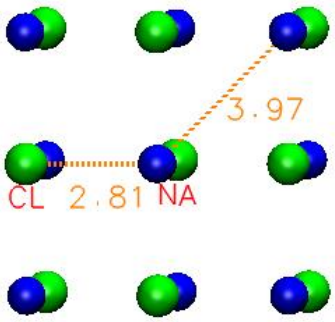

Figure S19. The snapshot of initial 9 pairs of NaCl nanocrystal. The nearest neighbor distance of Na^+ and Cl^- is ~0.281 nm, and the nearest neighbor distance of Na^+ and Na^+ (Cl^- and Cl^-) is ~0.397 nm.

Pair number of NaCl nanoparticle	Initial snapshots	Snapshots at 300 K	Snapshots at melting points determined by heat capacity	Snapshots at melting points determined by q_8	Snapshots at solubility ranges determined by q_8	
7				200 K 	0 water 	
9				900 K 	20 water 	25 water 
11				775 K 	25 water 	30 water 
13				950 K 	30 water 	35 water 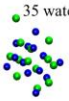
15			975 K 	975 K 	40 water 	45 water 
18			1000 K 	1100 K 	50 water 	55 water 
21			925 K 	950 K 	60 water 	65 water 
24			1025 K 	1050 K 	75 water 	80 water 
32			1000 K 	1050 K 	110 water 	130 water 
62			1050 K 	1050 K 	280 water 	310 water 
108			1200 K 	1200 K 	600 water 	650 water 
bulk	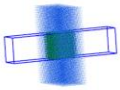		1365 K 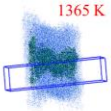	1355 K 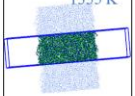		

Figure S20. Snapshots of NaCl nanoparticles during the melting and dissolution processes.

Supplementary Tables

Table S1. Summary of the number of ion pairs, equivalent volume diameter, the maximum number of water not dissolving the entire particle, the minimum number of water dissolving the entire particle, saturated mass fraction range, average potential energy of NaCl in dissolved state, at 300 K, and in melting point, and melting point. [a]Bulk saturated mass fraction is determined from MD simulations in Espinosa et al. (2016). The potential energy of molten NaCl is near -698.39 kJ/mol for all size.

Pair number of NaCl ions in the particle	Diameter (nm)	Maximum number of H_2O not dissolve entire particle	Minimum number of H_2O dissolve entire particle	Saturated mass fraction max (x_s^* max)	Saturated mass fraction min (x_s^* min)	Simulation time for solubility (ns)	Average potential Energy of NaCl in dissolution (kJ mol^{-1})	error	Average potential Energy of NaCl crystal at 300 K (kJ mol-1)	error	Average potential Energy of NaCl in melting point (kJ mol^{-1})	error	Melting Point (K) determined by the heat capacity	Melting Point (K) determined by the q_8 method
7	0.507	-	-	1.000	1.000	600	-697.223	0.000	-697.237	0.420				200
8	0.530	20	25	0.565	0.510	600	-663.653	11.663	-708.286	0.018				
9	0.551	20	25	0.594	0.539	600	-683.027	14.850	-713.802	0.023				900
11	0.594	25	30	0.588	0.543	600	-676.178	11.882	-713.430	0.031				775
13	0.665	30	35	0.585	0.547	600	-676.890	12.270	-721.005	0.030				950
15	0.709	40	45	0.549	0.520	600	-668.226	12.680	-721.740	0.054	-698.007	1.7	975	975
18	0.795	50	55	0.539	0.515	600	-657.628	12.228	-732.450	0.050	-699.750	5.5	1000	1100
21	0.837	60	65	0.532	0.512	600	-657.900	5.762	-732.257	0.026	-705.110	3.3	925	950
24	0.910	75	80	0.510	0.493	600	-644.977	12.635	-739.004	0.032	-703.529	1.2	1025	1050
32	1.042	110	130	0.486	0.444	1000	-624.098	35.152	-744.722	0.028	-716.009	5.6	1000	1050
62	1.358	280	310	0.418	0.394	1000	-566.344	37.290	-752.285	0.068	-704.305	1.3	1050	1050
108	1.745	600	650	0.369	0.350	1000	-521.377	41.787	-760.184	0.045	-700.252	1.9	1200	1200
2456	cubic (4.5 nm^3)	37000	37000	0.178 [a]	0.178 [a]	-	-358.350	20.950	-778.709	0.32	-708.070	3.7	1365	1355

Supplementary Note 1: simulation of melting process

The NaCl nanoparticles with different diameters were simulated at different temperatures with a ΔT (= 50 to 100 K). Following the approach of Qi et al. (2001), the melting point is the temperature with the maximum apparent heat capacity. The heat capacity was evaluated according to the following equation:

$$C_{\mathrm{p}}(T) = \frac{\partial U}{\partial T} + \frac{3}{2} R_{\mathrm{gas}} \tag{S1}$$

where U is the average potential energy and R_{gas} the universal gas constant. The melting process simulation for NaCl nanocrystals with different diameters in this study is summarized in Supplementary Table S1. By fitting the potential energy to a linear function of T in the solid and liquid phase (above and below the transition temperature), the melting point of NaCl crystal can be obtained (Fig. S8). The simulation demonstrates that the melting point of the NaCl nanocrystal is size-dependent, and this phenomenon also occurs in other substances. The nanocrystal with 7 pairs of NaCl ions is in liquid-like (molten) state at 300 K in the simulation.

Supplementary Note 2: a_{w} determination

Water activity (a_{w}) of NaCl is determined by the modified TM model (Tang, 1996; Cheng et al., 2015). It is expressed as a segmentation function of the solute mass fraction (x_{s}):

$$a_{\mathrm{w}} = \begin{cases} 1 + \sum C_{\mathrm{l}} (100 \cdot x_{\mathrm{s}})^{\mathrm{l}} & (x_{\mathrm{s}} \le 0.45) \\ \frac{a_1 \cdot x_{\mathrm{s}}^2 + a_2 \cdot x_{\mathrm{s}} + a_3}{x_{\mathrm{s}}^2 + a_4 \cdot x_{\mathrm{s}} + a_5} & (x_{\mathrm{s}} > 0.45) \end{cases} \tag{S2}$$

where the respective coefficients for NaCl ($x_{\mathrm{s}} \le 0.45$) are C_1 = -6.366×10^{-3}, C_2 = 8.624×10^{-5}, C_3 = -1.158×10^{-5}, and C_4 = 1.518×10^{-7}, and the respective coefficients for NaCl ($x_{\mathrm{s}} > 0.45$) are a_1= 0.1703, a_2= -0.6018, a_3= 0.4315, a_4= -0.4594, a_5= 0.4343.

Supplementary Note 3: Estimation of size-dependent solid-liquid surface tension

The solid-liquid surface tension of the NaCl nanoparticle (σ_{sl}) is determined by the MD solubility data based on the combination of the Ostwald-Freundlich (Ostwald, 1900; Freundlich, 1922) and Gibbs-Duhem equations (Cohen et al., 1987; Richardson and Snyder, 1994; Seinfeld et al., 1998) as

$$\sigma_{\mathrm{sl}} = \frac{RTD}{4\nu} \ln\left(\frac{a_{\mathrm{s}}^*}{a_{\mathrm{s,bulk}}^*}\right) = -\frac{RTD}{4\nu} \int_{x_{\mathrm{s,bulk}}^*}^{x_{\mathrm{s}}^*} M \frac{1 - x_{\mathrm{s}}}{x_{\mathrm{s}}} d\ln a_{\mathrm{w}} \tag{S3}$$

where R is the universal gas constant, T is the temperature, D is the volume equivalent diameter of NaCl crystal at the saturation dissolution point, which equals to the diameter

of the equilibrium droplet of equivalent volume, ν is the molar volume of NaCl solid phase (atomic volume) given as 2.7×10^{-5} m^3 mol^{-1}, and M is the molar weight of solute. $x^*_{s,bulk}$ is the mass fraction of solute in a saturated bulk solution, and $a^*_{s,bulk}$ is the solute activity at $x^*_{s,bulk}$. x^*_s is the mass fraction of solute in a saturated droplet, and a^*_s is the solute activity at x^*_s. a_w is the water activity retrieved from modified TM model (Supplementary Note 2).

The calculated solid-liquid surface tension of NaCl is fitted by the first-order Tolman equation and second-order Tolman equation, respectively (Tolman, 1949a):

$$\sigma_{sl} = \frac{\sigma_{sl,bulk}}{\left(1+\frac{4\delta}{D}\right)} \tag{S4}$$

$$\sigma_{sl} = \frac{\sigma_{sl,bulk}}{\left(1+\frac{4\delta}{D}+8\left(\frac{l}{D}\right)^2\right)} \tag{S5}$$

where $\sigma_{sl,bulk}$ is the bulk solid-liquid surface tension, D is the volume equivalent diameter of NaCl crystal at the saturation dissolution point, which equals to the diameter of the equilibrium droplet of equivalent volume. δ is the Tolman length, and l is a parameter that has the dimension of length.

The calculated σ_{sl} shows a significant size dependence with particle diameter larger than 0.530 nm (8 pairs of NaCl ions) (red and orange bars in Fig. S1). σ_{sl} decreases as the size of NaCl nanocrystals decreases. This size dependence is well explained by the second-order Tolman equation (Eq. S5), corresponding to the derived bulk solid-liquid surface tension ($\sigma_{sl,bulk}$ = (113.16, 142.95] mN m^{-1}) and a negative Tolman length (δ = (-0.082, -0.018] nm) (blue shaded curves in Fig. S1), while the first-order Tolman equation fit with fixed $\sigma_{sl,bulk}$ = 102 mN m^{-1} calculated by MD (Bahadur and Russell, 2008a) (light pink shaded curves in Fig. S1) performs poorly.

According to the blue shaded curves in Fig. S1, σ_{sl} has a critical decrease when the particle diameter is less than ~2 nm. This indicates that the bulk solid-liquid surface tension is applicable, but this may not be the case for the particles less than ~2 nm. Besides, it is still on debate if there is agreement between the interfacial energy at the solid-liquid interface σ_{sl} and at the solute embryo γ_{sl} (Cheng et al., 2015; Erdemir et al., 2009). We estimate $\sigma'_{sl,7}$ = (63.88, 70.57] mN m^{-1} based on the second-order Tolman equation, which is close to the interfacial energy of solute embryo γ_{sl} range from 41 to 63 mN m^{-1} (Zimmermann et al., 2015). This indicates that σ_{sl} and γ_{sl} may

be uniform when the particle is small enough. Note that, since the particle with 7 pairs of NaCl ions is in the molten state at 300 K, the directly calculated $\sigma_{sl,7}$ = 100.82 mN m^{-1}, which is close to the solid-vapor surface tension $\sigma'_{sl,7}$ = 101.85 mN m^{-1} (Patrov, 1997), may not represent the interfacial energy at the solid-liquid interface.

Supplementary Note 4: q_8 validation

We confirm that q_8 is a good indicator for determining whether sodium chloride is solid or liquid. Firstly, we demonstrate that q_8 provides the best separation between liquid and solid phase distributions compared to q_4 and q_6. Based on Eq. 1 and Eq. 2, we choose $l = 4$, 6, and 8 and calculate $q_l(i)$ for each ion in the NaCl solid and liquid particle with 108 pairs of ions, respectively. As shown in Fig. S3 and S4, q_8 atomic and probability distributions of ions can well distinguish NaCl solid and liquid phase. When q_8 <~0.35, ions are supposed to be liquid. Lanaro and Patey's study (2016) yielded a similar result. They chose $l = 2$, 4, 6, 8 and 10 and investigated $q_l(i)$ for the NaCl spherical crystal with ~2000 ions as the solid phase and a supersaturated solution with NaCl mole fraction equal 0.20 as the liquid phase at 300 K. And q_8 was proved to be the best choice for NaCl solid and liquid phase separation, which is similar to the results in this study. Secondly, it is demonstrated that q_8 = 0.35 is a good choice for the threshold to distinguish solid-like and liquid-like structures of NaCl nanoparticles. We investigated $q_l(i)$ for the NaCl solid and liquid nanoparticles with different pairs of NaCl ions, respectively. As shown in Fig. S5 and S6, q_8 atomic and probability distributions of ions is less than 0.35 (grey dash line) in each NaCl liquid nanoparticle. Thus, q_8=0.35 can well separate the solid and liquid phase NaCl nanoparticles. Thirdly, we demonstrate that q_8=0.35 is a good choice for the threshold to distinguish solid-like and liquid-like structures in different layers of a NaCl planar slab. We conduct the study of the NaCl crystal planar slab (4.5 nm^3, 5.6 nm volume equivalent diameter) dissolved in 37000 water molecules for 100 ns in the MD simulation. The q_8 distribution of dissolved ions at the interface tends to be less than 0.35, while the q_8 distribution of undissolved ions inside the crystal remains larger than 0.35 (Fig. S7). This implies that q_8 = 0.35 is still effective for separating solid and liquid phase ions in the dissolution process of the NaCl planar slab system. Overall, q_8 can be examined as a universal standard for separating liquid and solid phase NaCl ions, not only for nanoparticles but also for planar plate systems. ”

3. Energetic analysis of succinic acid in water droplets: insight into the size-dependent solubility of atmospheric nanoparticles

This work is in the ACPD preprint as Chen et al. (2021):

Chen, C., Wang, X., Binder, K., Ghahremanpour, M. M., van der Spoel, D., Pöschl, U., Su, H., and Cheng, Y.: Energetic analysis of succinic acid in water droplets: insight into the size-dependent solubility of atmospheric nanoparticles, Atmos. Chem. Phys. Discuss. [preprint], https://doi.org/10.5194/acp-2020-1329, in review, 2021.

I am the first-author of this work and my contribution to this work includes performing the study, working out the technical details such as preparing succinic acid and water force field files, running molecular dynamics simulations, analyzing the data, making the figures and tables, discussing the results, interpretation and implications, writing the manuscript and submitting the manuscript.

The following text, figures, and tables quoted (within "") from page 62 to page 83 are exactly the same as the manuscript which is cited on page 61.

"**Abstract**

Size-dependent solubility is prevalent in atmospheric nanoparticles, but a molecular level understanding is still insufficient, especially for organic compounds. Here, molecular dynamics simulations are performed to investigate the size dependence of succinic acid solvation on the scale of ~1 to 4 nm with the potential of mean forces method. These analyses reveal that the surface preference of succinic acid is stronger for a droplet than the slab of the same size, and the surface propensity is enhanced due to the curvature effect as the droplet becomes smaller. Energetic analyses show that such surface preference is primarily an enthalpic effect in both systems, while the entropic effect further enhances the surface propensity in droplets. On the other hand, with decreasing droplet size, the solubility of succinic acid in the internal bulk volume may decrease, imposing an opposite effect on the size dependence of solubility as compared with the enhanced surface propensity. Meanwhile, structural analyses, however, show that the surface to internal bulk volume ratio increases drastically, especially when considering the surface in respect to succinic acid, e.g., for droplet with radius of 1 nm, the internal bulk volume would be already close to zero for the succinic acid molecule.

Introduction

Organic compositions in aerosol particles play a vital role in new particle formation and growth, as well as aerosol activation and chemical reactions in the atmosphere (Matsumoto et al., 1997; Zhang et al., 2004; Metzger et al., 2010; Kirkby et al., 2011; Kroll et al., 2011; Riipinen et al., 2012). Organic compositions participate in chemical and physical processes in the internal bulk volume (referred to as the bulk of confined volumes except surface volumes) as well as at the surface area of aerosol particles, and the reactions at the surface are evidenced to be unique compared to the reactions in the internal bulk volume (Finlayson-Pitts, 2009; Donaldson and Valsaraj, 2010; Hayase et al., 2011; Martins- Costa et al., 2012; Monge et al., 2012). However, the influence of organic compositions in the aerosol surface volume, such as the surface partitioning, adsorption probabilities, and phase separation, is still not well understood

experimentally and theoretically (Rudich, 2003; Donaldson and Vaida, 2006; Fuzzi et al., 2006; Rudich et al., 2007; Bluhm and Siegmann, 2009; Werner et al., 2016).

It has been found that particle size plays an important role in regulating the phase transition of atmospheric nanoparticles. Bulk thermodynamics have shown that chemical composition, relative humidity, temperature, and pressure are the main factors controlling aerosol phase state, but they cannot fully explain the observed phenomenon for nanometer-sized particles (Biskos et al., 2006a; Biskos et al., 2006b; Virtanen et al., 2010; Krieger et al., 2012; You et al., 2012; Veghte et al., 2013; Cheng et al., 2015; Werner et al., 2016; Freedman, 2017). Several studies have demonstrated that the phase transitions of nanoparticles have significant size dependence. For instance, Biskos et al. (2006a) found that deliquescence and efflorescence occur at higher relative humidity for sodium chloride nanoparticles using Humidified Tandem Differential Mobility Analyzer (HTDMA) experiments. And Cheng et al. (2015) developed Differential Köhler Analysis to explain the size dependence of deliquescence and efflorescence for the sodium chloride nanoparticles. The morphology of particles was also observed through experiments, where phase separation of aerosol particles is dependent on both particle size and components (You et al., 2012; Veghte et al., 2013; Cheng et al., 2015).

Size dependence of organic molecule solvation in the nanoparticles as one of the phase transitions has been suspected to be prevalent. Favorable surface solvation of organic molecules was known to enhance the solubility of solutes at the surface of the nanodroplet with molecular dynamics (MD) simulation by Hub et al. (2012). Similar results were shown in Sayou et al. (2017) and attractive and repulsive interactions of the organic solute with water molecules were analyzed to explain the surface propensity of organic molecules in the droplet. Besides, Werner et al. (2016) probed the surface activity of succinic acid in sodium chloride and ammonium sulphate solutions by X-ray Photoelectron Spectroscopy (XPS) experiments. The result suggests that succinic acid has a higher solubility at the surface of bulk solutions compared with the total solubility of bulk solutions because of fewer water molecules for hydration at the surface. Furthermore, Werner et al. (2016) developed a partitioned particle model, where the surface region used the surface concentrations estimated from XPS experiments and the internal bulk volume had the bulk-like particle concentration, indicating that the size-dependent solubility of surface-active organic molecules can further enhance cloud activation and chemical reactions in the atmosphere. Despite of the importance of the size dependence of organic molecule solvation, how the solubility in the internal bulk

volume as well as at the surface part of nanodroplets changes, particularly with changing droplet size and the underlying driving mechanism is still unclear.

In this study, size dependence of organic composition solvation in the nanoparticles is investigated based on the molecular dynamics (MD) simulation and energetic analysis. Succinic acid is chosen as a surrogate in the simulation because it is present in the atmospheric aerosol particles (Hyvärinen et al., 2006; Werner et al., 2014). The simulations are performed for one single succinic acid molecule in different sizes of water nanodroplets (i.e., droplet radius from ~1 to 4 nm) and different thickness of water planar slabs (i.e., half slab thickness from ~1 to 4 nm). By comparing the potential of mean forces (PMFs) derived from the simulations, as well as the enthalpic and entropic components decomposed from PMFs, the potential driving forces for the size dependence of succinic acid solvation are identified and the size dependence of succinic acid solubility is discussed.

Methods

PMF calculations

Potential of Mean Forces (PMFs), the free-energy profiles along the chosen coordinate (along the center of mass of water droplets or slabs to the air), were computed using the method of umbrella sampling with a weighted histogram analysis method (Kumar et al., 1995; Souaille and Roux, 2001; Hub et al., 2010). This method is based on the protocol described in Caleman et al. (2011) and Sayou et al. (2017).

The MD simulations were computed with GROMACS 2016.5 (Van Der Spoel et al., 2005; Abraham et al., 2015). The solute (succinic acid molecule) was treated with the Generalized Amber force field (GAFF) with the electrostatic potential (ESP) calculated charges (B3LYP/aug-cc-pVTZ). Although aerosol pH in the atmosphere may vary in a large range (Zheng et al., 2020), the majority of fine particles (diameter <1 μm) is with pH below ~3 to 4 (Fig. 2 of Pye et al. (2020)). In this pH range, the form of succinic acid is more relevant as hydrogen-succinate and succinate dominate only at higher pH. Besides, recent study shows that the surface of pure water droplets and slabs is slightly enriched in hydronium, which might lead to some portion of succinic acid having a different protonation state in the internal bulk volume as on the surface as well (Hub et al., 2014), but the influence is not expected to be large to the aerosol pH. The solvent (water) was described with the TIP4P/2005 force field, as compared to four

other water models the combination of TIP4P/2005 with above force field of succinic acid produce the closest hydration free energy (ΔG_{hyd}) of single succinic acid molecule to the experimental value (Fig. S1 and SI).

Newton's equation of motion was integrated with the leapfrog integration scheme at a time step of 2 fs (Van Gunsteren and Berendsen, 1988). The temperature was controlled at 298.15 K using the stochastic dynamics integrator at a coupling constant of 0.1 ps (Van Gunsteren and Berendsen, 1988). The covalent bonds to hydrogen atoms were fixed by Linear Constraint Solver (LINCS) algorithm (Miyamoto and Kollman, 1992; Hess et al., 1997).

The droplets without periodic boundary conditions were simulated as isolated systems (Fig. 1a). The simulations consisted of a single succinic acid molecule with 140, 1117, 3768, and 8932 water molecules, corresponding to aqueous droplets with approximate radius 1 nm, 2 nm, 3 nm and 4 nm, respectively. The center of mass of the water molecules was fixed at the origin, and no cutoffs were applied to any intermolecular interactions (Fig. 1a).

The umbrella potential was implemented as

$$F(r) = \frac{k(r - r_{\mathrm{c}})^2}{2} \tag{1}$$

where k was set to 1000 kJ mol^{-1} nm^{-2}, r is the radial distance of the solute center of mass from the center of mass of the water molecules. Along with the reaction coordinate r, 20 windows with r_{c} of 0, 0.2, …, 4 nm, 25 windows with r_{c} of 0, 0.2, …, 5 nm, 35 windows with r_{c} of 0, 0.2, …, 7 nm, and 35 windows with r_{c} of 0, 0.2, …, 7 nm were prepared for the droplet systems (i.e., droplet radius from ~1 to 4 nm). Since the simulations were performed at the room temperature, to prevent individual water molecules from frequent evaporation from the droplet surface that may lead to an ill-defined droplet center of mass, a spherical flat-bottom restraining potential was applied to each water molecule. The potential was given by

$$V_{\mathrm{fb}}(r) = \frac{1}{2} k_{\mathrm{fb}} (r - r_{\mathrm{fb}})^2 H(r - r_{\mathrm{fb}}) \tag{2}$$

where r is the radial distance of the oxygen atom of the water molecule from the center of mass of the water droplet, r_{fb} is the radius of the sphere around the center of mass without any additional force, which was taken to be 0.5 nm larger than the radius of the water droplet. The force constant k_{fb} was set to 1000 kJ mol^{-1} nm^{-2}, and H is the

Heaviside step function. The energy of each structure was minimized, and the umbrella sampling was then conducted for 51 ns for each window of the solute location.

After removing the first 1 ns of each trajectory for equilibration, the PMFs for droplet systems were computed by the integration of the mean force. An analytical entropy correction for the PMFs of the droplet systems (Neumann, 1980) was computed as

$$\Delta S(r) = 2k_{\mathrm{B}} \ln(r) \tag{3}$$

where k_{B} is the Boltzmann factor, r is the radial distance of the solute center of mass from the center of mass of the water molecules. This correction is due to the fact that for the case when the succinic acid molecule is at a distance r, it can be anywhere in the volume of a spherical shell of size $4\pi r^2 \Delta r$ (where Δr = 0.2 is the thickness of the shell) and hence the associated entropy, which scales as the logarithm of the volume of this shell times Boltzmann's constant, yields a term as written in Eq. (3).

The slab systems were simulated under the periodic boundary condition in *x*, *y*, *z* directions with the canonical (NVT) ensemble. The single succinic acid molecule was solvated in the center of rectangular water box with edge lengths of 3 nm to the *x* and *y* directions and of 2, 4, 6 and 8 nm to the *z* direction. The slab systems (Fig. 1b) consisted of 560, 1200, 1800, and 2400 water molecules, which correspond to 1, 2, 3, and 4 nm of half slab thickness, respectively. The systems were then elongated to 30 nm in the *z* direction to create liquid-vapor interfaces. The smooth particle-mesh Ewald (PME) method with a real-space cutoff of 1.35 nm, a spline order of 6, and relative tolerance of 10^{-5} was used to the Coulombic interactions. The PME with a real-space cutoff of 1.35 nm was also used for the van der Waals interactions. The umbrella potential was implemented as

$$F(z) = \frac{k(z - z_{\mathrm{c}})^2}{2} \tag{4}$$

where k was set to 1000 kJ mol^{-1} nm^{-2}, z is the distance along the z direction of the solute center of mass from the center of mass of the water molecules. Along with the reaction coordinate z, 20 windows with z_{c} of 0, 0.2, …, 4 nm, 25 windows with z_{c} of 0, 0.2, …, 5 nm, 35 windows with z_{c} of 0, 0.2, …, 7 nm, 35 windows with z_{c} of 0, 0.2, …, 7 nm were prepared for the slab systems (i.e., half slab thickness from ~1 to 4 nm). The center of mass of the water molecules was fixed at the center of the rectangular cell, and restraint was used to prevent possible water evaporation. The restraint was given by

$$V_{\mathrm{fb}}(z) = \frac{1}{2} k_{\mathrm{fb}} (z - z_{\mathrm{fb}})^2 H(z - z_{\mathrm{fb}}) \quad (5)$$

where z is the distance along the z direction of the oxygen atom of the water molecule from the cell center. z_{fb} was taken to be 0.5 nm larger than the half of thickness of the slab in the z direction. The force constant k_{fb} was set to 1000 kJ mol^{-1} nm^{-2}.

Figure 1c depicts the schematic free energy profiles of a succinic acid along the radius in the droplet system and along the z-axis in the slab system. As the molecule moves from the center of mass of water toward the gas phase, its free energy goes through a minimum at the water-vapor interface, then increases again, and finally reaches a plateau in the gas phase. The free energy difference of the transition of the solute from the gas to the internal bulk volume of liquid, ΔG_{ba}, represents the free energy of hydration of succinic acid (Sayou et al., 2017). ΔG_{sb} is the free energy of the transition from the internal bulk volume to the liquid-vapor interface, and ΔG_{sa} is the free energy of the transition from the gas phase into the liquid-vapor interface.

To separate the energetic contributions that govern surface propensity, the PMFs of droplet systems and slab systems were further decomposed into enthalpic and entropic components. Under the canonical (NVT) ensemble, the enthalpic part ΔH was computed as the average potential energy of the system in each simulation. The entropic component was computed as

$$-T\Delta S = \Delta G - \Delta H \quad (6)$$

ΔH was further decomposed into water-water and solvent-water interactions in each system.

Structural analysis

For structural analysis, the water density profiles were calculated along the radius for the droplet systems and along the z-direction for the slab systems. For droplet, the simulation cell was divided into multiple shells with a thickness of 0.02 nm, and the density of each shell was statistically calculated based on the cumulative radial distribution functions of water molecules. For slab, the simulation cell was divided into multiple slices with a thickness of 0.02 nm, and the density of each slice was statistically averaged over the simulation time. Both water density profiles from droplets and slabs were further fitted to a hyperbolic tangent function (Vega and de Miguel, 2007) as

$$\rho(s) = \frac{1}{2}(\rho_{\mathrm{L}} + \rho_{\mathrm{V}}) - \frac{1}{2}(\rho_{\mathrm{L}} - \rho_{\mathrm{V}}) \tanh\left[\frac{s - s_0}{t}\right] \quad (7)$$

where ρ_{L} and ρ_{V} are densities of water and vapor, s_0 is the position of the Gibbs-dividing surface, and t is a parameter about surface thickness.

Results and discussion

Size dependence of surface propensity

In Fig. 2, the calculated potential of mean forces (PMFs) profiles show a significant surface propensity of succinic acid in the liquid phase with a minimum at the surface region for both water droplet and slab systems at all sizes. It indicates that the succinic acid is more preferably located at the surface region than inside the internal bulk volume and the gas phase.

The differences of free energy between succinic acid in the internal bulk volume, surface and air were further calculated to identify the size dependence of surface propensity of succinic acid. As shown in Fig. 3a, ΔG_{sb}, the free energy difference of the transition of succinic acid from the internal bulk volume to the surface, is negative in every droplet and slab system, reflecting the surface active of succinic acid. ΔG_{sb} in the droplet system is smaller than that in the slab system of the same size, suggesting that the surface propensity in the droplet system is more enhanced than that in the slab system due to the curvature effect. Similar results were observed in Sayou et al. (2017), where for ethane, benzene, methanol, and H_2S, curvature dependence is appreciable and the magnitude is mainly related to the structure of organic molecules. Hub et al. (2012) also supported this view in their study. Besides, based on XPS experiments, Werner et al. (2016) found the enrichment of surface partitioning of succinic acid at the surface region of the bulk solutions.

Meanwhile, ΔG_{sa}, the free energy difference of the transition of succinic acid from gas to the water surface, which is negative as well, is larger in the droplet system than that in the slab system of the same size (Fig. 3b), showing that the propensity of succinic acid at the surface layer (relative to the gas phase) in the droplet system is less than that in the slab system. Furthermore, the magnitude of the propensity is affected by the nature of the organic molecules as well as the temperature (Sayou et al., 2017). As a result, the decrease of ΔG_{sb} and increase of ΔG_{sa} from slab to droplet with the uniform size indicates that succinic acid is "pushed" from the internal bulk volume to the surface region more strongly but "pushed" from the air to the surface region more slightly for the droplet systems. These two opposite forces further affect succinic acid

to prefer to be exposed more to the air in the droplet rather than in the slab, which further demonstrates that the droplet curvature enhances the surface propensity of succinic acid.

When comparing the slab systems of different thicknesses, both ΔG_{sb} (Fig. 3a, blue circles) and ΔG_{sa} (Fig. 3b, blue triangles) are almost constant with the increase of the thickness, suggesting a near constant surface propensity. In other words, the change of slab thickness only has a very slight effect on the surface propensity of succinic acid. This is different from the results of nanodroplet with a curvature/Kelvin effect. Without a curvature, the pressure inside the slab does not depend on the slab thickness leading to almost unchanged surface propensity. And at the considered temperature, this pressure to very good approximation is zero. However, for the droplet systems, when the radius of the droplet increases but the curvature of the droplet decreases at the same time, ΔG_{sb} decreases first from radius 1 to 3 nm but then increases (Fig. 3a, orange circles), showing that the surface propensity relative to the internal bulk volume is enhanced first and then weaken. ΔG_{sa} shows a similar trend (Fig. 3b, orange triangles), meaning that the surface propensity relative to the air is also enhanced first and then weakened. Overall, the surface propensity is weakened as the droplet becomes larger and the difference between the droplet and slab systems becomes smaller when the droplet size increases. This result shows that different from thin slabs: for a nano-sized droplet, due to the Kelvin equation, the pressure inside the droplet is enhanced when the droplet size decreases.

Energetic analysis

To separate the energetic contributions that govern surface propensity of succinic acid, the PMF is decomposed into the enthalpic and entropic components for both droplet systems (radius from ~1 to 3 nm) and slab systems (half thickness from ~1 to 3 nm) (Fig. 4). Energetic decomposition for larger droplets and slabs is excluded due to the large uncertainties in the enthalpic component. Enthalpic curves are further divided into succinic acid-water interactions and water-water interactions (Fig. 5). For both droplet and slab systems, enthalpies show a significant minimum at the surface, demonstrating that the surface preference of succinic acid in both systems is primarily an enthalpic effect. However, the enthalpic minimum at the surface is partially

compensated by the entropy, indicating that the entropy affects the magnitude of surface preference of succinic acid.

On the contrary, the enthalpies show an increase in both droplets and slabs when being ~0.5 nm away from the surface, which may be caused by a reduced number of water-water interactions (Fig. 5, lines with open triangles). However, this increase of enthalpy is offset partially by the decreased entropy due to the increased rotational freedom of water molecules (Hub et al., 2012), resulting in a slight jump in the internal PMFs close to the surface. Furthermore, this jump becomes more significant when the size of the droplet decreases, showing that enthalpy plays a more important role in that region when the droplet size decreases. In addition, enthalpy plays a leading role in the performance of the succinic acid molecule in the internal bulk volume of droplets as well as in the internal bulk volume of slabs. However, the internal enthalpy and entropy inside droplets fluctuate more intensely than those in the slab systems due to the more active molecule interactions (Fig. 5).

Discussion on size dependence of solubility

With XPS detected surface enrichment, Werner et al. (2016) predicted a higher solubility of succinic acid in the small nanodroplet, based on the speculative assumptions that (1) with decreasing droplet size, the thickness of surface is assumed to be constant of ~0.4 nm, a value determined as the full width at half maximum of carbon profile peak with MD simulation in a slab system (3.9×3.9×3.9 nm^3 succinic acid aqueous solution in a 3.9×3.9×13 nm^3 slab, simulated for 1 ns at 278.15 K) (Werner et al., 2014); (2) the surface region of the nanodroplet was supposed to have the same enhanced surface concentration of succinic acid in the bulk solutions; and (3) the internal bulk volume of the nanodroplet was recognized to have the same solubility of succinic acid as that in the internal bulk volume of bulk solutions. With the results from this study, these assumptions may be revisited and gained more insight into the size dependence of solvation of succinic acid in nanodroplets compared to slab systems.

The free energy of hydration (ΔG_{ba}) gives implications on the size dependence of solubility of succinic acid (Fig. 3c). As shown in Fig. S1, the free energy of hydration of succinic acid in bulk solutions ΔG_{hyd} is -44.94 ± 1.4 kJ mol^{-1} by TI method calculation based on the GAFF/ESP force field for succinic acid and the TIP4P/2005 force field for water molecules (SI). For slab systems, ΔG_{ba} increases very slightly

along with the increase of the slab thickness but not beyond the range of ΔG_{hyd} (Fig. 3c, pink block). It means that the potential of succinic acid hydration into the slab systems is basically unchanged no matter how the slab thickness changes. This further indicates that the solubility of succinic acid in the internal bulk volume as well as at the surface region of the slab systems is almost constant.

Interestingly, for droplet systems, the hydration free energy ΔG_{ba}, under the interactions of ΔG_{sb} and ΔG_{sa} by the curvature effect, are significantly larger than ΔG_{hyd} at all sizes. The unfavorable succinic acid solvation in the internal bulk volume of the nanodroplets decreases the solubility of succinic acid in the internal bulk volume of the nanodroplet compared to the solubility in the internal bulk volume of the slabs. Furthermore, the hydration free energy is larger in the internal bulk volume of small droplets than that in large ones, suggesting a decrease of succinic acid solubility in the internal bulk volume of nanodroplet when the droplet size becomes smaller.

Although a larger hydration free energy usually suggests a smaller solubility in water, i.e., a decrease of succinic acid solubility in the internal bulk volume of nanodroplet when the droplet size becomes smaller, the favorable surface solvation of succinic acid enhances the surface solubility of succinic acid in the nanodroplets. Therefore, the overall size dependence of succinic acid solubility with decreasing sizes of the nanodroplets is controlled by the competition between these two effects (i.e., decreased solubility in the internal bulk volume and increased surface enrichment) as well as the drastic change of surface to internal bulk volume ratio.

To examine how the surface thickness and surface to internal bulk volume would change when the size of the systems decreases, the water density profiles (Fig. 2, dash lines) were fitted by the hyperbolic tangent function (Vega and de Miguel, 2007; Wang et al., 2019) based on the distributions of water density from MD simulations (Fig. 2, open circles). The surface thicknesses of different sizes of nanodroplets and slabs can then be obtained (Fig. 6a). It should be noted that the surface thickness of the slab profiles systematically depends on the lateral linear dimension of the slab, which is 3 nm here. Due to the capillary wave broadening it diverges logarithmically with this linear dimension, while in contrast, no such ambiguity occurs for the surface thickness of droplets (Wang et al., 2019). The structural analyses show that the surface to internal bulk volume ratio in water droplet increases significantly with decreasing droplet size (Fig. 6c), although the surface thickness of water decreases at the same time. When

droplet radius changes from 4 to 1 nm The water surface thickness slightly decreases from ~0.34 to ~0.25 nm (Fig. 6a). This result is consistent with the previous researches involving nanodroplets and slab water (Thompson et al., 1984; Ismail et al., 2006; Vega and de Miguel, 2007; Wang et al., 2019).

However, how to define the surface is another important issue here. Regarding succinic acid molecule, thermodynamic analysis shows that when the droplet is smaller, enthalpy and entropy ranges in the internal bulk volume become narrower. As shown in Fig. 5, for droplets of all sizes, the interaction of succinic acid molecule and water molecules shows a significant increase in both droplets and slabs when being ~1 nm away from the surface, indicating the surface thickness is effectively ~1 nm in respect to succinic acid molecule and is independent to the change of droplet size. Moreover, relatively stable interactions exist in the internal bulk volume of droplets with radius of 2 nm (Fig. 5b) and 3 nm (Fig. 5c), but not in the droplet with radius of 1 nm (Fig 5a). In this regard, for droplet with radius of 1 nm, the internal bulk volume is close to zero for succinic acid molecule, but in terms of water molecule, the radius of internal bulk volume is still ~0.75 nm (Fig. 6b). Thus, in respect to succinic acid molecule, the surface to internal bulk volume ratio would increase much stronger than that for water molecule. These results suggest that the width of the PMF profiles is not simply controlled by the width of the interface, what also matter is the effective range of intermolecular forces between the succinic acid molecule and the water molecules. Since these forces contain long-range contributions, it is understandable that a saturation of the PMF profiles in the center of the droplet or slab in Fig. 2 (at the same horizontal plateau) is not observed, unlike the behavior of the density profiles.

Conclusion

In conclusion, the size dependence of succinic acid solvation was probed based on the MD simulations and energetic analysis. The simulations were conducted for a single succinic acid molecule in the different sizes of water nanodroplets (i.e., droplet radius from ~1 to 4 nm) and different thickness of water planar slabs (i.e., half slab thickness from ~1 to 4 nm). On the one hand, energetic analyses reveal a stronger surface preference for a droplet than the slab of the same size, and the surface propensity is enhanced due to the curvature effect as the droplet becomes smaller. The energetic driving force underlying such surface preference is primarily an enthalpic effect in both systems, while the entropic effect further enhances the surface propensity in droplets.

On the other hand, the energetic analyses give implications on the size dependence of solubility of succinic acid in nanodroplets. The solubility of succinic acid in the internal bulk volume may decrease when the droplet becomes smaller, imposing an opposite effect on the size dependence of solubility as compared with the enhanced surface propensity. Meanwhile, the overall size dependence of succinic acid solubility is also controlled by the drastic change of surface to internal bulk volume ratio. However, structural analyses show that the surface to internal bulk volume ratio increases drastically, especially when considering the surface in respect to succinic acid, e.g., for droplet with radius of 1 nm, the internal bulk volume would be already close to zero for the succinic acid molecule.

Figures

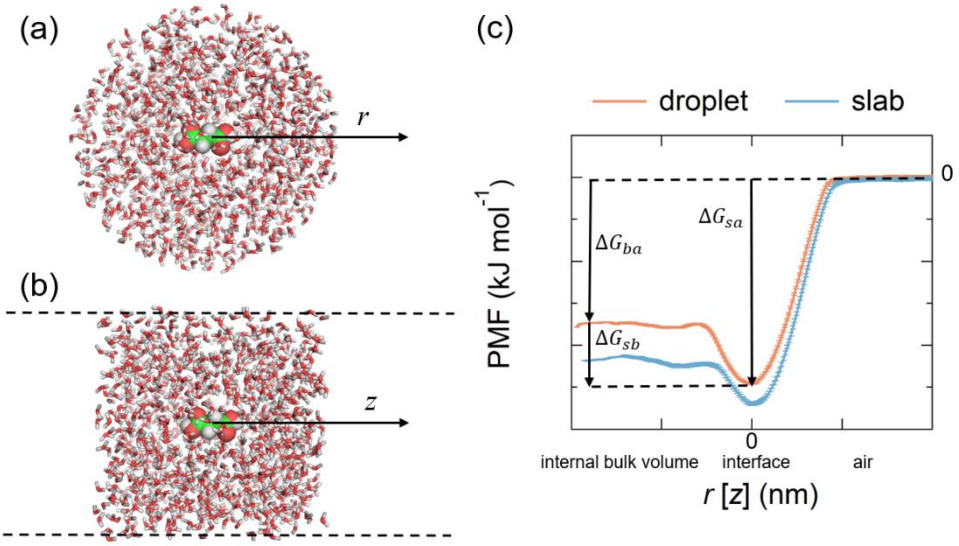

Figure 1: Model configuration and PMF calculations for water droplet and slab. Snapshot of the molecular configuration from the computation of the free energy profile of a succinic acid molecule coordinate across a liquid water droplet (a) and a liquid water slab (b). The succinic acid molecule is at the center of mass of the water droplet. (c) Typical PMF profiles of a succinic acid molecule in droplet and slab systems. The coordinate $r[z]$ is expressed in terms of the radical distance [distance along the z direction]. $r[z] = 0$ is where the PMF is minimum at the interface. ΔG_{ba}, ΔG_{sb}, and ΔG_{sa} are the free energy differences of the transition of the solute from the gas to the internal bulk volume of liquid, the internal bulk volume to the liquid-vapor interface, and the gas phase into the liquid-vapor interface, respectively.

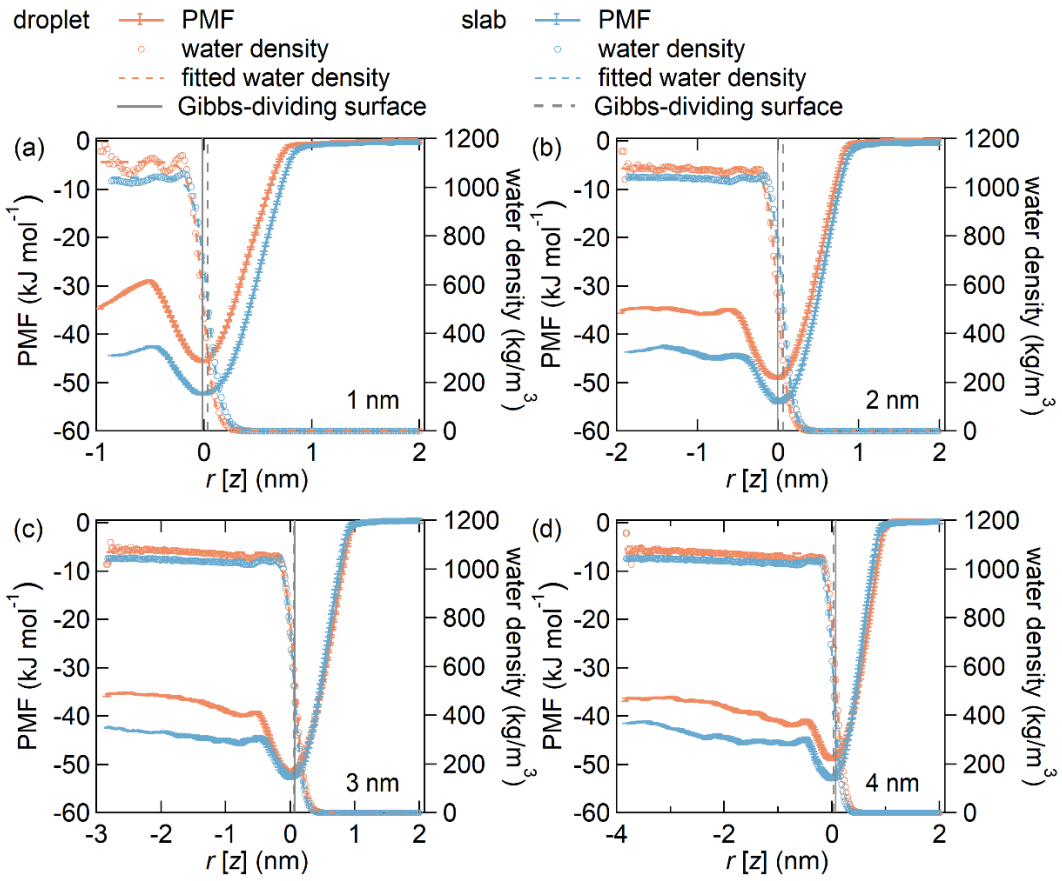

Figure 2: The potential of mean forces (PMFs) for succinic acid and density profiles of water in different sizes of droplet and slab systems at 298.15 K. All PMFs are defined to be zero outside of the droplets or slabs and thus quantify the free energy difference with respect to the internal bulk volume of water. The coordinate $r[z]$ is expressed in terms of the radial distance [distance along the z direction]. $r[z] = 0$ is where the PMF is minimum at the interface. The statistical errors are computed by binning analysis.

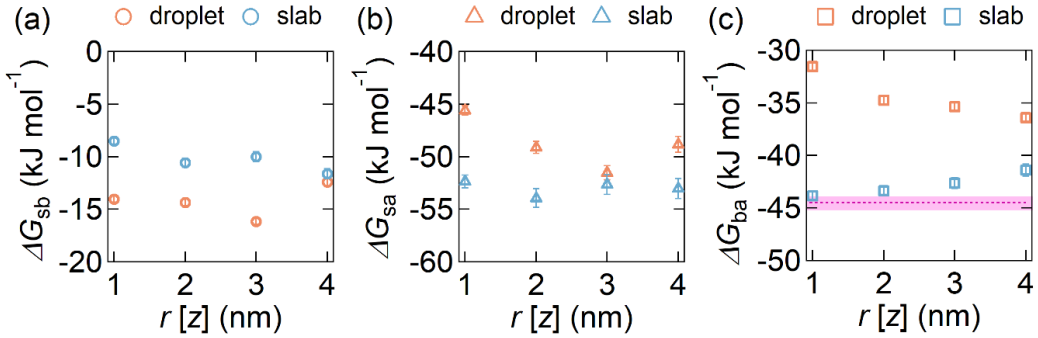

Figure 3: The differences of the free energy for succinic acid among the bulk, the surface and the air in different sizes of droplet (orange markers) and slab (blue markers) systems at 298.15 K. ΔG_{sb} (a), ΔG_{ba} (b), and ΔG_{sa} (c) are the free energy differences of the transition of the solute from the internal bulk volume to the liquid-vapor interface, the gas to the internal bulk volume of liquid, and the gas phase into the liquid-vapor interface, respectively. The pink block in (c) represent the free energy of hydration of succinic acid in bulk solutions ΔG_{hyd} by TI method calculation based on GAFF with ESP force field for succinic acid and TIP4P/2005 force field for water molecules (Fig. S1 and SI).

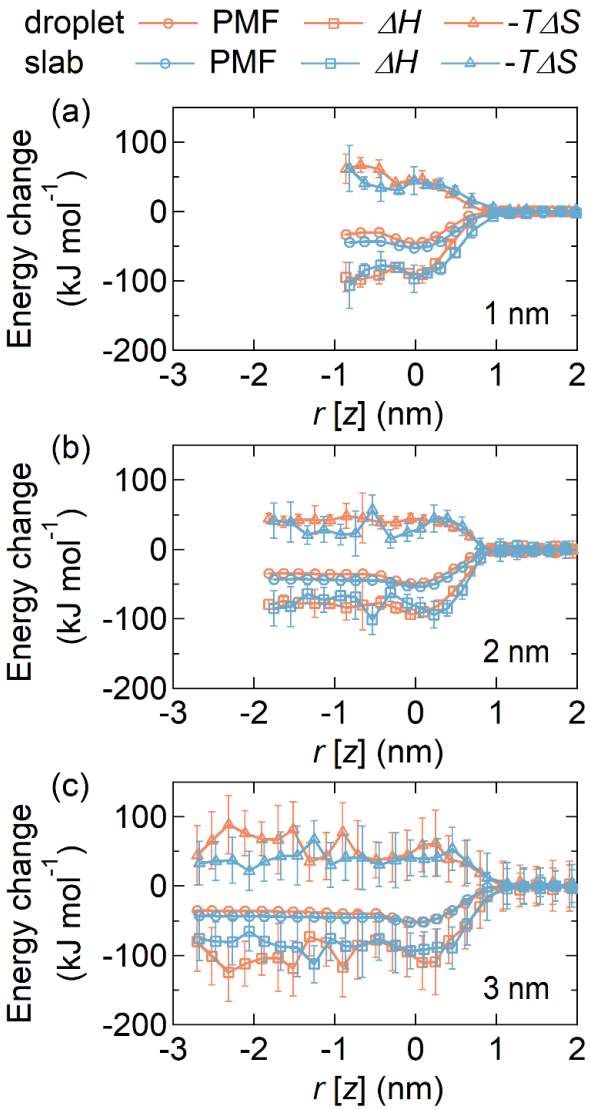

Figure 4: Decomposition of the potential of mean forces into enthalpic components and entropic components with different sizes in the droplet (radius) and slab (half slab thickness) systems. The lines with open circles represent the PMF profiles, the lines with open rectangles represent the enthalpic components (ΔH), and the lines with open triangles represent the entropic components ($-T\Delta S$).

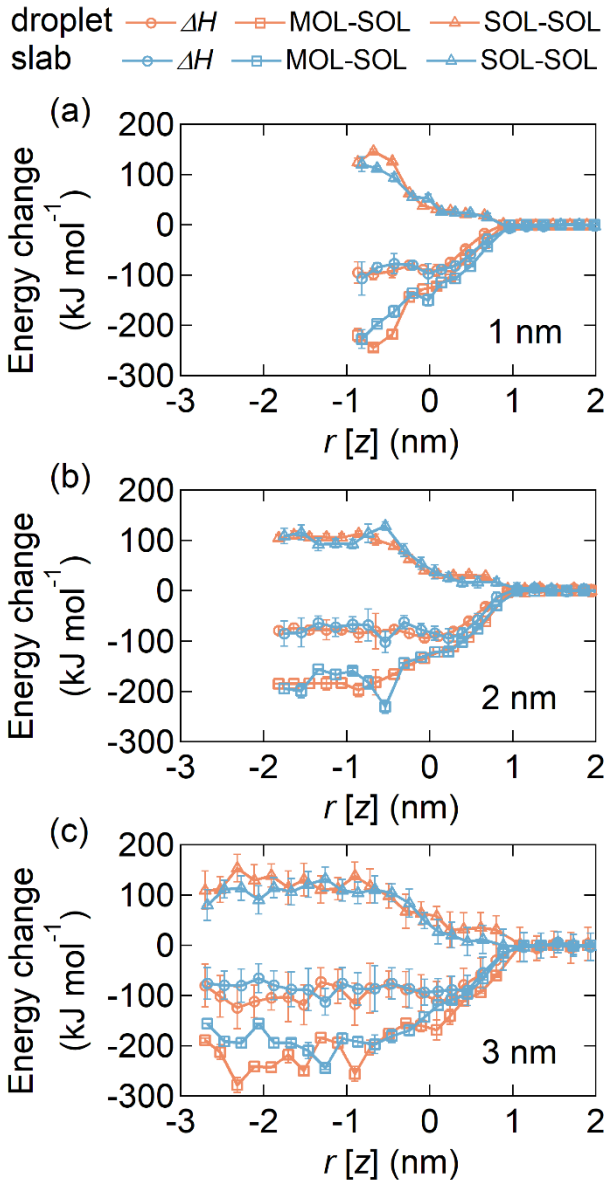

Figure 5: Decomposition of the enthalpic component into succinic acid-water and water-water interactions with different sizes in the droplet (radius) and slab (half slab thickness) systems. The lines with open circles represent the enthalpic components (ΔH), the lines with open rectangles represent the succinic acid-water interactions (MOL-SOL), and the lines with open triangles represent the water-water interactions (SOL-SOL).

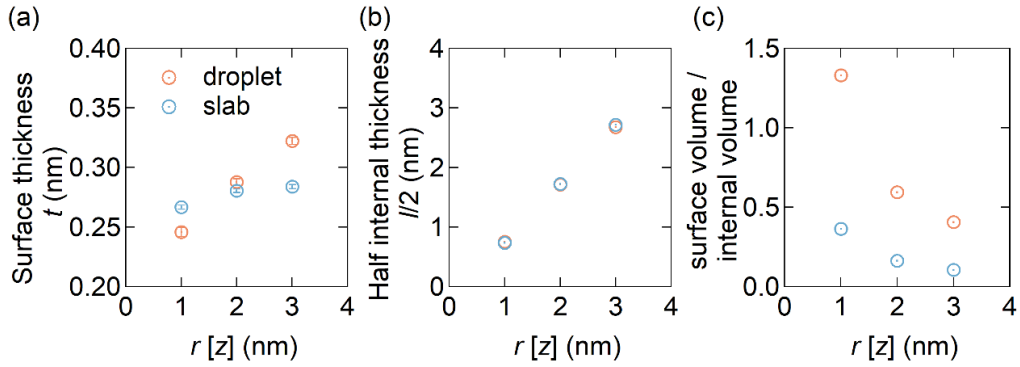

Figure 6: Structures of the droplet and slab systems with different sizes at 298.15 K. (a) Surface thicknesses of the droplet and slab systems. (b) Half internal thicknesses of the droplet and slab systems. (c) Ratio of surface volume versus internal bulk volume of the droplet and slab systems.

Energetic analysis of succinic acid in water droplets: insight into the size-dependent solubility of atmospheric nanoparticles

For Table of Contents Only (TOC)

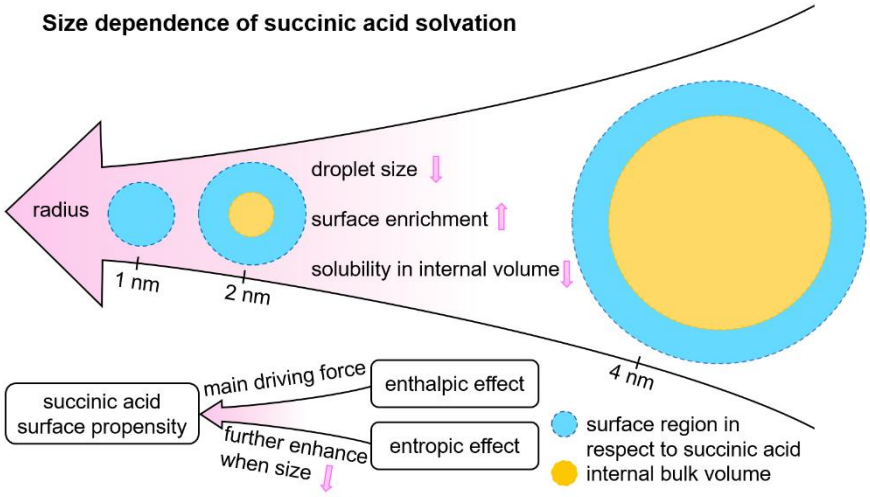

Supplementary Information

S1. Gibbs energy of hydration for force field selection

We computed the hydration free energy (ΔG_{hyd}) of one single succinic acid molecule in a box of water using thermodynamic integration (TI) (Kirkwood, 1935) to choose the reasonable force fields for the following PMF calculations. Five different combinations of force fields were used. The Generalized Amber force field (GAFF) (Wang et al., 2004) with the electrostatic potential (ESP) (Case et al., 2006) calculated charges (B3LYP/aug-cc-pVTZ) for the succinic acid was combined with several force fields: SPC (Berendsen et al., 1981), SPC/E (Berendsen et al., 1987), TIP3P (Jorgensen et al., 1983), TIP4P (Jorgensen et al., 1983), and TIP4P/2005 (Abascal and Vega, 2005) for the water molecules.

The TI simulations were computed with GROMACS 2016.5 (Van Der Spoel et al., 2005) at 298.15 K following the protocol of Shirts et al. (2003). One single succinic acid molecule was set in a cubic box of the volume 27 nm^3 with 877 water molecules. Contribution of Lennard-Jones and Coulomb interactions between the succinic acid molecule and the water molecules in the box for the thermodynamic integration were carried out using an alchemical reaction coordinate λ, where $\lambda = 0$ to $\lambda = 1$ correspond to the initial and final state, respectively. The interaction range was decomposed into 21 equally spaced λ-steps, and each λ-step was initially equilibrated for 200 ps then simulated for 500 ps. The free energy differences for each step was subsequently calculated by integrating $\langle \partial \mathcal{H} / \partial \lambda \rangle$ from $\lambda = 0$ to $\lambda = 1$. $\langle . \rangle$ denotes the average computed from the respective trajectory, where $\mathcal{H}$ is the Hamiltonian of the system. ΔG_{hyd} is the sum of the free energy differences from $\lambda = 0$ to $\lambda = 1$. In the context of computer simulations, such a use of TI methods is standard (Frenkel et al., 1996).

The experimental free energy of hydration ($\Delta G_{\mathrm{hyd,exp}}$) pertinent to the TI simulations with a single solute molecule was implemented as (Sander, 1999; Roeselová et al., 2004)

$$\Delta G_{\mathrm{hyd,exp}} = \Delta G^{0}_{\mathrm{hyd,exp}} + RT \ln\left(\frac{p_0}{c_0 RT}\right) \tag{S1}$$

where $\Delta G^{0}_{\mathrm{hyd.exp}}$ is the experimental hydration free energy corresponding to the standard state of p_0 = 1 atm gas pressure and c_0 = 1 mol L^{-1} aqueous concentration, R

is the universal gas constant and T = 298.15 K for the standard state. $\Delta G^0_{\mathrm{hyd.exp}}$ can be calculated from Henry's law constant k_{H} according to (Sander, 1999)

$$\Delta G^0_{\mathrm{hyd.exp}} = -RT \ln\left(\frac{p_0}{c_0} k_{\mathrm{H}}\right) \tag{S2}$$

k_{H} ranging from 3.0×10^6 to 4.1×10^7 mol m^{-3} Pa^{-1} in this study was obtained as an average value from Sander (2015).

As shown in Fig. S1, ΔG_{hyd} from the combination of GAFF with ESP for the succinic acid molecule and TIP4P/2005 for water molecules is closest to $\Delta G_{\mathrm{hyd,exp}}$ compared with the other four combinations (Zhang et al., 2018). Therefore, we selected the force field combination of GAFF with ESP for the succinic acid molecule and TIP4P/2005 for water molecules for the following calculations. In view of the approximate character of all force fields for water, discrepancies between calculations and experiment as seen in Fig. S1 are inevitable.

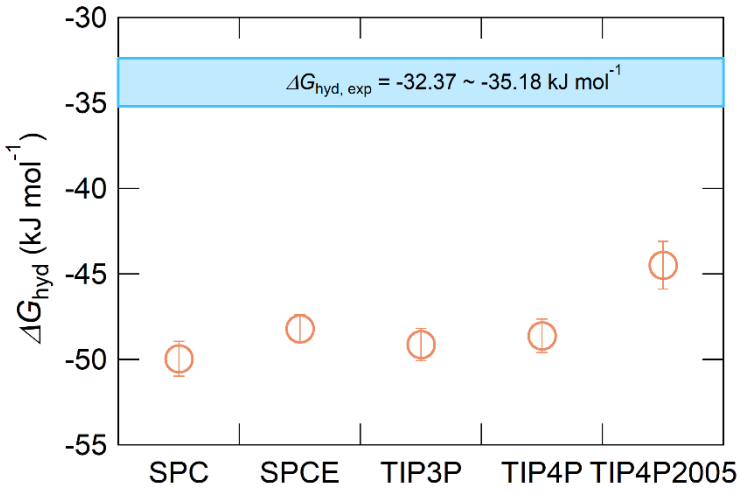

Figure S1. Gibbs energy of hydration (ΔG_{hyd})(kJ/mol) at 298.15K for succinic acid using five different force field-water model combinations. The light blue zone represents the experimental free energy of hydration ($\Delta G_{\mathrm{hyd,exp}}$). ”

4. Molecular dynamics simulation of the surface tension of aqueous sodium chloride: from dilute to highly supersaturated solutions and molten salt

This work is published in ACP as Wang et al. (2018):

Wang X, Chen C, Binder K, et al. Molecular dynamics simulation of the surface tension of aqueous sodium chloride: from dilute to highly supersaturated solutions and molten salt[J]. Atmospheric Chemistry and Physics, 2018, 18(23): 17077-17086.

I am the co-author of this work and my contribution to this work includes giving technical supports in numerical modelling and calculation as well as discussing the results including the molecular dynamics simulations and energetic analyses data, giving comments on the manuscript.

The following text, figures, and tables quoted (within "") from page 86 to page 106 are the same as published on Wang et al. (2018) which is cited on page 85.

"**Abstract**

Sodium chloride (NaCl) is one of the key components of atmospheric aerosols. The surface tension of aqueous NaCl solution ($\sigma_{NaCl,sol}$) and its concentration dependence are essential to determine the equilibrium water vapor pressure of aqueous NaCl droplets. Supersaturated NaCl solution droplets are observed in laboratory experiments and under atmospheric conditions, but the experimental data for $\sigma_{NaCl,sol}$ are mostly limited up to sub-saturated solutions. In this study, the surface tension of aqueous NaCl is investigated by molecular dynamics (MD) simulations and pressure tensor method from dilute to highly supersaturated solutions. We show that the linear approximation of concentration dependence of $\sigma_{NaCl,sol}$ at molality scale can be extended to the supersaturated NaCl solution until a molality of ~10.7 mol kg^{-1} (i.e., solute mass fraction (x_{NaCl}) of ~0.39). Energetic analyses show that this monotonic increase of surface tension is driven by the increase of excess surface enthalpy (ΔH) as the solution becomes concentrated. After that, the simulated $\sigma_{NaCl,sol}$ remains almost unchanged until x_{NaCl} of ~0.47 (near the concentration upon efflorescence). The existence of the "inflection point" at x_{NaCl} of ~0.39 and the stable surface tension of x_{NaCl} between ~0.39 and ~0.47 can be attributed to the nearly unchanged excess surface entropy term ($T \cdot \Delta S$) and the excess surface enthalpy term (ΔH). After a "second inflection point" at x_{NaCl} of ~0.47, the simulated $\sigma_{NaCl,sol}$ gradually regains the growing momentum with a tendency to approach the surface tension of molten NaCl (~175.58 mN m^{-1} at 298.15 K, MD simulation based extrapolation). This fast increase of $\sigma_{NaCl,sol}$ at x_{NaCl} > 0.47 is a process driven by excess surface enthalpy and excess surface entropy. Our results reveal different regimes of concentration dependence of the surface tension of aqueous NaCl at 298.15 K: a water-dominated regime (x_{NaCl} from 0 to ~0.39), a transition regime (x_{NaCl} from ~0.39 to ~0.47) and a molten NaCl-dominated regime (x_{NaCl} from ~0.47 to 1).

Introduction

Sodium chloride (NaCl) is one of the most important components of atmospheric aerosol particles (Finlayson-Pitts, 2003; Lewis and Schwartz, 2004). The

aqueous NaCl solution droplet could participate in many atmospheric processes, such as phase transition, cloud activation, ice crystallization, long-range transport and chemical aging (Martin, 2000; Finlayson-Pitts, 2003; Ghorai et al., 2014; Wagner et al., 2015; Chen et al., 2016). To better understand these processes, the concentration-dependent surface tension of aqueous NaCl solution ($\sigma_{NaCl,sol}$) is essential to determine the equilibrium between NaCl solution droplet and water vapor (Jarvis and Scheiman, 1968; Dutcher et al., 2010).

Below saturation point (~6.15 mol kg $^{-1}$), $\sigma_{NaCl,sol}$ shows a near linear dependence on molality (Jarvis and Scheiman, 1968; Johansson and Eriksson, 1974; Aveyard and Saleem, 1976; Weissenborn and Pugh, 1995; Matubayasi et al., 2001) with a slope of 1.73±0.17 (Pegram and Record, 2006, 2007). Because of the energy barrier of crystallization during dehydration and size-effects at the nanoscale (Martin, 2000; Biskos et al., 2006; Cheng et al., 2015), supersaturated aqueous NaCl solution droplets can exist under atmospheric conditions. However, direct measurements of surface tension of supersaturated droplets are challenging due to technical difficulties (Harkins and Brown, 1919; Vargaftik et al., 1983; Richardson and Snyder, 1994; Kumar, 2001). Only recently, Bzdek et al. (2016) overcame this limitation with an optical tweezer method and extend the concentration range to ~8 mol kg $^{-1}$, where the near linear relationship still holds (Bzdek et al., 2016).

It is a matter of debate to which extent the approximation of a near linear dependence of surface tensions on molality can still be used for NaCl droplets. Cheng et al. (2015) used the Differential Köhler Analyses (DKA) method to retrieve the surface tension of NaCl aqueous droplets, and revealed a large deviation from the near linear increase at molality of ~10 mol kg^{-1}. In literature, such deviation in concentrated solution has also been found for other compounds, such as HNO_3 (Weissenborn and Pugh, 1996) and it is believed to be typically true for most highly soluble electrolytes (Dutcher et al., 2010). The reason for such deviation remains unclear.

Several models about surface tension have been developed for highly concentrated solutions, e.g., Li and Lu (2001), Li et al. (1999), Levin and Flores-Mena (2001). Li and Lu (2001) developed a model based on the Gibbs dividing surface concept, where the adsorption and desorption rate constants, saturated surface excess, stoichiometric coefficient of ions and mean ionic activity coefficient are needed. For NaCl aqueous solution, this model is suitable for solution with concentration up to ~5.5

mol kg $^{-1}$. Li et al. (1999) uses Debye-Huckel parameter, osmotic coefficient and a proportionality constant from the fitting of measured values to calculate the surface tension, which covers the concentration until saturation point of bulk NaCl aqueous solutions. The remaining models are mostly only suitable for the dilute electrolyte solutions, such as the one proposed by Levin and Flores-Mena (2001). In their valid concentration range, these surface tension models produce linear or near linear concentration dependence of $\sigma_{NaCl,sol}$ that agrees well with currently available observations.

One surface tension model that is able to predict $\sigma_{NaCl,sol}$ in the whole concentration range from infinitely dilute (x_{NaCl} = 0) to highly supersaturated solution to molten salts (x_{NaCl} = 1) was proposed by Dutcher et al. (2010), which has been adopted into the widely used Extended Aerosol Inorganics Model (E-AIM) (Wexler and Clegg, 2002). This model is based on the following concept: ions are solvated by the water at low salt concentrations, which means that water molecules form hydration shells around the ions; while at very high salt concentration the water is considered as "solute" that is solvated by the ions, which means that ions forms shells around the water molecules (Dutcher et al., 2010). Accordingly, for a diluted solution, the surface tension of water dominates and the surface tension of the solution equals the surface tension of water adjusted by a term that is proportional to the solute concentration. For a highly supersaturated solution, a similar relationship can be applied with the surface tension of molten salt as governing element. Legitimately, the model is then constrained by the surface tensions of water and molten salt. The parameterization of this model is obtained by fitting the data of sub-saturated solutions. When the aqueous NaCl solution gets concentrated, this model shows a nonlinear monotonically increasing trend of $\sigma_{NaCl,sol}$ generally in good agreement with observations, but no "inflection point" was introduced. It should be noted that the surface tension as a function of mole fraction of NaCl according to the Dutcher et al. (2010) model is essentially a linear interpolation between the surface tensions of water and molten NaCl.

In this study, we applied molecular dynamics (MD) simulations and pressure tensor method to calculate the concentration dependence of $\sigma_{NaCl,sol}$ from infinitely dilute (x_{NaCl} = 0) to highly supersaturated solution to molten salt (x_{NaCl} = 1). The concentration dependence of $\sigma_{NaCl,sol}$ is divided into 3 regimes: a water-dominated regime, a transition regime and a molten NaCl-dominated regime. We compare our

results with the Dutcher et al. (2010) model, and present the principal underlying physical chemistry (driving forces) behind the change of surface tension along concentration changes.

Methods

MD simulation

MD simulations were carried out with the GROMACS 5.1 package (Abraham et al., 2015). The Na^+ ions, Cl^- ions and water molecules were added into a cubic box (L = 5 nm) to imitate the NaCl solution. The concentrations of simulated solutions are summarized in Table 1. To simulate the surface tension of supersaturated NaCl aqueous solution, we make use of the time window in the MD simulations before the crystallization starts in the system. The highest x_{NaCl} we can reach is ~0.64 (the corresponding concentration is ~30.39 mol kg^{-1}), below which the simulated surface tensions in three independent runs stably converge after 50 to 100 ns (Fig. 1). For more concentrated solutions, stable convergence cannot be reached, as for example large fluctuations are shown in Fig. 1d at x_{NaCl} of 0.75.

According to Dutcher et al. (2010), surface tension of liquid/molten NaCl at 298.15 K (corresponding x_{NaCl} is 1, infinite concentrated solution) can be regarded as the upper boundary of $\sigma_{NaCl,sol}$. However, a direct simulation of surface tension of molten NaCl at 298.15 K would not be possible, due to excessively large relaxation times of this system at this temperature. It has been found that surface tensions of a very wide range of molten salts can be well described by linear functions of temperature (Sada et al., 1984; Horvath, 1985; Janz 1988; Dutcher et al., 2010). We thus follow the approach of Dutcher et al. (2010) assuming a linear relationship between surface tension of molten NaCl and temperature. With this approach, we retrieve the surface tension of molten NaCl at 298.15 K by extrapolating the simulated surface tension of molten NaCl in the temperature range of 1000 K to 1700 K. Note that, in principle, non-linearity could still be possible at very high degrees of supercooling (e.g., close to or at room temperature) for the molten salts, which may introduce uncertainties to the offset obtained by the extrapolation.

The procedure of simulation we followed is (Fig. 2): (1) systems were firstly energetically minimized by the steepest-descent method (Stillinger and Weber, 1985) (2) Solutions were equilibrated in the *NVT* ensemble and *NPT* ensemble (pressure = 1

bar) with periodic boundary conditions in three directions. The temperature was controlled by using the Nosé–Hoover thermostat (Nosé 1984; Hoover 1985). The box volume change due to the variation of density at different temperatures, and in our case the length of cubic box varied from 4.9 nm to 5.1 nm. (3) The box was elongated along the z-direction with L_z = 20 nm to create two interfacial regions. (4) The solution was equilibrated and simulated with the *NVT* ensemble in the rectangular parallelepiped box at the corresponding temperature. (5) Systems without surfaces were also simulated for further energy analysis, and the trajectories obtained from step 2 were simulated with *NPT* ensemble. (6) All simulations were carried out for at least 200 ns, which is much longer than that in previous studies (a few nanoseconds, Jungwirth and Tobias, 2000; Neyt et al., 2013) because the system that we were dealing with is much more concentrated. 1 fs time step was adopted and conformations for analysis were saved every 2 ps. Both electrostatic interactions and van der Waals interactions were calculated using the particle mesh Ewald (PME) algorithm, which has been proven to be a good choice for accurate calculation of long-range interactions (Essmann et al., 1995; Fischer et al., 2015). To test the reproducibility, all the systems were simulated 3 times, and the respective statistical error bars were provided.

In our simulation, the Joung-Cheatham (JC) force field for NaCl (Joung and Cheatham III, 2009) with SPC/E water model (Berendsen et al., 1987) was applied to simulate the NaCl solution and molten NaCl. The solubility at 298.15 K based on JC force field with SPC/E model has been determined as 3.7±0.2 mol kg^{-1} (Moučka et al., 2013; Mester and Panagiotopoulos, 2015; Espinosa et al., 2016), which to our best knowledge is the value most close one to the experimental value of solubility (~6.15 mol kg^{-1}). Therefore, this force field is appropriate to be used to study the concentration dependence of properties. More details about the history of the attempts to correctly calculate the quantity by molecular simulation can be found in Nezbeda et al.'s review (2016).

Calculation of Surface Tension

Based on results from MD simulations, the surface tension was calculated by using the mechanical definition of the atomic pressure (Alejandre et al., 1995):

$$\sigma_{MD} = 0.5L_z\left[\langle P_{zz}\rangle - 0.5\left(\langle P_{xx}\rangle + \langle P_{yy}\rangle\right)\right] \quad (1)$$

where σ_{MD} can represent the surface tension of molten NaCl (σ_{NaCl}), NaCl solution ($\sigma_{NaCl,sol}$) or pure water (σ_{water}), L_z is the length of the simulation cell in the longest direction (along z-axis) and P_{aa} (a=x, y, z) denotes the diagonal component of the pressure tensor. The $\langle ... \rangle$ refers to the time average. The factor 0.5 outside the squared brackets takes into account the two interfaces in the system. Only the stable values were taken as our calculated surface tension.

Energy analysis

The excess surface enthalpy denotes the additional enthalpy in the system due to the creation of surfaces. It can be calculated as the difference of enthalpy between solutions with and without surfaces (Bahadur et al., 2007),

$$\Delta \mathrm{H} = H_{b_s} - H_b \tag{2}$$

where H_{b_s} is the total enthalpy of simulated systems with surfaces and H_b is the total enthalpy of simulated systems without surfaces. As the kinetic energy is the same for systems with or without surfaces and the difference of pV can be ignored, ΔH can be presented as

$$\Delta \mathrm{H} = E_{b_s} - E_b \tag{3}$$

where E_{b_s} and E_b are the potential energy of the system with and without surfaces.

Then the surface tension can be determined by the excess surface free energy per unit area as in Eq. (4) (Davidchack and Laird, 2003):

$$\sigma = \frac{\Delta \mathrm{G}}{\mathrm{A}} = \frac{\Delta \mathrm{H} - \mathrm{T} \cdot \Delta \mathrm{S}}{\mathrm{A}} \tag{4}$$

where ΔG is the increased part of free energy due to the creation of surfaces, A is the total area of the surface we created, so $A = 2 \times a$ and a is the area of each created surface. ΔS is the excess surface entropy. We then can retrieve ΔS by using the data of enthalpy and surface tension:

$$\Delta \mathrm{S} = \frac{\Delta H - \sigma \cdot A}{T} \tag{5}$$

ΔH and $\mathrm{T} \cdot \Delta \mathrm{S}$ per unit area ($\frac{\Delta \mathrm{H}}{\mathrm{A}}$ and $\frac{\mathrm{T} \cdot \Delta \mathrm{S}}{\mathrm{A}}$) are obtained as the enthalpic and entropic part of contributions to the net surface tension, which will be used to explain the change of surface tension along with the mass fraction of NaCl (x_{NaCl}).

Results and Discussion

Water-dominated regime (x_{NaCl} < ~0.39)

In Fig. 3a, the calculated surface tension of NaCl aqueous solution ($\sigma_{NaCl,sol}$) is compared with experimentally determined values (Jarvis and Scheiman, 1968; Johansson and Eriksson, 1974; Aveyard and Saleem, 1976; Weissenborn and Pugh, 1995; Matubayasi et al., 2001; Pegram and Record, 2006, 2007; Morris et al., 2015; Bzdek et al., 2016) in the sub-saturated concentration range (molality of NaCl solution from 0 to 6.15 mol kg^{-1} and x_{NaCl} from 0 to ~0.265). At 298.15 K, both model simulation (red solid points and fit line in Fig. 3a) and experimental observation (black line in Fig. 3a) reveal a linear dependence of surface tension on solution concentration at molality scale, with a very similar slope (2.1 versus 1.73±0.17, respectively). Systematic underestimation, however, exists in the simulated $\sigma_{NaCl,sol}$. The previous MD simulations by Neyt et al. (2013) has also reported a similar result for the solution whose concentration ranges from 0 to 5.2 mol kg $^{-1}$ by using the same water model (SPC/E) but two different NaCl force fields, i.e., Wheeler NaCl (solid dark blue triangle in Fig. 3a) and Relf NaCl (open light blue triangle in Fig. 3a). Bhatt et al. (2004) also used the Wheeler NaCl model and SPC/E water model revealing a linear dependence and underestimation. We also subtracted the experimentally determined and the MD simulated surface tension of pure water (σ_{water}) from the observed and modeled $\sigma_{NaCl,sol}$, respectively. The relative increase of surface tension ($\Delta\sigma = \sigma_{NaCl,sol} - \sigma_{water}$) from models and experiments converge nicely (Fig. 3b), and the former is only a little higher than the latter. The MD simulation is able to reproduce the increment in the growth of surface tension from pure water due to the addition of solute NaCl though the predicted absolute value of $\sigma_{NaCl,sol}$ is systematically underestimated, which may mainly be attributed to the discrepancy between observed σ_{water} and the modeled ones from the SPE/C water model.

By performing MD simulations in the supersaturated concentration range, we found that this linear relationship still holds beyond the saturation point until x_{NaCl} of ~0.39 (Fig. 4). As mentioned above, the laboratory experiments with elevated NaCl aqueous droplet and the optical tweezer method show that the linear relationship between $\sigma_{NaCl,sol}$ and NaCl concentration (molality scale) can be extended to ~8 mol kg^{-1} (Fig. 3) (Bzdek et al., 2016), corresponding to x_{NaCl} of ~0.33 (Fig. 4), which is consistent with our simulations.

Transition regime (x_{NaCl} from ~0.39 to ~0.47)

It was often found that surface tensions of single inorganic electrolyte aqueous solution were linear functions of concentration (at the molality scale) over moderate concentration range (Talbot, 1987; Dutcher et al., 2010). However, these simple relationships may not hold when the solutions become more concentrated. As shown in Fig. 4, starting from x_{NaCl} ~0.39, the simulated $\sigma_{NaCl,sol}$ remains almost unchanged until x_{NaCl} of ~0.47 (concentration upon efflorescence). This "inflection point" of $\sigma_{NaCl,sol}$ at x_{NaCl} of ~0.39 is supported by those determined by the DKA approach (Cheng et al., 2015), where a large deviation of surface tension from the monotonic linear increase. Note that beyond x_{NaCl} of ~0.47, the simulated surface tension increases again (Fig. 4). This "second inflection point", right at the concentration upon efflorescence, may imply potential correlation with crystallization processes.

Molten NaCl-dominated regime (x_{NaCl} > ~0.47)

Beyond the "second inflection point" (x_{NaCl} > 0.47), the simulated $\sigma_{NaCl,sol}$ gradually increases more and more strongly (Fig. 4). Unfortunately, due to the large fluctuation in the surface tension simulation (Fig. 1), we are not able to extend our surface tension calculation in this way beyond x_{NaCl} of ~0.64. However, according to Dutcher et al. (2010), it is expected that the surface tension of the solution would ultimately approach the surface tension of the hypothetical molten solute (i.e., $x_{NaCl} = 1$) at the same temperature. This hypothesis has been found to be consistent with the DKA retrieval for a highly concentrated ammonium sulfate aqueous solution with molality of ~380 mol kg^{-1} (Cheng et al., 2015). We thus also try to constrain the growth of $\sigma_{NaCl,sol}$ by MD simulated surface tension of molten NaCl (σ_{NaCl}) at 298.15 K.

Similar to Janz (1988)'s experimental results, the simulated σ_{NaCl} is also linearly correlated with temperature from 1000 K (the simulated melting point of NaCl) to 1700 K, as shown in Fig. 5. Following Dutcher et al. (2010), a surface tension of ~175.58 mN m^{-1} is obtained for the hypothetical molten NaCl at 298.15 K by linear extrapolation of the MD simulated σ_{NaCl} at higher temperature, which is very close to the ~169.7 mN m^{-1} extrapolated from the experimental results (Dutcher et al., 2010). Combined with $\sigma_{NaCl} = \sigma_{NaCl,sol}(x_{NaCl} = 1)$ = ~175.58 mN m^{-1}, the simulated $\sigma_{NaCl,sol}$ in the concentration range of x_{NaCl} > 0.47 shows the tendency to ultimately

approaching the surface tension of melting NaCl at 298.15 K, similar to the blue curve in Fig. 4 from the Dutcher et al. (2000) study.

Physical chemistry behind the regimes

In energetic analyses, surface tension was decomposed into excess surface enthalpy ($\frac{\Delta H}{A}$) and excess surface entropy ($\frac{T \cdot \Delta S}{A}$). Note that the increase in excess surface entropy ($\frac{T \cdot \Delta S}{A}$) or decrease of $-\frac{T \cdot \Delta S}{A}$ will contribute negatively to the growth of $\sigma_{NaCl,sol}$. The analyses show that the monotonic increase of surface tension in water-dominated concentration ranges (x_{NaCl} from 0 to ~0.39) is driven by the increase of $\frac{\Delta H}{A}$ when the solution becomes concentrated (Fig. 6). When the solution gets concentrated, $\frac{\Delta H}{A}$ first increases slightly with enhanced increasing rate at $x_{NaCl} >$ ~0.2 and in the supersaturated regime up to x_{NaCl} of ~0.39. $-\frac{T \cdot \Delta S}{A}$ behaves differently, it remains almost constant at about -45 mN m^{-1} first and only starts to decrease at x_{NaCl} ~0.2. This way, in this concentration range (x_{NaCl} from 0 to ~0.39), the increase of excess surface enthalpy outnumbers the increase of excess surface entropy and thus this physicochemical regime can be understood as an excess surface enthalpy-driving process.

The stable surface tension in the transition-regime concentration range (x_{NaCl} from ~0.39 to ~0.47) is attributed to that $-\frac{T \cdot \Delta S}{A}$ and $\frac{\Delta H}{A}$ are both almost unchanged. Figure 6 shows that in the concentration above x_{NaCl} of ~0.39, the increase of $\frac{\Delta H}{A}$significantly slows down and stabilizes at ~145 mN m^{-1} when the mass fraction approaches the efflorescence point. During this period, $-\frac{T \cdot \Delta S}{A}$ keeps nearly unchanged, which results in a corresponding $\sigma_{NaCl,sol}$ almost independent to the solution concentration change.

Here, we present a potential explanation for the stability of surface tension in this region from the structural analysis. The ratio of Na^+ concentration at different positions to the average concentration of the whole system ($C_z/C_{average}$) in different solutions is shown in Fig. 7a. The three blue-toned lines represent the ratio of solution in the transition regime with x_{NaCl} from ~0.39 to ~0.47. All of them have apophysises (significant rise) near the surface and these apophysises almost overlap with each other. This phenomenon suggests that the solute in these solutions enriches close to the surface

and the degree of enrichment is almost the same for the different-concentration solution. Here, we denote the significant difference of the solute concentration in bulk region and on surface as a type of liquid-liquid partitioning. To check if this partitioning is dependent on the size of solution slab, we calculate the corresponding value of a 3 nm × 3 nm × 10 nm solution slab with x_{NaCl} of 0.4 (Fig. 7b). There is still an apophysis near surface, thus we can claim that the partitioning is independent of the size of solution slab in the simulation. Note that this surface enrichment of NaCl does not mean that NaCl is enriched right on top of the solution surface. Actually the density profile of water extends about 0.2 nm beyond that of NaCl towards the vapor region. By contrast, the solution with x_{NaCl} >0.47 or <0.39 do not have this type of partitioning as shown by the red and green lines. This comparison implies that the stability of surface tension of solution with x_{NaCl} from ~0.39 to ~0.47 is related to the "bulk-surface" partitioning. This interpretation is only a conjecture, and more studies are needed to further examine this phenomenon and interpretation. The shallow minimum in the density profile for x_{NaCl} between 0.39 and 0.47 to the left of the maximum is somewhat unexpected, and one might expect equilibration problems. However, we have checked that this structural feature develops already during the first 10 ns of the MD simulation, and does not change at all during the residual 200 ns. Surface enrichment of NaCl can be expected, however, when the solubility limit of the water-rich solution in the bulk is reached. Very roughly, such phenomena are analogous to interfacial wetting phenomena such as surface melting of crystals (Frenken and Van der Veen, 1985), which sometimes is observed when the temperature is raised towards the triple point. In our case, the enrichment zone of NaCl (which is about 0.4 nm thick in Fig.7) would be a precursor effect to the (metastable) NaCl-rich bulk solution. Tentatively, one may correlate the formation of the enrichment zone with the stability of the surface entropy in this region via the entropy of mixing. At the same time, the surface enhancement of ions may be related to the phenomenon of efflorescence.

As shown in Fig. 6, when a solution gets more concentrated from x_{NaCl} of ~0.47 to ~0.64, the $\frac{\Delta H}{A}$ slightly increases from the plateau of ~145 mN m^{-1} but the change is only ~5 mN m^{-1}. The $-\frac{T\cdot\Delta S}{A}$ keeps increasing. So during this period, both surface excess enthalpy term and entropy term contribute to the growth of $\sigma_{NaCl,sol}$. To constrain the energetic analyses, the $\frac{T\cdot\Delta S}{A}$ and $\frac{\Delta H}{A}$ were also calculated for the molten NaCl at 298.15

K. According to Fig. 5, we have $\sigma_{NaCl} = -0.0755 \cdot T + 198.09$, then we can get $\frac{\Delta S_{NaCl}}{A}$ = 0.0755 mN m^{-1} K^{-1} because of $\frac{\Delta S(T)}{A} = \frac{-d\sigma(T)}{dT}$ (Landau and Lifshitz, 1969). Therefore, for molten NaCl (x_{NaCl} = 1.0), $\frac{T \cdot \Delta S_{NaCl}}{A}$ at 298.16 K is 22.15 mN m^{-1}, and $\frac{\Delta H_{NaCl}}{A}$ at 298.15 K is 198.09 mN m^{-1} (Fig. 6). Here, we used the derivative of temperature-surface tension relation to calculate the excess surface entropy, and more discussions about the comparison of these methods can be found in the supplement (Fig. S1). According to Fig. 6, it is expected that excess surface enthalpy term will still have a large amount (about more than 50 mN m^{-1}) to grow until approaching $\frac{\Delta H}{A}$ of molten NaCl at 298.15 K. It is similar for surface excess entropy term while the increment is smaller. Thus, the fast increase in $\sigma_{NaCl,sol}$ in the concentration of x_{NaCl} from ~0.47 to 1 can be assumed to be a process driven by excess surface enthalpy and excess surface entropy.

Conclusion

The analysis based on the calculated surface tension confirms the basic concept of the Dutcher et al. (2010) semi-empirical model, while unfold a more detailed global landscape of concentration dependence of surface tension of aqueous NaCl solution and its driving forces: (1) a water-dominated regime (x_{NaCl} from 0 to ~0.39, at low concentrations ions are solvated by the water molecules, which means that water-structures/hydration shells are formed around ions); (2) a transition regime (x_{NaCl} from ~0.39 to ~0.47); and (3) a molten NaCl-dominated regime (x_{NaCl} from ~0.47 to 1, at very high salt concentration water molecules are solvated by the ions, which means that a salt-structure is formed around the water molecules). Note that our result may not exactly reflect the real mode of surface tension of NaCl solution along the concentration, but it does imply the concept of a non-monotonic change of surface tension. One must be aware that for nucleation processes in the atmosphere also other chemical compounds matter, and will require future study. Also, mixed salt solutions would be very interesting, and can in principle be studied with similar simulation methods as applied here; however, this task must be left to future work.

Table 1. Concentrations of solution studied in our simulation and the calculated values of surface tension.

NO.	Number of water	Number of NaCl	Concentration (mol kg^{-1}) in bulk region [b]	x_{NaCl} in bulk region	Concentration (mol kg^{-1}) of whole solution	x_{NaCl} of whole solution	Surface tension (mN m^{-1})
1	4142	0	0	0	0	0	62.24±0.044
2	4058	42	0.657	0.037	0.575	0.0325	63.48±0.03
3	3976	83	1.235	0.067	1.159	0.0635	64.8±0.014
4	3824	159	2.41	0.123	2.309	0.119	67.41±0.089
5	3728	207	3.16	0.156	3.08	0.1528	69.49±0.006
6	3656	243	3.85	0.184	3.69	0.1776	70.76±0.1
7	3550	296	4.8	0.219	4.63	0.213	73.61±0.055
8	3452	345	6.04	0.261	5.552	0.245	76.06±0.14
9	3388	377	6.75	0.283	6.182	0.265	77.5±0.11
10	3314	414	7.47	0.304	6.94	0.288	79.7±0.19
11	3222	460	8.57	0.334	7.931	0.317	82.06±0.25
12	3108	517	9.745	0.36	9.24	0.351	84.35±0.143
13	3038	552	10.66	0.384	10.09	0.371	85.67±0.183
14	2960	591	11.83	0.409	11.09	0.3935	86.9±0.04
15	2868	637	13.49	0.44	12.339	0.419	87.83±0.25
16	2762	690	15.34	0.47	13.879	0.448	88.03±0.88
17	2636	753	17.37	0.504	15.87	0.481	88.77±0.42
18	2486	828	19.98	0.54	18.503	0.519	90.35±0.6
19	2368	887	24.6	0.59	20.81	0.549	93.4±2.157
20	2232	955	26.74	0.61	23.77	0.581	97.6±1.46
21	2122	1010	30.396	0.64	26.44	0.607	102.53±0.46
22[a]	2109	421	11.48	0.4018	11.09	0.3935	86.9±0.59

a. The solution slab in this system is 3 nm × 3 nm × 10 nm and the simulation box is 3 nm × 3 nm × 30 nm.

b. There is a little difference between the concentration in the bulk region and the one of the whole system due to surface effects. The values used in the main text are the ones in the bulk region

Figures

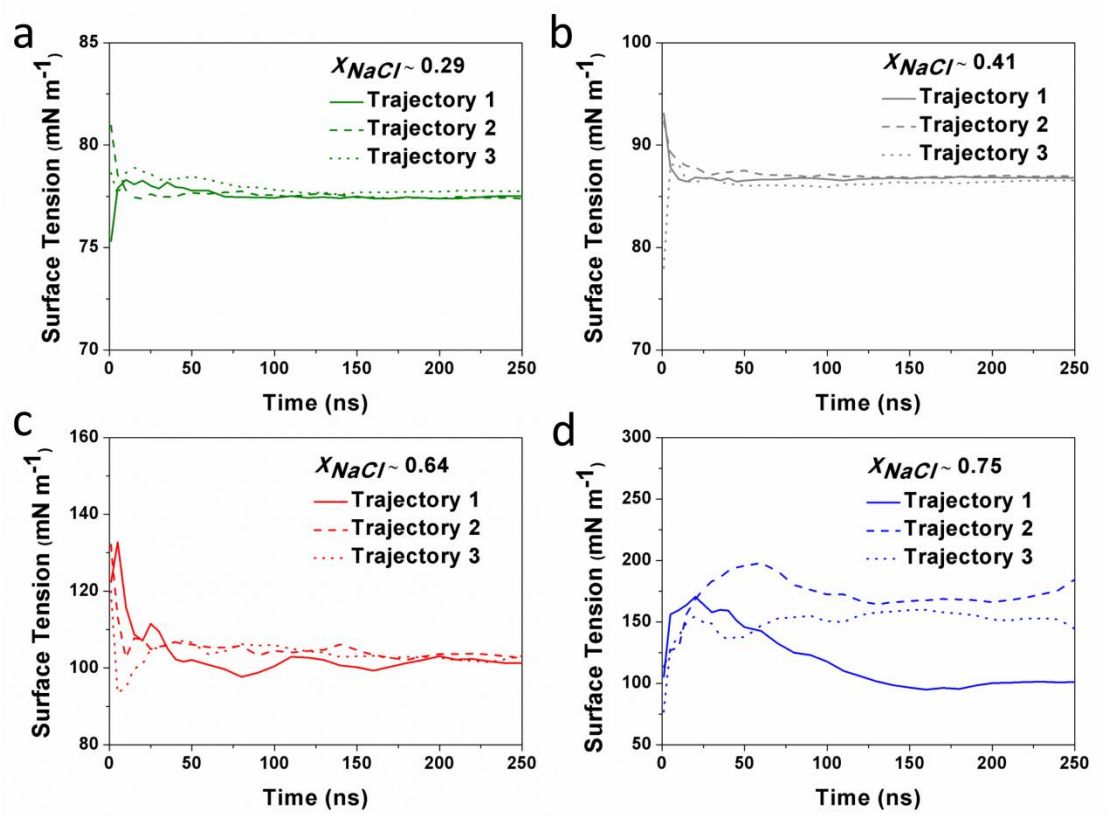

Figure 1. The calculated surface tension at different simulation time from different trajectories. For the solution with $x_{NaCl} \leq 0.64$ (a-c), the surface tension become steadily stabilized after ~100-150 ns, and different individual simulation runs converge to a similar result. When $x_{NaCl} > 0.64$ (d; here $x_{NaCl} = 0.75$), the surface tension keeps fluctuating and the final values from different individual simulations cannot be converged even after 250 ns.

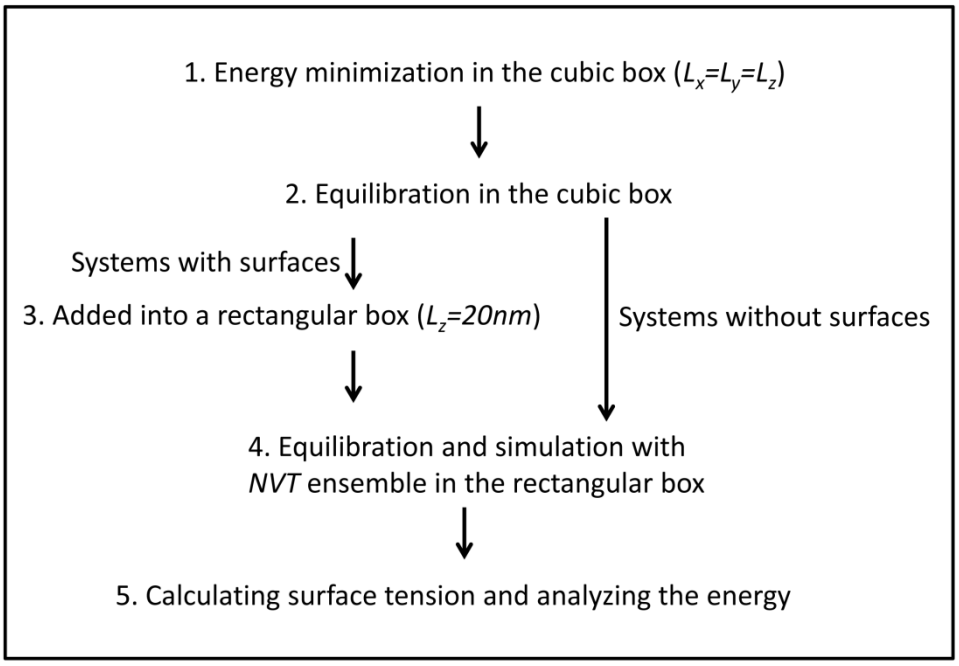

Figure 2. Schematic diagram of the different steps performed in the MD simulation.

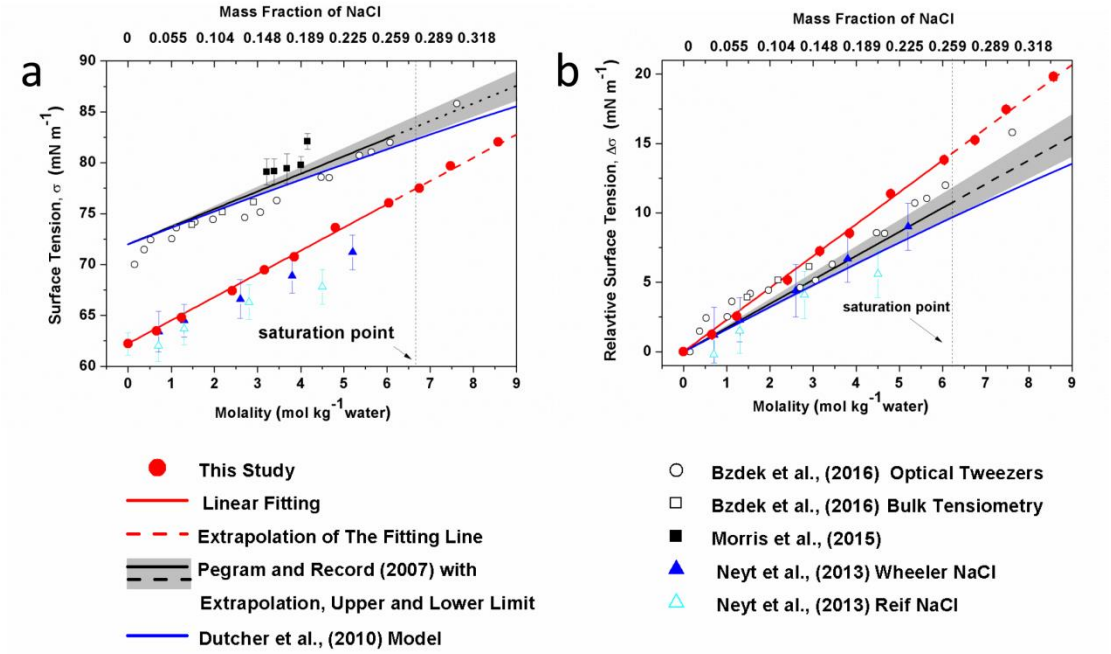

Figure 3. Surface tension (a) and relative surface tension (b) defined as $\Delta\sigma = \sigma_{solution} - \sigma_{water}$ as a function of the concentration of NaCl. The σ_{water} in the Morris et al. (2015) study was not determined, thus the corresponding $\Delta\sigma$ is not shown in panel b.

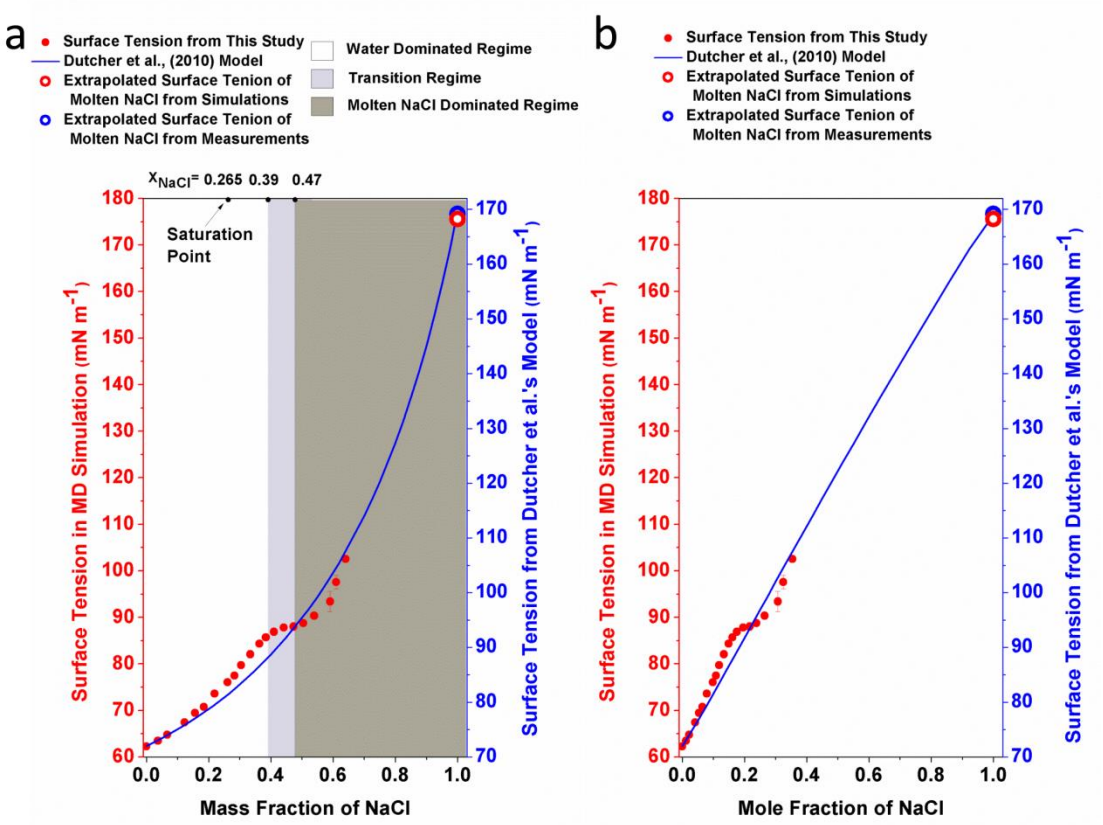

Figure 4. The surface tension of different-concentration NaCl solution. (a) The surface tension of NaCl solution against the mass fraction of NaCl. The left red y-axis is for the data from MD simulation (red circle), and the right blue y-axis is for the Dutcher et al. model (2010, blue solid line). The white, light grey and dark grey areas shade the water-dominated, transition and molten NaCl-dominated regimes, respectively. (b) The surface tension of NaCl solution is plotted against the mole fraction of NaCl.

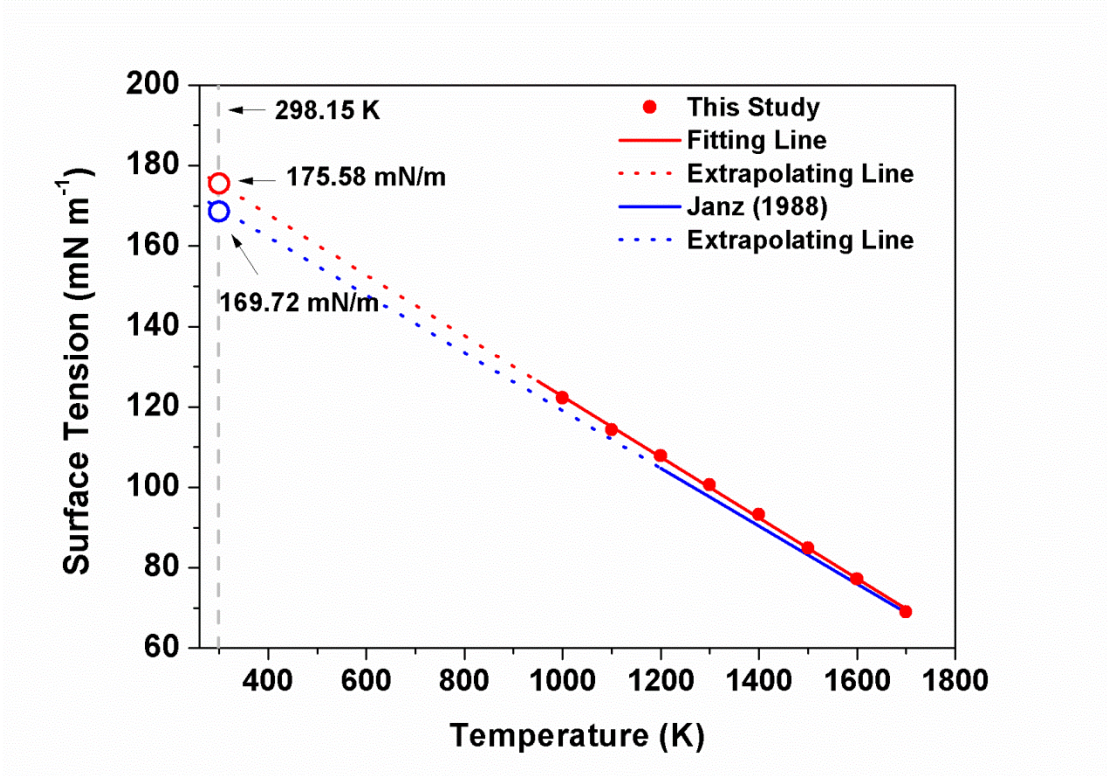

Figure 5. The surface tension of molten NaCl at different temperatures. The equation in Janz's study (1988) is $\sigma_{NaCl} = -0.07188 \cdot \mathrm{T} + 191$ (blue solid line). The fitting line based on our data is $\sigma_{NaCl} = -0.0755 \cdot \mathrm{T} + 198.09$ (red solid line). The red and blue open circles represent the extrapolated value of surface tension in simulation and reality.

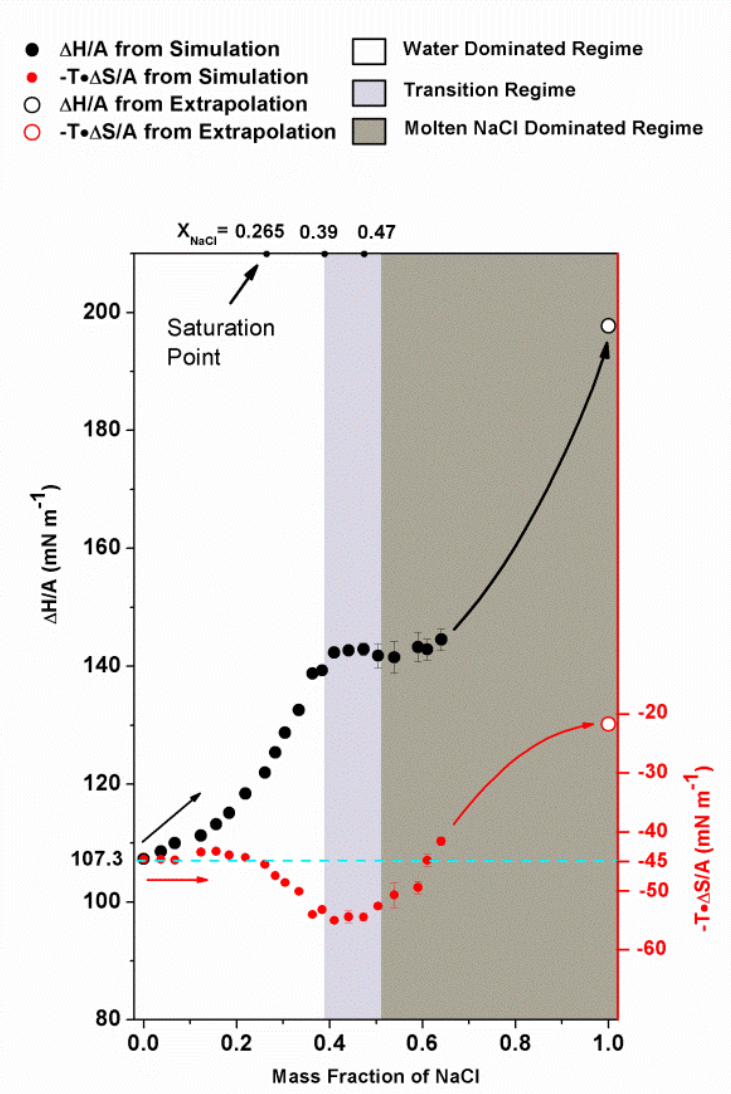

Figure 6. The excess surface enthalpy and entropy per unit area ($\frac{\Delta H}{A}$ and $\frac{T \cdot \Delta S}{A}$) of different NaCl solution concentrations. $\frac{\Delta H}{A}$ (black circles) and $-\frac{T \cdot \Delta S}{A}$ (red circles) are shown as a function of mass fraction of NaCl. The solid circles are obtained from simulation directly, and the open circles are obtained from the extrapolation of corresponding properties of molten NaCl. The cyan dashed line is only an auxiliary line for clearer view. Shaded areas are the same as in Figure 4.

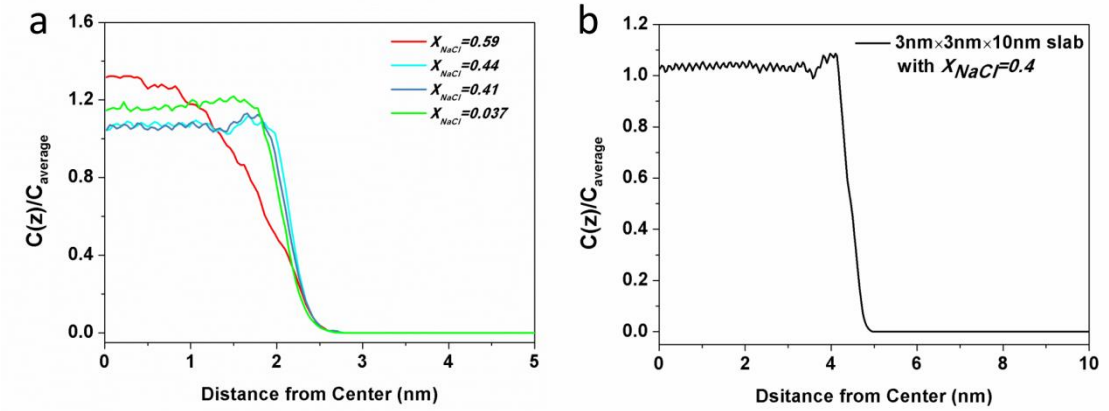

Figure 7. The ratio of Na^+ concentration at different positions (C_z) to the average concentration of the whole system ($C_{average}$). (a) The solution with x_{NaCl} = 0.59 (red line) is on behalf of the solution in the molten NaCl-dominated regime (red line), the solution x_{NaCl} = 0.44 and 0.41 (blue lines) represent the solution in transition regime, and the solution x_{NaCl} = 0.037 (green line) represents the solution in the water-dominated regime. (b) The density profile obtained from a 3 nm × 3 nm × 10 nm solution slab in which NaCl mass fraction is about 0.4.

Supplementary Information

There are three ways to calculate the excess surface entropy, i.e. the direct method, the numerical derivative and the derivative of temperature-surface tension ($T-\sigma$) relation (Sega and Dellago, 2017; Sega et al., 2018). The direct method was employed to calculate $\frac{\Delta H}{A}$ and $\frac{T\cdot\Delta S}{A}$ in our paper (Fig. 6). In this method, we simulated liquid layers with and without surfaces. The difference of enthalpy per area of liquid with surfaces and the one of liquid without surfaces is the excess surface enthalpy ($\frac{\Delta H}{A}$). And $\frac{T\cdot\Delta S}{A}$ can be calculated as $\frac{T\cdot\Delta S}{A}=\frac{\Delta H}{A}-\sigma$. The numerical derivative method is based on the value of σ of the studied liquid at different temperatures. We need to use the equation $\sigma(T)=\sigma(T_0)+a\times(T-T_0)+b\times(T-T_0)^2$ to fit the data of $\sigma(T_0)$, $\sigma(T_0-10\ K)$ and $\sigma(T_0+10\ K)$ to get the fitting parameters a and b for a given T_0, i.e., $a(T_0)$ and $b(T_0)$, respectively. As $\frac{\Delta S(T)}{A}=\frac{-d\sigma(T)}{dT}$ (Landau and Lifshitz, 1969), we have $\frac{\Delta S}{A}(T_0)=-a(T_0)$. And we can get $\frac{\Delta S}{A}$ at different temperature one by one. For $\frac{\Delta H}{A}$, we can calculate by $\frac{\Delta H}{A}=\sigma+\frac{T\cdot\Delta S}{A}$. The derivative of $T-\sigma$ relation method is also based on the value of σ of at different temperatures. After obtaining these values, we can get an equation to describe the relationship between σ and T, i.e. $\sigma(T)$. After that the excess surface entropy can be easily calculated by $\frac{\Delta S(T)}{A}=\frac{-d\sigma(T)}{dT}$ (Landau and Lifshitz, 1969). And similarly, $\frac{\Delta H}{A}=\sigma+\frac{T\cdot\Delta S}{A}$.

A very recent paper (Sega et al., 2018) compared excess surface entropy based on these methods and reported that results based on the direct method might not be applicable at high temperature because of its significant deviations to the excess surface entropy derived with the derivative of $T-\sigma$ relation when the temperature is high. Thus we used the derivative of $T-\sigma$ relation method to calculate $\frac{\Delta H}{A}$ and $\frac{T\cdot\Delta S}{A}$ of molten NaCl, but not the direct method. Note again that the majority of data in Fig. 6 (except the points for x_{NaCl} of 1.0) are obtained by the direct method at 298.15 K. We also performed independent calculation of the excess surface entropy and enthalpy of pure water at temperatures from 278.15 K to 348.15 K based on the aforementioned three methods. As shown in the Fig. S1, results from these three methods well agree with each other, which means that results based on the direct method at room temperature can be trusted.

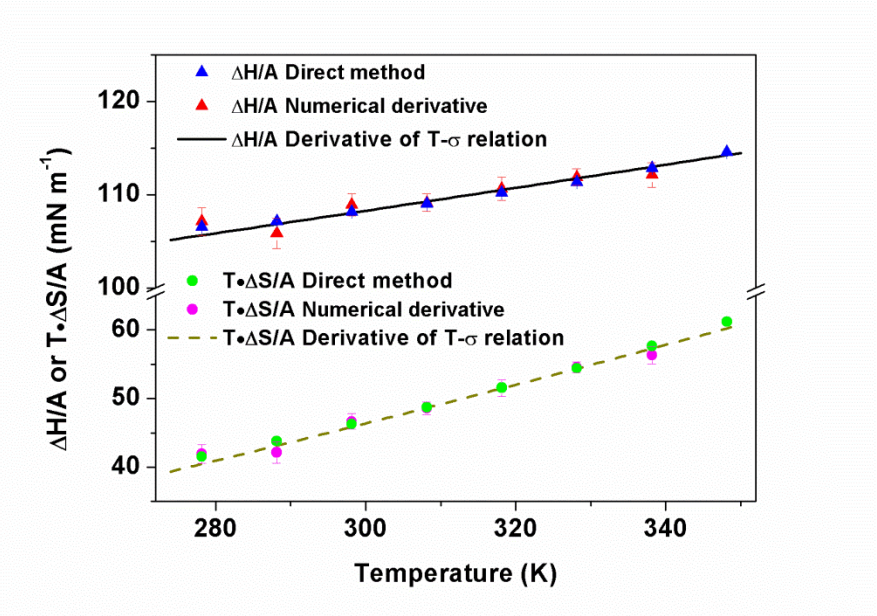

Figure S1. $\frac{\Delta H}{A}$ and $\frac{T \cdot \Delta S}{A}$ of pure water at temperatures from 278.15 K to 348.15 K obtained from different methods. ”

5. Conclusions and Outlook

In this thesis, the nano-size effect on the solubility of the NaCl nanocrystal, succinic acid solvation in water nanodroplets, the concentration dependent surface tension of the NaCl solutions are presented based on the MD simulation and corresponding thermodynamic analysis, respectively.

In the first study, a significant size effect on the solubility of NaCl nanoparticles is observed. Combining the Ostwald-Freundlich equation and Gibbs-Duhem equation with size-dependent solid-liquid surface tension yields a good prediction of the size dependence of the solubility. In addition, the distribution of ions and water in saturated nanodroplets is found to be inhomogeneous. There is a higher concentration of NaCl in the inner part than at the surface of the nanodroplet. Moreover, the structural similarity between the dissolved and molten ions grows as the size decreases, which indicate the similarity of the size effect on dissolution and melting processes. Chemical potential analysis indicates the similarity as well and further shows that NaCl nanoparticles contains equal to or less than 7 pairs of NaCl ions at 300 K in the molten state, which can be thought as the dissolved NaCl with infinite solubility. In short, this study provides insight into the size effect association between dissolution and melting processes, which may be useful to future explorations of nanoparticles in many different fields including atmospheric science, material science, and chemical engineering. However, the driving force for the size-dependent solubility of NaCl nanodroplets and corresponding structures is still not clear. Therefore, in the future, the potential of mean forces of Na^+, Cl^- ions, and water molecules in the saturated nanodroplets will be presented to explore the driving forces of size effects and inhomogeneous structures of nanoparticles. The potential of mean forces of ions and water molecules in three-phase or more multi-phase environmental systems will be also analyzed to further help understand the mechanism of size effect on the phase separation.

In the second study, the nanodroplet has a stronger surface preference for the succinic acid molecule than the same size slab, and the preference increases as the droplet size decreases, owing to the curvature effect. In addition, by comparing the energy curves of succinic acid molecule in water droplets for radii from 1 to 4 nm, it shows that the opposite size-dependent solvation of succinic acid in the internal bulk volume and surface volume of water droplets. That is, when the water droplet size decreases, the surface enrichment of succinic acid increases, but the solubility in the

internal volume decreases. At the same time, the ratio of the surface to the internal volume increases dramatically, and for water droplets with a radius of 1 nm, the internal volume is close to zero for the succinic acid molecule. Further energetic analysis shows that the surface propensity of succinic acid is primarily an enthalpic effect in all simulated cases, while the entropic effect further enhances the surface propensity when the droplet size decreases. This study indicates that the properties for organic compounds in the aqueous nanodroplets can deviate fundamentally from predictions based on bulk solution properties, which should be considered in the prediction of aerosol phase transition. Nevertheless, neither the inorganic compounds effect nor the ionization and concentration of organics are taken into consideration in this study. Therefore, in future studies, the energy profiles of organic compounds in water droplets of different sizes before and after ionization will be analyzed as a supplement. The concentration effect of organic and inorganic compounds for the size-dependent solvation will also be considered.

In the third study, the analysis based on the calculated surface tension confirms the basic concept of the Dutcher et al. (2010) semi-empirical model, while unfold a more detailed global landscape of concentration dependence of surface tension of aqueous NaCl solution and its driving forces. In the further work, this study can connect with the first study in this thesis to investigate the equilibrium between NaCl nanodroplets and water vapor with considering the size-dependent and concentration-dependent surface tension.

A. List of Publications

Peer-Reviewed publications

1. Chen, C., Wang, X., Binder, K., Ghahremanpour, M. M., van der Spoel, D., Pöschl, U., Su, H., and Cheng, Y.: Energetic analysis of succinic acid in water droplets: insight into the size-dependent solubility of atmospheric nanoparticles, Atmospheric Chemistry and Physics Discussions, 1-19, 2021.

2. Chen, C., Wang, X., Binder, K., Pöschl, U., Su, H., Cheng, Y.: Size-dependent solubility of NaCl nanocrystal in aqueous droplet (to be submitted).

3. Wang, X., Binder, K., Chen, C., Koop, T., Pöschl, U., Su, H., and Cheng, Y.: Second inflection point of water surface tension in the deeply supercooled regime revealed by entropy anomaly and surface structure using molecular dynamics simulations, Phys. Chem. Chem. Phys., 21, 3360-3369, 2019.

4. Wang, X., Chen, C., Binder, K., Kuhn, U., Pöschl, U., Su, H., and Cheng, Y.: Molecular dynamics simulation of the surface tension of aqueous sodium chloride: from dilute to highly supersaturated solutions and molten salt, Atmos. Chem. Phys., 18, 17077-17086, 10.5194/acp-18-17077-2018, 2018.

5. Wang, X., Chen, C., Binder, K., Pöschl, U., Su, H., Cheng, Y.: Studying the vapor pressure and surface tension of water nano-droplets by MD simulations (to be submitted).

6. Wang, S., Su, H., Chen, C., Tao, W., Streets, D. G., Lu, Z., Zheng, B., Carmichael, G. R., Lelieveld, J., Pöschl, U., and Cheng, Y.: Natural gas shortages during the "coal-to-gas" transition in China have caused a large redistribution of air pollution in winter 2017, P. Natl. Acad, Sci., 117, 31018-31025, 10.1073/pnas.2007513117, 2020.

Presentations

1. Chen, C., Wang, X., Binder, K., Ghahremanpour, M. M., van der Spoel, D., Pöschl, U., Su, H., and Cheng, Y.: Energetic analysis of succinic acid in water droplets: insight into the size-dependent solubility of atmospheric nanoparticles, European Geosciences Union - EGU General Assembly, April 2021, virtual PICO presentation.

2. Chen, C., Wang, X., Binder, K., Ghahremanpour, M. M., van der Spoel, D., Pöschl, U., Su, H., and Cheng, Y.: Energetic analysis of succinic acid in water droplets: insight into the size-dependent solubility of atmospheric nanoparticles, European Aerosol Conference (EAC), September 2020, virtual PICO presentation.

3. Chen, C., Kuhn, U., Pöschl, U., Su, H., & Cheng, Y.: Elevated HONO emissions in agricultural system: model simulation by the improved DNDC model (DNDC-HONO), European Geosciences Union - EGU General Assembly, Vienna (Austria), April 8th – 13th 2018, poster presentation.

B. Curriculum Vitae

BASIC INFORMATION

Chuchu Chen

Nationality: China

Email: c.chen@mpic.de

Address: Hahn-Meitner-Weg 1, 55128 Mainz

Phone: +49 157-3114-5966

EDUCATION

PhD candidate, Max Planck Institute for Chemistry, Johannes Gutenberg-Universität Mainz and Max Planck Graduate Center (2016.01~present)

- Research topic: Nano-size effect on phase transition of atmospheric aerosol particles with molecular dynamic simulation.
- Advisor: Prof. Dr. Kurt Binder, Prof. Dr. Ulrich Pöschl, Dr. Yafang Cheng, Dr. Hang Su

M.Sc. in Atmospheric Science, Center For Earth System Science, Tsinghua University (2012.09~2015.06)

- Research topic: Spatial and temporal variability in ammonia emissions from agricultural fertilization in China
- Advisor: Prof. Dr. Qiang Zhang

B.Sc. in Geographic Information Science, School of Earth Sciences, Zhejiang University (2008.09~2012.06)

RESEARCH INTEREST

- Molecular dynamics simulation
- Size effect on phase transition of aerosol particles
- Atmospheric pollutant emissions and air quality modelling

PUBLICATIONS

- Chen, C., Wang, X., Binder, K., Ghahremanpour, M. M., van der Spoel, D., Pöschl, U., Su, H., and Cheng, Y.: Energetic analysis of succinic acid in water droplets: insight into the size-dependent solubility of atmospheric nanoparticles, Atmospheric Chemistry and Physics Discussions, 1-19, 2021.

- Wang, X., Binder, K., Chen, C., Koop, T., Pöschl, U., Su, H., and Cheng, Y.: Second inflection point of water surface tension in the deeply supercooled regime revealed by entropy anomaly and surface structure using molecular dynamics simulations, Phys. Chem. Chem. Phys., 21, 3360-3369, 2019.
- Wang, X., Chen, C., Binder, K., Kuhn, U., Pöschl, U., Su, H., and Cheng, Y.: Molecular dynamics simulation of the surface tension of aqueous sodium chloride: from dilute to highly supersaturated solutions and molten salt, Atmos. Chem. Phys., 18, 17077-17086, 10.5194/acp-18-17077-2018, 2018.
- Wang, S., Su, H., Chen, C., Tao, W., Streets, D. G., Lu, Z., Zheng, B., Carmichael, G. R., Lelieveld, J., Pöschl, U., and Cheng, Y.: Natural gas shortages during the "coal-to-gas" transition in China have caused a large redistribution of air pollution in winter 2017, P. Natl. Acad, Sci., 117, 31018-31025, 10.1073/pnas.2007513117, 2020.
- Qi, J., Zheng, B., Li, M., Yu, F., Chen, C., Liu, F., ... & He, K. (2017). A high-resolution air pollutants emission inventory in 2013 for the Beijing-Tianjin-Hebei region, China. Atmospheric Environment, 170, 156-168.

ACADEMIC ACTIVITIES

- Chen, C., Wang, X., Binder, K., Ghahremanpour, M. M., van der Spoel, D., Pöschl, U., Su, H., and Cheng, Y.: Energetic analysis of succinic acid in water droplets: insight into the size-dependent solubility of atmospheric nanoparticles, European Geosciences Union - EGU General Assembly, April 2021, virtual PICO presentation.
- Chen, C., Wang, X., Binder, K., Ghahremanpour, M. M., van der Spoel, D., Pöschl, U., Su, H., and Cheng, Y.: Energetic analysis of succinic acid in water droplets: insight into the size-dependent solubility of atmospheric nanoparticles, European Aerosol Conference (EAC), September 2020, virtual PICO presentation.
- Chen, C., Kuhn, U., Pöschl, U., Su, H., & Cheng, Y.: Elevated HONO emissions in agricultural system: model simulation by the improved DNDC model (DNDC-HONO), European Geosciences Union - EGU General Assembly, Vienna (Austria), April 8th – 13th 2018, poster presentation.
- The Third Sino-European School on Atmospheric Chemistry (SESAC 2017) in Shanghai (China), Nove 21st-30th, 2017.

C. References

Abascal, J. L., and Vega, C.: A general purpose model for the condensed phases of water: TIP4P/2005, J. Chem. Phys., 123, 234505, 2005.

Abraham, M. J., Murtola, T., Schulz, R., Páll, S., Smith, J. C., Hess, B., and Lindahl, E.: GROMACS: High performance molecular simulations through multi-level parallelism from laptops to supercomputers, SoftwareX, 1, 19-25, 2015.

Alejandre, J., Tildesley, D. J., and Chapela, G. A.: Molecular dynamics simulation of the orthobaric densities and surface tension of water, J Chem Phys., 102, 4574-4583, 1995.

Altaf, M. B., and Freedman, M. A.: Effect of drying rate on aerosol particle morphology, J. Phys. Chem. Lett., 8, 3613-3618, 2017.

Ammann, M., Kalberer, M., Jost, D., Tobler, L., Rössler, E., Piguet, D., Gäggeler, H., and Baltensperger, U.: Heterogeneous production of nitrous acid on soot in polluted air masses, Nature, 395, 157-160, 1998.

Anttila, T., Kerminen, V.-M., and Lehtinen, K. E.: Parameterizing the formation rate of new particles: The effect of nuclei self-coagulation, Journal of Aerosol Science, 41, 621-636, 2010.

Aragones, J. L., Sanz, E., and Vega, C.: Solubility of NaCl in water by molecular simulation revisited, J Chem Phys, 136, 244508, 10.1063/1.4728163, 2012.

Atkins, P., De Paula, J., and Friedman, R.: Physical chemistry: quanta, matter, and change, Oxford University Press, USA, 2014.

Aveyard, R., and Saleem, S. M.: Interfacial tensions at alkane-aqueous electrolyte interfaces, J Am Chem Soc., 72, 1609-1617, 1976.

Bahadur, R., Russell, L. M., and Alavi, S.: Surface tensions in NaCl-water-air systems from MD simulations, J Phys Chem B., 111, 11989-11996, 2007.

Bahadur, R., and Russell, L. M.: Effect of Surface Tension from MD Simulations on Size-Dependent Deliquescence of NaCl Nanoparticles, Aerosol Science and Technology, 42, 369-376, 10.1080/02786820802104965, 2008a.

Bahadur, R., and Russell, L. M.: Water uptake coefficients and deliquescence of NaCl nanoparticles at atmospheric relative humidities from molecular dynamics simulations, J Chem Phys, 129, 094508, 10.1063/1.2971040, 2008b.

Barahona, D., West, R., Stier, P., Romakkaniemi, S., Kokkola, H., and Nenes, A.: Comprehensively accounting for the effect of giant CCN in cloud activation parameterizations, Atmos. Chem. Phys., 10, 2467-2473, 2010.

Beegle, B. L., Modell, M., and Reid, R. C.: Legendre transforms and their application in thermodynamics, AIChE Journal, 20, 1194-1200, 1974.

Berendsen, H., Grigera, J., and Straatsma, T.: The missing term in effective pair potentials, J. Phys. Chem., 91, 6269-6271, 1987.

Berendsen, H. J., Postma, J. P., van Gunsteren, W. F., and Hermans, J.: Interaction models for water in relation to protein hydration, in: Intermolecular forces, Springer, 331-342, 1981.

Bhatt, D., Newman, J., and Radke, C.: Molecular dynamics simulations of surface tensions of aqueous electrolytic solutions, J Phys Chem B., 108, 9077-9084, 2004.

Biskos, G., Malinowski, A., Russell, L. M., Buseck, P. R., and Martin, S. T.: Nanosize Effect on the Deliquescence and the Efflorescence of Sodium Chloride Particles, Aerosol Science and Technology, 40, 97-106, 10.1080/02786820500484396, 2006a.

Biskos, G., Paulsen, D., Russell, L., Buseck, P., and Martin, S.: Prompt deliquescence and efflorescence of aerosol nanoparticles, 2006b.

Biskos, G., Russell, L., Buseck, P., and Martin, S. T.: Nanosize effect on the hygroscopic growth factor of aerosol particles, Geophysical Research Letters, 33, 2006c.

Bluhm, H., and Siegmann, H.: Surface science with aerosols, Surface science, 603, 1969-1978, 2009.

Boucher, O., and Lohmann, U.: The sulfate-CCN-cloud albedo effect, Tellus B: Chemical and Physical Meteorology, 47, 281-300, 1995.

Burch, D., and Bazant, M. Z.: Size-dependent spinodal and miscibility gaps for intercalation in nanoparticles, Nano letters, 9, 3795-3800, 2009.

Bzdek, B. R., Power, R. M., Simpson, S. H., Reid, J. P., and Royall, C. P.: Precise, contactless measurements of the surface tension of picolitre aerosol droplets, Chem Sci., 7, 274-285, 2016.

Caleman, C., Hub, J. S., van Maaren, P. J., and van der Spoel, D.: Atomistic simulation of ion solvation in water explains surface preference of halides, P. Natl. Acad, Sci., 2011.

Cao, C., Huang, K., Shi, J., Zheng, D., Wang, W., Gu, L., and Bai, H.: Liquid-like behaviours of metallic glassy nanoparticles at room temperature, Nature communications, 10, 1-8, 2019.

Case, D. A., Darden, T., Cheatham III, T. E., Simmerling, C., Wang, J., Duke, R. E., Luo, R., Merz, K. M., Pearlman, D. A., and Crowley, M.: AMBER 9, University of California, San Francisco, 45, 2006.

Chan, C. K., Liang, Z., Zheng, J., Clegg, S. L., and Brimblecombe, P.: Thermodynamic properties of aqueous aerosols to high supersaturation: I—measurements of water activity of the system Na+− Cl−− NO− 3− SO2− 4− H2O at~ 298.15 K, Aerosol science and technology, 27, 324-344, 1997.

Chen, C., Lee, J.-G., Arakawa, K., and Mori, H.: Comparative study on size dependence of melting temperatures of pure metal and alloy nanoparticles, Applied Physics Letters, 99, 013108, 2011.

Chen, Y., Cheng, Y., Ma, N., Wolke, R., Nordmann, S., Schüttauf, S., Ran, L., Wehner, B., Birmili, W., and Gon, H. A.: Sea salt emission, transport and influence on size-segregated nitrate simulation: a case study in northwestern Europe by WRF-Chem, Atmos Chem Phys., 16, 12081-12097, 2016.

Cheng, Y., Su, H., Koop, T., Mikhailov, E., and Poschl, U.: Size dependence of phase transitions in aerosol nanoparticles, Nat Commun, 6, 5923, 10.1038/ncomms6923, 2015.

Cohen, M. D., Flagan, R. C., and Seinfeld, J. H.: Studies of concentrated electrolyte solutions using the electrodynamic balance. 3. Solute nucleation, J. Phys. Chem., 91, 4583-4590, 1987.

Couchman, P., and Jesser, W.: Thermodynamic theory of size dependence of melting temperature in metals, Nature, 269, 481-483, 1977.

Davidchack, R. L., and Laird, B. B.: Direct calculation of the crystal–melt interfacial free energies for continuous potentials: Application to the Lennard-Jones system, J Chem Phys., 118, 7651-7657, 2003.

de España, C. D., Wonaschütz, A., Steiner, G., Rosati, B., Demattio, A., Schuh, H., and Hitzenberger, R.: Long-term quantitative field study of New Particle Formation (NPF) events as a source of Cloud Condensation Nuclei (CCN) in the urban background of Vienna, Atmos. Environ., 164, 289-298, 2017.

Delogu, F.: Structural and energetic properties of unsupported Cu nanoparticles from room temperature to the melting point: Molecular dynamics simulations, Phys. Rev. B, 72, 10.1103/PhysRevB.72.205418, 2005.

Donahue, N. M., Ortega, I. K., Chuang, W., Riipinen, I., Riccobono, F., Schobesberger, S., Dommen, J., Baltensperger, U., Kulmala, M., and Worsnop, D. R.: How do organic vapors contribute to new-particle formation?, Faraday discussions, 165, 91-104, 2013.

Donaldson, D., and Vaida, V.: The influence of organic films at the air− aqueous boundary on atmospheric processes, Chemical reviews, 106, 1445-1461, 2006.

Donaldson, D., and Valsaraj, K. T.: Adsorption and reaction of trace gas-phase organic compounds on atmospheric water film surfaces: A critical review, Environ. Sci. Technol., 44, 865-873, 2010.

Dunne, E. M., Gordon, H., Kürten, A., Almeida, J., Duplissy, J., Williamson, C., Ortega, I. K., Pringle, K. J., Adamov, A., and Baltensperger, U.: Global atmospheric particle formation from CERN CLOUD measurements, Science, 354, 1119-1124, 2016.

Dutcher, C. S., Wexler, A. S., and Clegg, S. L.: Surface tensions of inorganic multicomponent aqueous electrolyte solutions and melts, J Phys Chem A., 114, 12216-12230, 2010.

Erdemir, D., Lee, A. Y., and Myerson, A. S.: Nucleation of crystals from solution: classical and two-step models, Accounts of chemical research, 42, 621-629, 2009.

Ervens, B.: Modeling the processing of aerosol and trace gases in clouds and fogs, Chemical reviews, 115, 4157-4198, 2015.

Espinosa, J. R., Young, J. M., Jiang, H., Gupta, D., Vega, C., Sanz, E., Debenedetti, P. G., and Panagiotopoulos, A. Z.: On the calculation of solubilities via direct coexistence simulations: Investigation of NaCl aqueous solutions and Lennard-Jones binary mixtures, J Chem Phys, 145, 154111, 10.1063/1.4964725, 2016.

Essmann, U., Perera, L., Berkowitz, M. L., Darden, T., Lee, H., and Pedersen, L. G.: A smooth particle mesh Ewald method, J Chem Phys., 103, 8577-8593, 1995.

Estillore, A. D., Morris, H. S., Or, V. W., Lee, H. D., Alves, M. R., Marciano, M. A., Laskina, O., Qin, Z., Tivanski, A. V., and Grassian, V. H.: Linking hygroscopicity and the surface microstructure of model inorganic salts, simple and complex carbohydrates, and authentic sea spray aerosol particles, Phys. Chem. Chem. Phys., 19, 21101-21111, 2017.

Factorovich, M. H., Molinero, V., and Scherlis, D. A.: Vapor pressure of water nanodroplets, J Am Chem Soc, 136, 4508-4514, 10.1021/ja405408n, 2014.

Fan, J., Wang, Y., Rosenfeld, D., and Liu, X.: Review of aerosol–cloud interactions: Mechanisms, significance, and challenges, Journal of the Atmospheric Sciences, 73, 4221-4252, 2016.

Finlayson-Pitts, B.: The tropospheric chemistry of sea salt: A molecular-level view of the chemistry of NaCl and NaBr, Chem Rev., 103, 4801-4822, 2003.

Finlayson-Pitts, B. J.: Reactions at surfaces in the atmosphere: integration of experiments and theory as necessary (but not necessarily sufficient) for predicting the physical chemistry of aerosols, Phys. Chem. Chem. Phys., 11, 7760-7779, 2009.

Fisher, L. R., and Israelachvili, J. N.: Experimental studies on the applicability of the Kelvin equation to highly curved concave menisci, Journal of Colloid and Interface Science, 80, 528-541, 1981.

Fischer, N. M., van Maaren, P. J., Ditz, J. C., Yildirim, A., and van der Spoel, D.: Properties of organic liquids when simulated with long-range Lennard-Jones interactions, J Chem Theory Comput., 11, 2938-2944, 2015.

Fletcher, N. H.: Size effect in heterogeneous nucleation, J. Chem. Phys., 29, 572-576, 1958.

Fountoukis, C., Riipinen, I., Denier Van Der Gon, H., Charalampidis, P., Pilinis, C., Wiedensohler, A., O'Dowd, C., Putaud, J., Moerman, M., and Pandis, S. N.: Simulating ultrafine particle formation in Europe using a regional CTM: contribution of primary emissions versus secondary formation to aerosol number concentrations, Atmos. Chem. Phys., 12, 8663-8677, 2012.

Freedman, M. A.: Phase separation in organic aerosol, Chem. Soc. Rev., 46, 7694-7705, 2017.

Frenkel, D., Smit, B., and Ratner, M. A.: Understanding molecular simulation: from algorithms to applications, Academic press San Diego, 1996.

Frenken J W M, Van der Veen J F.: Observation of surface melting, Phys Rev Lett, 54, 134-137, 1985.

Freundlich, H.: Die Bedeutung der Kapillarchemie für technische und physiologische Fragen, Angewandte Chemie, 22, 1393-1395, 1909.

Freundlich, H.: Kapillarchemie, eine Darstellung der Chemie der Kolloide und verwandter Gebiete, akademische Verlagsgesellschaft, 1922.

Fuentes-Azcatl, R., and Barbosa, M. C.: Sodium chloride, NaCl/ϵ: New force field, J. Phys. Chem. B, 120, 2460-2470, 2016.

Fuzzi, S., Andreae, M., Huebert, B., Kulmala, M., Bond, T. C., Boy, M., Doherty, S., Guenther, A., Kanakidou, M., and Kawamura, K.: Critical assessment of the current state of scientific knowledge, terminology, and research needs concerning the role of organic aerosols in the atmosphere, climate, and global change, Atmos. Chem. Phys., 6, 2017-2038, 2006.

Gao, Y., Chen, S. B., and Yu, L. E.: Efflorescence relative humidity for ammonium sulfate particles, J. Phys. Chem. A, 110, 7602-7608, 2006.

Gao, Y., Chen, S. B., and Liya, E. Y.: Efflorescence relative humidity of airborne sodium chloride particles: A theoretical investigation, Atmos. Environ., 41, 2019-2023, 2007.

Gast, A. P., and Adamson, A. W.: Physical chemistry of surfaces, Wiley New York, 1997.

Ghorai, S., Wang, B., Tivanski, A., and Laskin, A.: Hygroscopic properties of internally mixed particles composed of NaCl and water-soluble organic acids, Environ Sci Technol., 48, 2234-2241, 2014.

Goldstein, A., Echer, C., and Alivisatos, A.: Melting in semiconductor nanocrystals, Science, 256, 1425-1427, 1992.

Gordon, H., Sengupta, K., Rap, A., Duplissy, J., Frege, C., Williamson, C., Heinritzi, M., Simon, M., Yan, C., and Almeida, J.: Reduced anthropogenic aerosol radiative forcing caused by biogenic new particle formation, P. Natl. Acad, Sci., 113, 12053-12058, 2016.

Gordon, H., Kirkby, J., Baltensperger, U., Bianchi, F., Breitenlechner, M., Curtius, J., Dias, A., Dommen, J., Donahue, N. M., and Dunne, E. M.: Causes and importance of new particle formation in the present-day and preindustrial atmospheres, Journal of Geophysical Research: Atmospheres, 122, 8739-8760, 2017.

Gribb, A. A., and Banfield, J. F.: Particle size effects on transformation kinetics and phase stability in nanocrystalline TiO2, American Mineralogist, 82, 717-728, 1997.

Guo, Y., Xu, K., Wu, C., Zhao, J., and Xie, Y.: Surface chemical-modification for engineering the intrinsic physical properties of inorganic two-dimensional nanomaterials, Chem. Soc. Rev., 44, 637-646, 2015.

Harbury, L.: Solubility and Melting Point as Functions of Particle Size. 1, J. Phys. Chem., 50, 190-199, 1946.

Harkins, W. D., and Brown, F.: The determination of surface tension (free surface energy), and the weight of falling drops: The surface tension of water and benzene by the capillary height method, J Am Chem Soc., 41, 499-524, 1919.

Hayase, S., Yabushita, A., Kawasaki, M., Enami, S., Hoffmann, M. R., and Colussi, A. J.: Weak acids enhance halogen activation on atmospheric water's surfaces, J. Phys. Chem. A, 115, 4935-4940, 2011.

Hess, B., Bekker, H., Berendsen, H. J., and Fraaije, J. G.: LINCS: a linear constraint solver for molecular simulations, Journal of computational chemistry, 18, 1463-1472, 1997.

Hess, B., van der Spoel, L. E., and Lindahl, E.: GROMACS Groningen Machine for Chemical Simulations, User Manual. Version, 4, 2010.

Hinds, W. C.: Aerosol technology: properties, behavior, and measurement of airborne particles, John Wiley & Sons, 1999.

Hoover, W.G.: Canonical dynamics: equilibrium phase-space distributions, Phys Rev A., 31(3), 1695, 1985.

Hub, J. S., De Groot, B. L., and Van Der Spoel, D.: g_wham A Free Weighted Histogram Analysis Implementation Including Robust Error and Autocorrelation Estimates, J. Chem. Theory. Comput., 6, 3713-3720, 2010.

Hub, J. S., Caleman, C., and van der Spoel, D.: Organic molecules on the surface of water droplets--an energetic perspective, Phys Chem Chem Phys, 14, 9537-9545, 10.1039/c2cp40483d, 2012.

Hub, J. S., Wolf, M. G., Caleman, C., van Maaren, P. J., Groenhof, G., and van der Spoel, D.: Thermodynamics of hydronium and hydroxide surface solvation, Chemical Science, 5, 10.1039/c3sc52862f, 2014.

Hyvärinen, A.-P., Lihavainen, H., Gaman, A., Vairila, L., Ojala, H., Kulmala, M., and Viisanen, Y.: Surface Tensions and Densities of Oxalic, Malonic, Succinic, Maleic, Malic, andcis-Pinonic Acids, Journal of Chemical & Engineering Data, 51, 255-260, 10.1021/je050366x, 2006.

Ismail, A. E., Grest, G. S., and Stevens, M. J.: Capillary waves at the liquid-vapor interface and the surface tension of water, J. Chem. Phys., 125, 014702, 2006.

Janz, G. J.: Thermodynamic and transport properties for molten salts: correlation equations for critically evaluated density, surface tension, electrical conductance, and viscosity data, Amer Inst of Phys., 1988.

Jarvis, N. L., and Scheiman, M. A.: Surface potentials of aqueous electrolyte solutions, J Phys Chem., 72, 74-78, 1968.

Jeevanandam, J., Barhoum, A., Chan, Y. S., Dufresne, A., and Danquah, M. K.: Review on nanoparticles and nanostructured materials: history, sources, toxicity and regulations, Beilstein journal of nanotechnology, 9, 1050-1074, 2018.

Ji, C., Gao, Q., Dong, X., Yin, W., Gu, Z., Gan, Z., Zhao, Y., and Yin, M.: A Size-Reducible Nanodrug with an Aggregation-Enhanced Photodynamic Effect for Deep Chemo-Photodynamic Therapy, Angewandte Chemie International Edition, 57, 11384-11388, 2018.

Jiang, H., Debenedetti, P. G., and Panagiotopoulos, A. Z.: Nucleation in aqueous NaCl solutions shifts from 1-step to 2-step mechanism on crossing the spinodal, J Chem Phys, 150, 124502, 10.1063/1.5084248, 2019.

Jiang, Q., and Yang, C.: Size effect on the phase stability of nanostructures, Current nanoscience, 4, 179-200, 2008.

Johansson, K., and Eriksson, J. C.: γ and $d\gamma/dT$ measurements on aqueous solutions of 1, 1-electrolytes, J Colloid Interf Sci., 49, 469-480, 1974.

Johnson, C. A.: Generalization of the Gibbs-Thomson equation, Surface Science, 3, 429-444, 1965.

Jorgensen, W. L., Chandrasekhar, J., Madura, J. D., Impey, R. W., and Klein, M. L.: Comparison of simple potential functions for simulating liquid water, J. Chem. Phys., 79, 926-935, 1983.

Joung, I. S., and Cheatham III, T. E.: Determination of alkali and halide monovalent ion parameters for use in explicitly solvated biomolecular simulations, J. Phys. Chem. B, 112, 9020-9041, 2008.

Joung, I. S., and Cheatham III, T. E.: Molecular dynamics simulations of the dynamic and energetic properties of alkali and halide ions using water-model-specific ion parameters, J Phys Chem B., 113, 13279-13290, 2009.

Jungwirth P, and Tobias D J.: Surface effects on aqueous ionic solvation: A molecular dynamics simulation study of NaCl at the air/water interface from infinite dilution to saturation[J]. The Journal of Physical Chemistry B, 2000, 104(32): 7702-7706.

Kaptay, G.: On the size and shape dependence of the solubility of nano-particles in solutions, Int J Pharm, 430, 253-257, 10.1016/j.ijpharm.2012.03.038, 2012.

Kerminen, V.-M., Chen, X., Vakkari, V., Petäjä, T., Kulmala, M., and Bianchi, F.: Atmospheric new particle formation and growth: review of field observations, Environmental Research Letters, 13, 103003, 2018.

Kirkby, J., Curtius, J., Almeida, J., Dunne, E., Duplissy, J., Ehrhart, S., Franchin, A., Gagné, S., Ickes, L., and Kürten, A.: Role of sulphuric acid, ammonia and galactic cosmic rays in atmospheric aerosol nucleation, Nature, 476, 429-433, 2011.

Kirkwood, J. G.: Statistical mechanics of fluid mixtures, J. Chem. Phys., 3, 300-313, 1935.

Koop, T., Bookhold, J., Shiraiwa, M., and Pöschl, U.: Glass transition and phase state of organic compounds: dependency on molecular properties and implications for secondary organic aerosols in the atmosphere, Phys. Chem. Chem. Phys., 13, 19238-19255, 2011.

Korhonen, H., Lehtinen, K. E., and Kulmala, M.: Multicomponent aerosol dynamics model UHMA: model development and validation, Atmos. Chem. Phys., 4, 757-771, 2004.

Krieger, U. K., Marcolli, C., and Reid, J. P.: Exploring the complexity of aerosol particle properties and processes using single particle techniques, Chem. Soc. Rev., 41, 6631-6662, 2012.

Kroll, J. H., Donahue, N. M., Jimenez, J. L., Kessler, S. H., Canagaratna, M. R., Wilson, K. R., Altieri, K. E., Mazzoleni, L. R., Wozniak, A. S., and Bluhm, H.: Carbon oxidation state as a metric for describing the chemistry of atmospheric organic aerosol, Nature chemistry, 3, 133-139, 2011.

Kuang, C., McMurry, P., and McCormick, A.: Determination of cloud condensation nuclei production from measured new particle formation events, Geophysical Research Letters, 36, 2009.

Kuang, C., Chen, M., McMurry, P. H., and Wang, J.: Modification of laminar flow ultrafine condensation particle counters for the enhanced detection of 1 nm condensation nuclei, Aerosol Science and Technology, 46, 309-315, 2012.

Kuhn, T., Earle, M., Khalizov, A., and Sloan, J.: Size dependence of volume and surface nucleation rates for homogeneous freezing of supercooled water droplets, Atmos. Chem. Phys., 11, 2853-2861, 2011.

Kulmala, M., Vehkamäki, H., Petäjä, T., Dal Maso, M., Lauri, A., Kerminen, V. M., Birmili, W., and McMurry, P. H.: Formation and growth rates of ultrafine atmospheric

particles: a review of observations, Journal of Aerosol Science, 35, 143-176, 10.1016/j.jaerosci.2003.10.003, 2004.

Kulmala, M., Kontkanen, J., Junninen, H., Lehtipalo, K., Manninen, H. E., Nieminen, T., Petaja, T., Sipila, M., Schobesberger, S., Rantala, P., Franchin, A., Jokinen, T., Jarvinen, E., Aijala, M., Kangasluoma, J., Hakala, J., Aalto, P. P., Paasonen, P., Mikkila, J., Vanhanen, J., Aalto, J., Hakola, H., Makkonen, U., Ruuskanen, T., Mauldin, R. L., 3rd, Duplissy, J., Vehkamaki, H., Back, J., Kortelainen, A., Riipinen, I., Kurten, T., Johnston, M. V., Smith, J. N., Ehn, M., Mentel, T. F., Lehtinen, K. E., Laaksonen, A., Kerminen, V. M., and Worsnop, D. R.: Direct observations of atmospheric aerosol nucleation, Science, 339, 943-946, 10.1126/science.1227385, 2013.

Kumar, A.: Aqueous guanidinium salts: Part II. Isopiestic osmotic coefficients of guanidinium sulphate and viscosity and surface tension of guanidinium chloride, bromide, acetate, perchlorate and sulphate solutions at 298.15 K, Fluid Phase Equilibr., 180, 195-204, 2001.

Kumar, S., Rosenberg, J. M., Bouzida, D., Swendsen, R. H., and Kollman, P. A.: Multidimensional free-energy calculations using the weighted histogram analysis method, Journal of Computational Chemistry, 16, 1339-1350, 1995.

Laakso, L., Merikanto, J., Vakkari, V., Laakso, H., Kulmala, M., Molefe, M., Kgabi, N., Mabaso, D., Carslaw, K., and Spracklen, D.: Boundary layer nucleation as a source of new CCN in savannah environment, Atmos. Chem. Phys., 13, 1957-1972, 2013.

Lanaro, G., and Patey, G. N.: Molecular dynamics simulation of NaCl dissolution, J Phys Chem B, 119, 4275-4283, 10.1021/jp512358s, 2015.

Lanaro, G., and Patey, G. N.: Birth of NaCl Crystals: Insights from Molecular Simulations, J Phys Chem B, 120, 9076-9087, 10.1021/acs.jpcb.6b05291, 2016.

Landau, L. D., and Lifshitz, E. M.: Statistical physics, Pergamon press, 1969.

Lei, T., Ma, N., Hong, J., Tuch, T., Wang, X., Wang, Z., Pöhlker, M., Ge, M., Wang, W., and Mikhailov, E.: Nano-hygroscopicity tandem differential mobility analyzer (nano-HTDMA) for investigating hygroscopic properties of sub-10 nm aerosol nanoparticles, Atmospheric Measurement Techniques, 13, 5551-5567, 2020.

Letellier, P., Mayaffre, A., and Turmine, M.: Solubility of nanoparticles: nonextensive thermodynamics approach, Journal of Physics: Condensed Matter, 19, 436229, 2007.

Levin, Y., and Flores-Mena, J.: Surface tension of strong electrolytes, EPL, 56, 187, 2001.

Lewis, E. R., and Schwartz, S. E.: Sea salt aerosol production: mechanisms, methods, measurements, and models-A critical review, American Geophysical Union, 2004.

Li, Q.-J., Küçükbenli, E., Lam, S., Khaykovich, B., Kaxiras, E., and Li, J.: Development of robust neural-network interatomic potential for molten salt, Cell Reports Physical Science, 2, 100359, 2021.

Li, T., Donadio, D., and Galli, G.: Ice nucleation at the nanoscale probes no man's land of water, Nature communications, 4, 1-6, 2013.

Li, Z.-B., Li, Y.-G., and Lu, J.-F.: Surface tension model for concentrated electrolyte aqueous solutions by the Pitzer equation, Ind Eng Chem Res., 38, 1133-1139, 1999.

Li, Z., and Lu, B. C.-Y.: Surface tension of aqueous electrolyte solutions at high concentrations—representation and prediction, Chem Eng Sci., 56, 2879-2888, 2001.

Li, Z., Rosenfeld, D., and Fan, J.: Aerosols and their impact on radiation, clouds, precipitation, and severe weather events, in: Oxford Research Encyclopedia of Environmental Science, 2017.

Lide, D. R.: CRC handbook of chemistry and physics, CRC press, 2004.

Lihavainen, H., Kerminen, V. M., Komppula, M., Hatakka, J., Aaltonen, V., Kulmala, M., and Viisanen, Y.: Production of "potential" cloud condensation nuclei associated with atmospheric new-particle formation in northern Finland, Journal of Geophysical Research: Atmospheres, 108, 2003.

Lü, Y., Zhang, X., and Chen, M.: Size Effect on nucleation rate for homogeneous crystallization of nanoscale water film, J. Phys. Chem. B, 117, 10241-10249, 2013.

Manka, A., Pathak, H., Tanimura, S., Wölk, J., Strey, R., and Wyslouzil, B. E.: Freezing water in no-man's land, Phys. Chem. Chem. Phys., 14, 4505-4516, 2012.

Martins-Costa, M. T., Anglada, J. M., Francisco, J. S., and Ruiz-Lopez, M. F.: Reactivity of atmospherically relevant small radicals at the air–water interface, Angewandte Chemie International Edition, 51, 5413-5417, 2012.

Martin, S. T.: Phase transitions of aqueous atmospheric particles, Chem Rev., 100, 3403-3454, 2000.

Matsumoto, K., Tanaka, H., Nagao, I., and Ishizaka, Y.: Contribution of particulate sulfate and organic carbon to cloud condensation nuclei in the marine atmosphere, Geophysical Research Letters, 24, 655-658, 1997.

Matubayasi, N., Tsunetomo, K., Sato, I., Akizuki, R., Morishita, T., Matuzawa, A., and Natsukari, Y.: Thermodynamic quantities of surface formation of aqueous electrolyte

solutions: IV. Sodium halides, anion mixtures, and sea water, J Colloid Interf Sci., 243, 444-456, 2001.

Mauritsen, T., Sedlar, J., Tjernström, M., Leck, C., Martin, M., Shupe, M., Sjogren, S., Sierau, B., Persson, P., and Brooks, I.: An Arctic CCN-limited cloud-aerosol regime, Atmos. Chem. Phys., 11, 165-173, 2011.

McCoy, B. J.: A new population balance model for crystal size distributions: Reversible, size-dependent growth and dissolution, Journal of colloid and interface science, 240, 139-149, 2001.

McHale, J., Auroux, A., Perrotta, A., and Navrotsky, A.: Surface energies and thermodynamic phase stability in nanocrystalline aluminas, Science, 277, 788-791, 1997.

Menzl, G., Gonzalez, M. A., Geiger, P., Caupin, F., Abascal, J. L., Valeriani, C., and Dellago, C.: Molecular mechanism for cavitation in water under tension, P. Natl. Acad, Sci., 113, 13582-13587, 2016.

Merikanto, J., Spracklen, D., Mann, G., Pickering, S., and Carslaw, K.: Impact of nucleation on global CCN, Atmos. Chem. Phys., 9, 8601-8616, 2009.

Mester Z., Panagiotopoulos A Z.. Mean ionic activity coefficients in aqueous NaCl solutions from molecular dynamics simulations, J Chem Phys., 142(4), 044507, 2015.

Metzger, A., Verheggen, B., Dommen, J., Duplissy, J., Prevot, A. S., Weingartner, E., Riipinen, I., Kulmala, M., Spracklen, D. V., and Carslaw, K. S.: Evidence for the role of organics in aerosol particle formation under atmospheric conditions, P. Natl. Acad, Sci., 107, 6646-6651, 2010.

Mikhailov, E., Vlasenko, S., Martin, S. T., Koop, T., and Pöschl, U.: Amorphous and crystalline aerosol particles interacting with water vapor: conceptual framework and experimental evidence for restructuring, phase transitions and kinetic limitations, Atmos. Chem. Phys., 9, 9491-9522, 10.5194/acp-9-9491-2009, 2009.

Miyamoto, S., and Kollman, P. A.: Settle: An analytical version of the SHAKE and RATTLE algorithm for rigid water models, Journal of computational chemistry, 13, 952-962, 1992.

Monge, M. E., Rosenørn, T., Favez, O., Müller, M., Adler, G., Riziq, A. A., Rudich, Y., Herrmann, H., George, C., and D'Anna, B.: Alternative pathway for atmospheric particles growth, P. Natl. Acad, Sci., 109, 6840-6844, 2012.

Morris, H. S., Grassian, V. H., and Tivanski, A. V.: Humidity-dependent surface tension measurements of individual inorganic and organic submicrometre liquid particles, Chem Sci., 6, 3242-3247, 2015.

Moucka, F., Nezbeda, I., and Smith, W. R.: Molecular force fields for aqueous electrolytes: SPC/E-compatible charged LJ sphere models and their limitations, J Chem Phys, 138, 154102, 10.1063/1.4801322, 2013.

Mudunkotuwa, I. A., Rupasinghe, T., Wu, C.-M., and Grassian, V. H.: Dissolution of ZnO nanoparticles at circumneutral pH: a study of size effects in the presence and absence of citric acid, Langmuir, 28, 396-403, 2012.

Müller, R. H., and Peters, K.: Nanosuspensions for the formulation of poorly soluble drugs: I. Preparation by a size-reduction technique, International journal of pharmaceutics, 160, 229-237, 1998.

Müller, R. H., Jacobs, C., and Kayser, O.: Nanosuspensions as particulate drug formulations in therapy: rationale for development and what we can expect for the future, Advanced drug delivery reviews, 47, 3-19, 2001.

Neumann, R. M.: Entropic approach to Brownian movement, Am. J. Phys., 48, 354-357, 10.1119/1.12095, 1980.

Neyt, J.-C., Wender, A., Lachet, V., Ghoufi, A., and Malfreyt, P.: Prediction of the concentration dependence of the surface tension and density of salt solutions: atomistic simulations using Drude oscillator polarizable and nonpolarizable models, Phys Chem Chem Phys., 15, 11679-11690, 2013.

Nezbeda I., Moučka F., and Smith W R.: Recent progress in molecular simulation of aqueous electrolytes: Force fields, chemical potentials and solubility, Mol Phys., 114(11), 1665-1690, 2016.

Nosé, S.: A molecular dynamics method for simulations in the canonical ensemble, Mol Phys., 52(2), 255-268, 1984.

Ostwald, W.: Über die vermeintliche Isomerie des roten und gelben Quecksilberoxyds und die Oberflächenspannung fester Körper, Zeitschrift für physikalische Chemie, 34, 495-503, 1900.

Pan, D., Liu, L.-M., Slater, B., Michaelides, A., and Wang, E.: Melting the ice: on the relation between melting temperature and size for nanoscale ice crystals, ACS nano, 5, 4562-4569, 2011.

Pathak, H., Obeidat, A., Wilemski, G., and Wyslouzil, B.: The structure of D2O-nonane nanodroplets, J. Chem. Phys., 140, 224318, 2014.

Patrov, B.: Surface tension of Na, K//Cl, SO 4 and Li, K//Cl, NO 3 mutual system melts, Zhurnal Prikladnoj Khimii, 70, 1900-1902, 1997.

Pegram, L. M., and Record, M. T.: Partitioning of atmospherically relevant ions between bulk water and the water/vapor interface, P Natl Acad Sci USA., 103, 14278-14281, 2006.

Pegram, L. M., and Record, M. T.: Hofmeister salt effects on surface tension arise from partitioning of anions and cations between bulk water and the air-water interface, J Phys Chem B., 111, 5411-5417, 2007.

Perez, M.: Gibbs–Thomson effects in phase transformations, Scripta materialia, 52, 709-712, 2005.

Pierce, J., and Adams, P.: Can cosmic rays affect cloud condensation nuclei by altering new particle formation rates?, Geophysical Research Letters, 36, 2009.

Pöschl, U.: Atmospheric aerosols: composition, transformation, climate and health effects, Angewandte Chemie International Edition, 44, 7520-7540, 2005.

Pöschl, U., and Shiraiwa, M.: Multiphase chemistry at the atmosphere–biosphere interface influencing climate and public health in the anthropocene, Chemical reviews, 115, 4440-4475, 2015.

Prestipino, S., Laio, A., and Tosatti, E.: Shape and area fluctuation effects on nucleation theory, J. Chem. Phys., 140, 094501, 2014.

Pye, H. O., Nenes, A., Alexander, B., Ault, A. P., Barth, M. C., Clegg, S. L., Collett Jr, J. L., Fahey, K. M., Hennigan, C. J., and Herrmann, H.: The acidity of atmospheric particles and clouds, Atmos. Chem. Phys., 20, 4809-4888, 2020.

Qi, Y., Çağin, T., Johnson, W. L., and Goddard III, W. A.: Melting and crystallization in Ni nanoclusters: The mesoscale regime, J. Chem. Phys., 115, 385-394, 2001.

Qin, S.-Y., Cheng, Y.-J., Jiang, Z.-W., Ma, Y.-H., and Zhang, A.-Q.: Morphology control of self-deliverable nanodrug with enhanced anticancer efficiency, Colloids and Surfaces B: Biointerfaces, 165, 345-354, 2018.

Qiu, L., Chen, T., Öçsoy, I., Yasun, E., Wu, C., Zhu, G., You, M., Han, D., Jiang, J., and Yu, R.: A cell-targeted, size-photocontrollable, nuclear-uptake nanodrug delivery system for drug-resistant cancer therapy, Nano letters, 15, 457-463, 2015.

Rabinow, B. E.: Nanosuspensions in drug delivery, Nature reviews Drug discovery, 3, 785-796, 2004.

Reddington, C. L., Carslaw, K. S., Spracklen, D. V., Frontoso, M. G., Collins, L., Merikanto, J., Minikin, A., Hamburger, T., Coe, H., and Kulmala, M.: Primary versus

secondary contributions to particle number concentrations in the European boundary layer, Atmos. Chem. Phys., 11, 12007-12036, 2011.

Richardson, C., and Snyder, T. D.: A study of heterogeneous nucleation in aqueous solutions, Langmuir, 10, 2462-2465, 1994.

Rickards, A. M., Miles, R. E., Davies, J. F., Marshall, F. H., and Reid, J. P.: Measurements of the sensitivity of aerosol hygroscopicity and the κ parameter to the O/C ratio, J. Phys. Chem. A, 117, 14120-14131, 2013.

Riipinen, I., Yli-Juuti, T., Pierce, J. R., Petäjä, T., Worsnop, D. R., Kulmala, M., and Donahue, N. M.: The contribution of organics to atmospheric nanoparticle growth, Nature Geoscience, 5, 453-458, 10.1038/ngeo1499, 2012.

Rivest, J. B., Fong, L.-K., Jain, P. K., Toney, M. F., and Alivisatos, A. P.: Size dependence of a temperature-induced solid–solid phase transition in copper (I) sulfide, J. Phys. Chem. Lett., 2, 2402-2406, 2011.

Roeselová, M., Vieceli, J., Dang, L. X., Garrett, B. C., and Tobias, D. J.: Hydroxyl radical at the air− water interface, J. Am. Chem. Soc., 126, 16308-16309, 2004.

Rose, C., Sellegri, K., Moreno, I., Velarde, F., Ramonet, M., Weinhold, K., Krejci, R., Andrade, M., Wiedensohler, A., and Ginot, P.: CCN production by new particle formation in the free troposphere, Atmos. Chem. Phys., 17, 1529-1541, 2017.

Rosenfeld, D., Sherwood, S., Wood, R., and Donner, L.: Climate effects of aerosol-cloud interactions, Science, 343, 379-380, 2014.

Rudich, Y.: Laboratory perspectives on the chemical transformations of organic matter in atmospheric particles, Chemical Reviews, 103, 5097-5124, 2003.

Rudich, Y., Donahue, N. M., and Mentel, T. F.: Aging of organic aerosol: Bridging the gap between laboratory and field studies, Annu. Rev. Phys. Chem., 58, 321-352, 2007.

Sander, R.: Compilation of Henry's law constants for inorganic and organic species of potential importance in environmental chemistry, in, Citeseer, 1999.

Sander, R.: Compilation of Henry's law constants (version 4.0) for water as solvent, Atmos. Chem. Phys., 15, 4399-4981, 10.5194/acp-15-4399-2015, 2015.

Sayou, M., Ishizuka, R., and Matubayasi, N.: Energetic Analysis of Adsorption and Absorption of Small Molecule to Nanodroplet of Water, J. Phys. Chem. B, 121, 5995-6001, 2017.

Sega, M., and Dellago, C.: Long-range dispersion effects on the water/vapor interface simulated using the most common models. J. Phys. Chem. B, 121(15), 3798-3803, 2017.

Sega, M., Horvai, G., and Jedlovszky, P.: On the calculation of the surface entropy in computer simulation. J. Mol. Liq., 262, 58-62, 2018.

Seinfeld, J., and Pandis, S.: Chapter 2: Atmospheric Trace Constituents, Atmospheric Chemistry and Physics: From Air Pollution to Climate Change; John Wiley & Sons: Hoboken, NJ, USA, 45-46, 2016.

Seinfeld, J. H., Pandis, S. N., and Noone, K.: Atmospheric chemistry and physics: from air pollution to climate change, Physics Today, 51, 88, 1998.

Seinfeld, J. H., Bretherton, C., Carslaw, K. S., Coe, H., DeMott, P. J., Dunlea, E. J., Feingold, G., Ghan, S., Guenther, A. B., and Kahn, R.: Improving our fundamental understanding of the role of aerosol− cloud interactions in the climate system, P. Natl. Acad, Sci., 113, 5781-5790, 2016.

Shchekin, A., and Rusanov, A.: Generalization of the Gibbs–Kelvin–Köhler and Ostwald–Freundlich equations for a liquid film on a soluble nanoparticle, J. Chem. Phys., 129, 154116, 2008.

Shirts, M. R., Pitera, J. W., Swope, W. C., and Pande, V. S.: Extremely precise free energy calculations of amino acid side chain analogs: Comparison of common molecular mechanics force fields for proteins, J. Chem. Phys., 119, 5740-5761, 2003.

Souaille, M., and Roux, B.: Extension to the weighted histogram analysis method: combining umbrella sampling with free energy calculations, Computer physics communications, 135, 40-57, 2001.

Steinhardt, P. J., Nelson, D. R., and Ronchetti, M.: Bond-orientational order in liquids and glasses, Phys. Rev. B, 28, 784-805, 10.1103/PhysRevB.28.784, 1983.

Stillinger, F. H., and Weber, T. A.: Computer simulation of local order in condensed phases of silicon, Phys Rev B., 31, 5262, 1985.

Sun, J., He, L., Lo, Y.-C., Xu, T., Bi, H., Sun, L., Zhang, Z., Mao, S. X., and Li, J.: Liquid-like pseudoelasticity of sub-10-nm crystalline silver particles, Nature materials, 13, 1007-1012, 2014.

Suo, L., Hu, Y.-S., Li, H., Armand, M., and Chen, L.: A new class of solvent-in-salt electrolyte for high-energy rechargeable metallic lithium batteries, Nature communications, 4, 1-9, 2013.

Talbot, J. B.: Handbook of aqueous electrolyte solutions: physical properties, estimation and correlation methods AL Horvath, Ellis Horwood Limited, 1985, 631 p. Wiley Online Library, 1987.

Tang, I., Munkelwitz, H., and Wang, N.: Water activity measurements with single suspended droplets: The NaCl-H2O and KCl-H2O systems, Journal of colloid and interface science, 114, 409-415, 1986.

Tang, I. N.: Chemical and size effects of hygroscopic aerosols on light scattering coefficients, Journal of Geophysical Research: Atmospheres, 101, 19245-19250, 10.1029/96jd03003, 1996.

Thanh, N. T., Maclean, N., and Mahiddine, S.: Mechanisms of nucleation and growth of nanoparticles in solution, Chemical reviews, 114, 7610-7630, 2014.

Thompson, S., Gubbins, K., Walton, J., Chantry, R., and Rowlinson, J.: A molecular dynamics study of liquid drops, J. Chem. Phys., 81, 530-542, 1984.

Tolbert, S., and Alivisatos, A.: Size dependence of a first order solid-solid phase transition: the wurtzite to rock salt transformation in CdSe nanocrystals, Science, 265, 373-376, 1994.

Tolman, R. C.: Consideration of the Gibbs theory of surface tension, J. Chem. Phys., 16, 758-774, 1948.

Tolman, R. C.: The effect of droplet size on surface tension, J. Chem. Phys., 17, 333-337, 1949a.

Tolman, R. C.: The superficial density of matter at a liquid-vapor boundary, J. Chem. Phys., 17, 118-127, 1949b.

Trostl, J., Chuang, W. K., Gordon, H., Heinritzi, M., Yan, C., Molteni, U., Ahlm, L., Frege, C., Bianchi, F., Wagner, R., Simon, M., Lehtipalo, K., Williamson, C., Craven, J. S., Duplissy, J., Adamov, A., Almeida, J., Bernhammer, A. K., Breitenlechner, M., Brilke, S., Dias, A., Ehrhart, S., Flagan, R. C., Franchin, A., Fuchs, C., Guida, R., Gysel, M., Hansel, A., Hoyle, C. R., Jokinen, T., Junninen, H., Kangasluoma, J., Keskinen, H., Kim, J., Krapf, M., Kurten, A., Laaksonen, A., Lawler, M., Leiminger, M., Mathot, S., Mohler, O., Nieminen, T., Onnela, A., Petaja, T., Piel, F. M., Miettinen, P., Rissanen, M. P., Rondo, L., Sarnela, N., Schobesberger, S., Sengupta, K., Sipila, M., Smith, J. N., Steiner, G., Tome, A., Virtanen, A., Wagner, A. C., Weingartner, E., Wimmer, D., Winkler, P. M., Ye, P., Carslaw, K. S., Curtius, J., Dommen, J., Kirkby, J., Kulmala, M., Riipinen, I., Worsnop, D. R., Donahue, N. M., and Baltensperger, U.: The role of low-volatility organic compounds in initial particle growth in the atmosphere, Nature, 533, 527-531, 10.1038/nature18271, 2016.

Turnbull, D.: Formation of crystal nuclei in liquid metals, Journal of Applied Physics, 21, 1022-1028, 1950.

Van Der Spoel, D., Lindahl, E., Hess, B., Groenhof, G., Mark, A. E., and Berendsen, H. J.: GROMACS: fast, flexible, and free, Journal of computational chemistry, 26, 1701-1718, 2005.

Van Gunsteren, W. F., and Berendsen, H. J.: A leap-frog algorithm for stochastic dynamics, Molecular Simulation, 1, 173-185, 1988.

Vargaftik, N., Volkov, B., and Voljak, L.: International tables of the surface tension of water, J Phys Chem Ref Dat., 12, 817-820, 1983.

Vega, C., and de Miguel, E.: Surface tension of the most popular models of water by using the test-area simulation method, J Chem Phys, 126, 154707, 10.1063/1.2715577, 2007.

Veghte, D. P., Altaf, M. B., and Freedman, M. A.: Size dependence of the structure of organic aerosol, J. Am. Chem. Soc., 135, 16046-16049, 2013.

Veghte, D. P., Bittner, D. R., and Freedman, M. A.: Cryo-transmission electron microscopy imaging of the morphology of submicrometer aerosol containing organic acids and ammonium sulfate, Analytical chemistry, 86, 2436-2442, 2014.

Vicente, C., Yao, W., Maris, H., and Seidel, G.: Surface tension of liquid 4 He as measured using the vibration modes of a levitated drop, Phys. Rev. B, 66, 214504, 2002.

Virtanen, A., Joutsensaari, J., Koop, T., Kannosto, J., Yli-Pirilä, P., Leskinen, J., Mäkelä, J. M., Holopainen, J. K., Pöschl, U., and Kulmala, M.: An amorphous solid state of biogenic secondary organic aerosol particles, Nature, 467, 824-827, 2010.

von Helmholtz, R.: Untersuchungen über Dämpfe und Nebel, besonders über solche von Lösungen, Annalen der Physik, 263, 508-543, 1886.

Wagner, R., Höhler, K., Möhler, O., Saathoff, H., and Schnaiter, M.: Crystallization and immersion freezing ability of oxalic and succinic acid in multicomponent aqueous organic aerosol particles, Geophys Res Lett., 42, 2464-2472, 2015.

Wang, J., Wolf, R. M., Caldwell, J. W., Kollman, P. A., and Case, D. A.: Development and testing of a general amber force field, Journal of computational chemistry, 25, 1157-1174, 2004.

Wang, X., Chen, C., Binder, K., Kuhn, U., Pöschl, U., Su, H., and Cheng, Y.: Molecular dynamics simulation of the surface tension of aqueous sodium chloride: from dilute to highly supersaturated solutions and molten salt, Atmos. Chem. Phys., 18, 17077-17086, 10.5194/acp-18-17077-2018, 2018.

Wang, X., Binder, K., Chen, C., Koop, T., Pöschl, U., Su, H., and Cheng, Y.: Second inflection point of water surface tension in the deeply supercooled regime revealed by

entropy anomaly and surface structure using molecular dynamics simulations, Phys. Chem. Chem. Phys., 21, 3360-3369, 2019.

Wang, Z., Wu, Z., Yue, D., Shang, D., Guo, S., Sun, J., Ding, A., Wang, L., Jiang, J., and Guo, H.: New particle formation in China: Current knowledge and further directions, Science of the Total Environment, 577, 258-266, 2017.

Weissenborn, P. K., and Pugh, R. J.: Surface tension and bubble coalescence phenomena of aqueous solutions of electrolytes, Langmuir., 11, 1422-1426, 1995.

Weissenborn, P. K., and Pugh, R. J.: Surface tension of aqueous solutions of electrolytes: relationship with ion hydration, oxygen solubility, and bubble coalescence, J Colloid Interf Sci., 184, 550, 1996.

Werner, J., Julin, J., Dalirian, M., Prisle, N. L., Öhrwall, G., Persson, I., Björneholm, O., and Riipinen, I.: Succinic acid in aqueous solution: connecting microscopic surface composition and macroscopic surface tension, Phys. Chem. Chem. Phys., 16, 21486-21495, 2014.

Werner, J., Dalirian, M., Walz, M.-M., Ekholm, V., Wideqvist, U., Lowe, S. J., Öhrwall, G., Persson, I., Riipinen, I., and Björneholm, O.: Surface partitioning in organic–inorganic mixtures contributes to the size-dependence of the phase-state of atmospheric nanoparticles, Environ. Sci. Technol., 50, 7434-7442, 2016.

Wexler, A. S., Clegg, S. L.: Atmospheric aerosol models for systems including the ions H+, NH4+, Na+, SO42−, NO3−, Cl−, Br−, and H2O, J. Geophys. Res.: Atmos, 107(D14), 2002.

You, Y., Renbaum-Wolff, L., Carreras-Sospedra, M., Hanna, S. J., Hiranuma, N., Kamal, S., Smith, M. L., Zhang, X., Weber, R. J., and Shilling, J. E.: Images reveal that atmospheric particles can undergo liquid–liquid phase separations, P. Natl. Acad, Sci., 109, 13188-13193, 2012.

Yu, F., and Turco, R.: Case studies of particle formation events observed in boreal forests: implications for nucleation mechanisms, Atmos. Chem. Phys., 8, 6085-6102, 2008.

Yu, F., and Luo, G.: Simulation of particle size distribution with a global aerosol model: contribution of nucleation to aerosol and CCN number concentrations, Atmos. Chem. Phys., 9, 7691-7710, 2009.

Yue, D., Hu, M., Zhang, R., Wu, Z., Su, H., Wang, Z., Peng, J., He, L., Huang, X., and Gong, Y.: Potential contribution of new particle formation to cloud condensation nuclei in Beijing, Atmos. Environ., 45, 6070-6077, 2011.

Zhang, C., Guo, Y., and Priestley, R. D.: Glass transition temperature of polymer nanoparticles under soft and hard confinement, Macromolecules, 44, 4001-4006, 2011.

Zhang, H., Yin, C., Jiang, Y., and van der Spoel, D.: Force field benchmark of amino acids: I. hydration and diffusion in different water models, Journal of chemical information and modeling, 58, 1037-1052, 2018.

Zhang, J., Li, M., Feng, Z., Chen, J., and Li, C.: UV Raman spectroscopic study on TiO2. I. Phase transformation at the surface and in the bulk, J. Phys. Chem. B, 110, 927-935, 2006.

Zhang, R., Suh, I., Zhao, J., Zhang, D., Fortner, E. C., Tie, X., Molina, L. T., and Molina, M. J.: Atmospheric new particle formation enhanced by organic acids, Science, 304, 1487-1490, 2004.

Zhang, R.: Getting to the critical nucleus of aerosol formation, Science, 328, 1366-1367, 2010.

Zhang, R., Khalizov, A., Wang, L., Hu, M., and Xu, W.: Nucleation and growth of nanoparticles in the atmosphere, Chem Rev, 112, 1957-2011, 10.1021/cr2001756, 2012.

Zhang, Y., Wen, X.-Y., and Jang, C.: Simulating chemistry–aerosol–cloud–radiation–climate feedbacks over the continental US using the online-coupled Weather Research Forecasting Model with chemistry (WRF/Chem), Atmos. Environ., 44, 3568-3582, 2010.

Zheng, G., Su, H., Wang, S., Andreae, M. O., Pöschl, U., and Cheng, Y.: Multiphase buffer theory explains contrasts in atmospheric aerosol acidity, Science, 369, 1374-1377, 2020.

Zheng, G., Wang, Y., Wood, R., Jensen, M. P., Kuang, C., McCoy, I. L., Matthews, A., Mei, F., Tomlinson, J. M., and Shilling, J. E.: New particle formation in the remote marine boundary layer, Nature communications, 12, 1-10, 2021.

Zimmermann, N. E., Vorselaars, B., Quigley, D., and Peters, B.: Nucleation of NaCl from aqueous solution: Critical sizes, ion-attachment kinetics, and rates, J. Am. Chem. Soc., 137, 13352-13361, 2015.